Effects of Small-Displacement Faults on the Permeability Distribution of Poorly Consolidated Santa Fe Group Sands, Rio Grande Rift, New Mexico

by

John M. Sigda

Submitted in partial fulfillment
of the requirements for the degree of
Master of Science of Hydrology

New Mexico Institute of Mining and Technology
Department of Earth and Environmental Science
Socorro, New Mexico

October, 1997

ABSTRACT

The abundance of faulted sediments throughout many regions of continental crustal extension, such as the western United States, stands in strong contrast to our relatively poor understanding of their hydrologic importance. Faults in poorly consolidated sediments, like those in well indurated rocks, range from tens of kilometers to mere meters in length and from kilometers to millimeters in displacement. Yet important differences with faults in well indurated rocks have been noted: faults in poorly consolidated sediments display unique structural features and can cross-cut the thick vadose zones and underlying aquifers found in sediment-filled basins such as those supplying water to the western United States' rapidly growing population. Little is known about the hydrologic properties of such faults. In contrast, hydrologists and petroleum geologists have long known faulting can exert potent controls on flow of hydrocarbons and groundwater in well indurated rocks, often dramatically changing their saturated hydraulic properties. Recent studies have documented faulting-induced changes in permeability ranging between three and eight orders of magnitude in crystalline and well indurated porous sedimentary rocks. Does faulting alter the single fluid-phase permeability of poorly consolidated sediments just as significantly?

The following hypotheses were tested as the first step to answering this question:

Small-displacement faulting can create significant changes to the single fluid-phase permeability of poorly consolidated sands within the Rio Grande Rift;

and

Single fluid-phase permeability changes within poorly consolidated sand fault zones are caused by deformational and diagenetic processes such as comminution and alteration of grains.

The hypothesis tests focus on uncemented, small (< 1 m) and moderate (≥ 2.5 m) displacement to fault zones in sands to eliminate confounding effects from juxtaposition of differing lithologies.

More than 1000 *in situ* measurements were collected with air and gas mini-permeameters at two faulted Santa Fe Group outcrops within the Rio Grande rift. The spatial variability of permeability within the undeformed and fault zone sands was quantified using variography. Point count analysis of epoxy-impregnated thin sections provided estimates of porosity, grain size, and mineral composition. X-ray diffractometry determined clay-size fraction mineral composition. Scanning electron microscopy afforded visual comparison of deformed and undeformed sands.

Deformed sand intrinsic permeability decreases as much as two to three orders of magnitude relative to undeformed sands. Exhibiting values on the order of 10 darcies, average undeformed sand permeability is less variable than average permeability within fault zones. Low fault zone permeability reduction is positively correlated with low macroporosity and average pore and grain sizes, reorientation of elongate grains, large clay-size fraction and clay mineral abundance, diagenetic alteration of feldspars, and redistribution of clays to form grain coatings and other pore-occluding microstructures. Calcite cement abundance was negligible in both deformed and undeformed samples.

Results support the hypothesis that deformational and diagenetic processes associated with small-displacement faults can significantly alter the original single fluid-phase permeability of poorly consolidated sands.

TABLE OF CONTENTS

LIST OF TABLES

LIST OF FIGURES

ACKNOWLEDGMENTS

This research was funded in part by the U.S. Department of Energy and Sandia National Laboratories (SNL) under the guidance of Dr. James T. McCord. Additional funding was contributed by the Roswell Geological Society and the Antonius Budding Award from New Mexico Tech's Department of Earth and Environmental Science (E&ES).

Dr. Dave Love and Dr. John Hawley of the New Mexico Bureau of Mines and Mineral Resources (NMBMMR) gladly gave of their time and enthusiasm in identifying study sites. Phil Norton and John Taylor of the Bosque del Apache National Wildlife Refuge kindly provided site access, support, and patience.

Dr. Peter Mozley and Dr. Laurel Goodwin (E&ES) and Dr. William Haneberg of the NMBMMR enthusiastically taught me the rudiments of collaboration and of the many geological techniques employed in this research.

Vince Tidwell (SNL) provided his prototype field mini-permeameter as well as unfailing support.

Dr. Allan Gutjahr (Department of Mathematics), Dr. John Wilson, and Dr. Fred Phillips, (E&ES), proved to be marvelously supportive, patient, and then patient again as my advisors and committee members.

I thank you and all the many other faculty and staff at New Mexico Tech and NMBMMR who assisted me. Thank you for your creative input, financial wherewithal, and enthusiastic support.

To my wife, Rebecca, and my children, thank you for your years of sacrifice and love:

Ninawapenda ninyi kila mmoja daima, na ninamwomba Mwenyezi Mungu awabariki kila siku.

This thesis is accepted on behalf of the faculty
of the Institute by the following committee:

Advisor

Date

I release this document to the New Mexico Institute of Mining and Technology.

Student's Signature

10-24-97
Date

INTRODUCTION

From the Sierra Nevada's eastern edge to central New Mexico, sediments and faults are distinctive and potentially important features of many basin-fill aquifer units. Active extension of the continental crust in this region, most of which lies within the Basin and Range Province, has uplifted long, parallel mountain ranges and down-dropped basin blocks along faults. The poorly consolidated basin-fill sediments, eroded from adjacent mountains, were repeatedly faulted as the basins subsided relative to the up-thrown blocks. Ranging from tens of kilometers to mere meters in length, these faults have accommodated vertical displacements from kilometers to millimeters. The number of faults distributed across an area of crustal extension can be quite large: recent data from New Mexico's Española Basin suggest small displacement faults (0.01 - 1.0 m) may number more than 3000 within a roughly 400 km^2 (150 mi^2) area (Carter and Winter, 1995). Many such faults cross-cut the basin aquifers on which most of the region's rapidly growing population depends. Yet little is known of the fault-related changes to basin-fill sediments, whether from a structural, a sedimentological, or a hydrologic perspective.

In sharp contrast to faults within poorly consolidated sediments, there is a profusion of information about the structural and hydrologic characteristics of faults in well indurated rocks. Geologists have characterized single fluid-phase permeability of gouges recovered from faulted crystalline rocks to better understand the interrelationship between fault slip and pore-water movement (Morrow et al., 1981 and 1984). Petroleum geologists have long known fault zones in well consolidated reservoir rocks can control oil and gas recovery (Smith, 1966 and 1980; Berg and Avery, 1995). Recently published intrinsic permeability measurements of faulted, well indurated, porous, sedimentary, reservoir rocks, or their outcrop analogs, indicate these fault zones are 10^3 to 10^7 less permeable than the parent material (Antonellini and Aydin, 1994; Fowles and Burley, 1994).

Current conceptual hydrogeological models of fault zones in crystalline rock describe fault segments as cores of low permeability fault gouge surrounded by heavily fractured zones within which permeability is typically enhanced (Smith et al., 1989; Scholz and Anders, 1994). Well indurated, porous, sedimentary rocks appear to accommodate fault stresses differently by forming one or more of a hierarchical series of structures: deformation bands, zones of deformation bands, and slip surfaces, each of which possesses a much lower permeability than undeformed rock (Aydin, 1978; Aydin and Johnson, 1978; Antonellini and Aydin, 1994; Antonellini et al., 1994). Caine et al. (1996) have suggested the hydrologic behavior of a single fault is governed by the proportions of total fault width occupied by the low permeability cataclasite core and by the enhanced permeability damage zone.

It is unclear whether these conceptual hydrogeologic models properly pertain to faults in poorly consolidated sediments given the present lack of information about their hydraulic properties. Features similar to the slip surfaces and deformation bands of Aydin and others have been reported for one such fault (Mozley and Goodwin, 1995; Heynecamp et al., 1995). The paucity of data about the porosity and permeability of faults in poorly consolidated sediments effectively precludes adequate understanding of the influence from such faults on flow and transport through poorly consolidated sediments.

Poorly consolidated basin-fill sediments form important reservoirs for both hydrocarbons and drinking water, intimating that faults within these reservoirs may possibly have economic or public policy impacts. Many of the cities in the American Southwest and West which depend on basin-fill aquifers (e.g., Phoenix and Tucson, AZ; Albuquerque, NM; Las Vegas, NV; Salt Lake City, UT) face critical water resource management problems brought on by their burgeoning populations. Fault compartmentalization of hydrocarbon reservoirs, which strongly affects recovery efficiency and cost, has been well established for well indurated rocks (Smith, 1966 and 1980; Weber, 1978) but has yet to be determined for poorly consolidated reservoirs. Proper assessment of the influence exerted by

faults in poorly consolidated sediments on fluid flow through basin-fill reservoirs requires a better understanding of their horizontal and vertical extensiveness, their areal density, and their hydraulic properties relative to the parent sediments.

The initial objective of this research was to determine what, if any, effect faulting has on the permeability distribution of poorly consolidated sediments, particularly those common in the southwestern United States. The primary hypothesis tested is

> Faulting can create significant changes to the single fluid-phase permeability of poorly consolidated sands within the Rio Grande Rift.

The hypothesis test is restricted to small (< 1 m) and moderate (≥ 3 m) displacement faults, because they constitute the limiting case (if smaller displacement faults change parent permeability, then so will larger displacement faults) and because smaller displacement faults tend to reduce or eliminate complications from juxtaposition of different lithofacies. The smaller the displacement, the greater the likelihood that a particular lithologic unit will maintain contact with itself across both fault blocks.

Also tested is the hypothesis, ancillary to the first, that

> The single fluid-phase permeability change within poorly consolidated sand fault zones is caused by deformational and diagenetic processes.

The second hypothesis test is simplified by focusing on uncemented fault zones. Although cemented fault zones within otherwise poorly consolidated sediments (Mozley and Goodwin, 1996) and syn-slip cementation of faults (e.g., Knipe, 1992; Edwards et al., 1993) have been observed, exclusion of cemented faults should provide a better understanding of incipient fault zone permeability

and the relevant deformational and (non-cementation) diagenetic processes by avoiding the confounding effects from post-slip cementation.

Representing a first step in understanding the hydrologic significance of faults in poorly consolidated sediments, this study describes initial tests of the two hypotheses. Single fluid-phase permeability (hereafter denoted as permeability) of deformed and undeformed Upper Santa Fe Group (NM) sands are estimated through *in situ* permeametry to determine whether there are differences in the permeability distribution associated with faulting. Grain and pore size distributions, porosity, and mineral abundance for faulted and undeformed poorly consolidated sands are compared through petrographic analyses to identify which, if any, deformational and diagenetic processes were associated with observed differences in permeability.

CONCEPTUAL MODELS OF FAULTS AND PERMEABILITY

Elucidating the hydrologic roles of faults in poorly consolidated sediments necessitates understanding a multitude of physical and chemical processes, which are typically the domain of structural geology, sedimentology, and hydrology, as perceived from the pore-scale to the basin-scale. By drawing upon these disciplines, this chapter introduces the ways in which faults are physically expressed in the earth's subsurface and reviews our present-day understanding of how faults are distributed across the crust, how faulting alters the petrophysical properties of rocks, and the ways in which faults affect fluid flow through aquifers and petroleum reservoirs. Although the bulk of current and past literature has dealt with faults in well indurated rocks, the primary focus remains on faults in poorly consolidated sediments.

Questioning the impact of faults in poorly consolidated sediments on fluid flow is at least partly motivated by economic concerns. Faulting within areally extensive hydrocarbon reservoir formation often creates juxtaposition or deformation-diagenesis seals, which subdivide the reservoir into compartments because fluids, especially non-wetting phases, cannot easily pass through the seals (Knipe, 1992, 1993). Designing wells for optimal hydrocarbon extraction requires estimates of the number, size, and location of reservoir compartments; however, many of the faults responsible for subdividing the reservoir cannot be detected by most surface and subsurface characterization methods (Gauthier and Lake, 1993). Three-dimensional seismic studies of petroleum reservoirs cannot resolve faults with throws (the purely vertical component of dip-slip displacement) less than 12 m, but seals are often created by faults with much smaller throws (Gauthier and Lake, 1993).

Fault compartmentalization of aquifers is not ordinarily considered a serious problem in managing most groundwater basins, yet it may also portend significant economic and policy concerns. The role of faults in controlling aquifer-river interactions, in distributing mountain-front recharge, and

in history-matching are important issues facing the USGS as it develops a groundwater model for managing the Albuquerque Basin's (New Mexico) groundwater resources (Thorn et al., 1993). Faults may also exert strong local controls on the efficacy of a contamination site's groundwater remediation scheme. For example, low-permeability faults could impede recovery of contaminants in pump and treat systems, especially in densely faulted basin-fill aquifers.

Expressing Stress: Fault Types and Formation

A fault is a mark of the rise and fall of stresses in the earth's crust. Opposed by cohesive and frictional forces and often abetted by pore fluid pressure, stress eventually surmounts enough resistance to allow blocks of crust to move, creating a zone of rock failure or accommodation - the fault. This movement, known as displacement or slip, varies from millimeters to kilometers; fault zone widths show similar ranges of magnitude. Lateral expression (strike) may reach hundreds of kilometers though the fault seldom extends more than 10 - 20 km vertically. Direction of fault block movement (shear) may be primarily vertical (dip-slip), horizontal (strike-slip), or a combination of the two (oblique-slip). Orientation of the three-dimensional principal stresses determines each of the ideal fault types according to Andersonian faulting theory: a vertically oriented minimum compressive principal stress tends to shorten the crust, producing thrust and reverse faults; vertical orientation of the maximum compressive principal stress yields normal faults, which lengthen the crust; and strike-slip faults form when the intermediate principal compressive stress is vertically oriented (see Twiss and Moores, 1992, pages 202-203).

The perimeter encompassing the extent of observable deformation is denoted the fault tip line. The extent of observable deformation for a single fault buried at depth forms an envelope which, when simplified to two dimensions (i.e., the slip plane) is thought to have an elliptical shape (Barnett et al., 1987; Walsh and Watterson, 1988; Cowie and Scholz, 1992a). According to this model, displacement decreases from its maximum at the center outwards to the perimeter of the ellipse (Walsh and

Watterson, 1988). Fault length is the horizontal distance between the ellipse's apices. The line formed by the intersection of the ellipse and the earth's surface is the fault trace A fault which has no trace, i.e., does not intersect the earth's surface, is denoted blind.

Real world faults typically demonstrate a far richer three-dimensional complexity than is accommodated by this simple elliptical model. Splays are subsidiary faults which branch off from (and may later rejoin) the main fault. Nearby faults or faults and splays which share a roughly contemporaneous origin constitute a fault zone. Pods of protolith (parent rock) showing little or no deformation bounded by adjacent faults or splays are called horses. Maximum displacement is often observed far from a fault's presumed midpoint (Carter and Winter, 1995). Strike or dip may change many times along a fault's length, but dip-slip faults are typically more variable along strike than dip whereas strike-slip faults show greater variability along dip than strike.

Adding another layer of complexity, faults can reactivate or slip more than once under the same or differing tectonic environments. Total displacement on a single fault may comprise one, several, or tens of slip events. Reactivation can increase fault length through propagation of fault tips (Cowie and Scholz, 1992a) or through linkage of previously existing faults (Segall and Pollard, 1983). Reactivation of one fault may prevent growth of another fault by blocking advance of its tip line (Cowie and Scholz, 1992a).

The areal density of faults varies widely and is influenced by lithology, tectonic history (including type of tectonic regime, stress field orientation, and time rate of change), and amount of subsequent reactivation. Fault numbers can be especially high within areas which have been subjected to extensional stress regimes, such as rift valleys (Carter and Winter, 1994; Schlische et al., 1996) or collapse of salt domes (Aydin, 1977; Aydin and Johnson, 1977

Lost in Space: Models of Fault Spatial Distributions

The spatial distribution of faults represents yet another level of complexity, one that is much less well understood than the others but often has important economic consequences. Assessing the engineering impact of faults on hydrologic or hydrocarbon reservoir systems requires knowledge of the number and spatial distribution of faults which act as barriers to single or multi-phase fluid flow, but the techniques available for locating faults within the subsurface cannot detect all sealing faults, particularly those with displacements smaller than 12m (Gauthier and Lake, 1993). This section reviews research on the spatial distribution of fault populations and the conceptual models which can be used to predict or simulate the location of undetected sealing faults.

To be practicable, each conceptual model must describe the locations, areal density (numbers per unit area or volume), orientation, and physical dimensions (length, width, depth) of faults. Major modes of orientation can be inferred from observations of the distributions of structures, such as fault maps (Gauthier and Lake, 1993). The simple, two-dimensional models of faults as elliptical planes (Barnett et al., 1987; Cowie and Scholz, 1992a) can provide limited constraint on maximum displacement relative to fault length and can be readily simulated using Boolean algorithms (e.g., the GSLIB subroutine *ellipsim* by Deutsch and Journel, 1992). However, these simple models lack any means for constraining or predicting fault locations or fault areal density as a function of either maximum displacement, length, or both.

Several decades of field studies have demonstrated proportional relationships between fault length and maximum displacement and between number of faults and either length or displacement (Elliott, 1976; Marrett and Allmendinger, 1991; Cowie and Scholz, 1992b; Carter and Winter, 1995; Nicol et al., 1996; Schlische et al., 1996). With the advent of fractal mathematics (Mandelbrot, 1967 and 1983), numerous researchers posited that the observed proportional relationships were actually fractal

relationships, i.e., the dimensionality of each relation lies between integer values (Turcotte, 1986; Marrett and Allmendinger, 1991; Cowie and Scholz, 1992b; Carter and Winter, 1995).

The fractal relationship between maximum displacement, d, along the fault's length and fault length, L, is given by

Equation 1: Fault Displacement - Length Power Law

$$d = \gamma L^{C}$$

where γ is a constant thought to be a function of the lithology (Cowie and Scholz, 1992a) and the constant C is typically estimated as close to 1 (Cowie and Scholz, 1992b; Carter and Winter, 1995; Schlische et al., 1996). Variables d and L have units of length, often kilometers or meters.

The second key fractal function defines the number of faults N within a given area as a function of the maximum displacement d along their lengths such that the cumulative number of faults with displacement d greater than or equal to some minimum value d_{min} is a power law function of d_{min}:

Equation 2: Number of Faults vs. Displacement Power Law

$$N(d \geq d_{min}) = \alpha\, d_{min}^{-D}$$

Variables d and d_{min} have units of length, typically kilometers. Constant α, which gives the number of faults with maximum displacement ≥ one length unit, is estimated to range from 10^{-2} to 10^{4} when length is given in kilometers. D, which defines the fractal dimension, has estimates ranging from 0.6 to 2.3 for kilometer length units (Gauthier and Lake, 1993; Carter and Winter, 1995). Given values for each parameter, the number of faults with maximum displacement between 0.001 and 0.010 kilometers is determined by subtracting N(d > 0.010 km) from N(d > 0.001 km).

Adopting a conceptual model which treats fault spatial distributions as fractal relationships between length, displacement, and number offers several advantages for estimating impacts from fault compartmentalization. An entire population of faults is fully characterized by only four parameters: C, γ, α, and D, allowing estimation of fault areal density as a function of either displacement or length. Data from field techniques which measure maximum displacement can be combined with those from techniques which yield length measurements. Perhaps the model's greatest utility lies in its capacity to estimate the number of faults which fall within a maximum displacement range that cannot be detected from a wholly different, but measurable, displacement range. Thus, one can estimate the number of potentially sealing faults with displacements less than the 12 m minimum detectable by 3D seismic methods (Gauthier and Lake, 1993). Furthermore, the number of typically unmapped small-displacement faults ($\leq$ 3 m) that also suffer from an undersampling bias, can be estimated from easily mapped faults to obtain more accurate estimates of strain within an extensional tectonic regime (Carter and Winter, 1995). For example, using data collected for the Espanola Basin of the New Mexico Rio Grande rift, the number of faults with displacement $\leq$ 1 m within a 400 km^2 area of consolidated and poorly consolidated sediments may reach 3000 (Carter and Winter, 1995).

Despite its predominance within the literature, the fractal conceptual model displays several important weaknesses, both as a hypothesis and as a working solution to the fault compartmentalization problem. There are numerous disagreements about the parameter values estimated for the fractal relations and about the methods used to calculate the estimates, such as avoiding sampling biases, handling fault splays; and choosing proper regression techniques (Cowie and Scholz, 1992a and b; Clark and Cox, 1996; Nicol et al., 1996; Schlische et al., 1996). Many data plots of fault number versus maximum displacement appear to indicate the presence of one or more fractal dimension values (D in Equation 2), especially for smaller displacement faults, which may be the result of undersampling smaller displacement faults or else suggests the fractal hypothesis

is not valid (Marrett and Allmendinger, 1991; Carter and Winter, 1995; Nicol et al., 1996). Another drawback is the model's inability to predict or simulate the location of each of the expected faults (Gauthier and Lake, 1993).

Dividing the Waters: Fault Controls on Hydraulic Properties

Narrowing the perspective from a regional to a single fault view allows a closer examination of the relationship between the petrophysical characteristics of faults and local changes in hydraulic properties, particularly permeability. Faulting can induce large-scale permeability changes through juxtaposition of lithologic units with different permeabilities, significantly influencing fluid flow through the faulted reservoir (Tolman, 1937; Dutcher and Garrett, 1963; Davis and DeWeist, 1966; Bernard et al., 1989; Haneberg, 1995; Matthai and Roberts, 1996). However, in keeping with the proposed test of the first hypothesis (restricted to small- and moderate-displacement faults), this section focuses on the creation and evolution of permeability within the fault zone itself.

Post-slip fault zone permeability, which here refers to permeability evolution beginning with a slip event, is governed by two broad classes of petrophysical processes. Physical changes to the original rock driven by movement along the fault's slip plane (deformation) and a host of alterations, subsequent to slip, driven by physico-chemical processes not directly related to fault movement (diagenesis) create permeability differences between the parent material and fault rock. This section reviews the various deformational and diagenetic processes which can alter fault-zone permeability and then examines the petrophysical and permeability changes observed in well indurated rocks and poorly consolidated sediments.

Deformational and Diagenetic Processes

Movement along a fault's slip surface can deform the parent rock or sediment through a number of processes, including fracturing, cataclasis, bed drag, and compaction, each of which operates at

different scales. These deformational processes create the first changes to the parent rock permeability, which may in turn be further modified by additional slip or by the wide array of physical and chemical alterations known as diagenetic processes.

Fractures opened by faulting (e.g., parallel and conjugate shear fractures) of competent rock can increase permeability, especially in rock immediately adjacent to the fault zone (Smith et al., 1989; Twiss and Moores, 1992; Caine et al., 1996). Post-slip mineralization of the fractures by allogenic or remobilized authigenic minerals, conveyed through preferential fluid flow, corroborates the higher permeability of this fracture or damage zone (Smith et al., 1989; Edwards et al., 1993).

Cataclasis, defined as distributed microcracking of the parent material with grain boundary sliding and rotation of fragments, operates at smaller scales than fracturing and typically reduces permeability. Continued cataclasis grinds rock fragments into powder or flour-sized particles and can eventually form fault gouge, which is typically many orders of magnitude lower in permeability than even the crystalline parent rock (Engelder, 1974; Morrow et al., 1981 and 1984; Smith et al., 1989). Cataclasis reduces grain and pore sizes in sandstones and similar clastic rocks: within a deformation band or adjacent to a slip surface, grains may be comminuted to clay-sized fragments, leading to a poorly sorted grain-size distribution, and often almost entirely eliminating porosity (Aydin, 1978; Pittman, 1981; D'Onfro et al., 1984; Edwards et al., 1993). Porosity can also be eliminated or reduced through compaction, without any of the microcracking or grain boundary sliding which define cataclasis (Antonellini et al., 1994).

Sediment beds, particularly beds of finer-grained sediments, dragged into a fault zone can also significantly reduce the local permeability relative to the parent rock. Clay and shales may be smeared along or mixed with fault zone materials during slip. Depending on the amount and location of clay or shale beds, smearing can create zones with relatively homogeneous pore size distributions which retard

fluid flow and often support build-up of non-wetting phases such as hydrocarbons (Gibson, 1994; Berg and Avery, 1995). Elongate grains and phyllosilicate sheet structures are often realigned from a parallel-to-bedding to a parallel-to-dip orientation which tends to increase permeability anisotropy within a fault zone (Davis and DeWeist, 1966; Knipe, 1992, 1993; Mozley and Goodwin, 1995).

Largely controlled by the quantity and chemical composition of migrating pore fluids, fault zone diagenetic processes operate on both rock matrix and void space. Permeability differences between faulted and undeformed materials created by deformational (and previous diagenetic) processes typically give faults different diagenetic histories than those observed in the surrounding undeformed materials. Changes in pore and grain-size distributions, fluid saturation, increases in rock matrix surface area, and a possible post-slip rise in pH through abrasion pH may also affect both type and rate of diagenetic alterations. Preferential cementation and dissolution are commonly observed in fault-zone rocks (Flournoy and Ferrell, 1980; Knipe, 1993, 1992; Edwards et al., 1993; Fowles and Burley, 1994; Mozley and Goodwin, 1995). Large increases in matrix surface area suggest mineral replacement and alteration, such as alteration of comminuted feldspars to clays, also occur preferentially within fault zones. Fault zone pore structures, altered by slip-induced porosity collapse, may be further altered by repacking of clay minerals (Knipe, 1993), or by mobilization and re-precipitation (elluviation and illuviation) of clay-sized materials, or by the addition of mechanically infiltrated clays (see discussions by Matlack et al., 1989 and Moraes and de Ros, 1990).

By changing the porosity, pore sizes, and pore interconnectivity in porous media, the deformational and diagenetic processes described above often alter the permeability or the parent material. These same processes may also alter other hydraulic and transport properties, such as unsaturated hydraulic conductivity or hydrodynamic dispersion, because these properties are likely affected by the skewing of the pore size distributions towards small pores and increase in clay-sized materials and/or clay minerals. For example, the larger proportion of small (though still

interconnected) pores within a deformed zone should raise the faulted sediment's unsaturated hydraulic conductivity relative to that for the parent sediments at the high capillary pressures commonly observed in arid areas.

Faults in Well indurated Rocks

Smith et al. (1989) and Scholz and Anders (1994) have described models of fault zones in crystalline rock within which fault segments comprise low-permeability fault gouge cores surrounded by heavily fractured, relatively high-permeability damage zones. Permeability of the parent crystalline rock is primarily confined to fractures. Anastomosing fault segments branch and rejoin, enveloping pods of essentially undeformed protolith. Permeability of such fault zones tends to be strongly anisotropic (Smith et al., 1989; Forster and Evans, 1991).

Fault zone architecture of porous, well indurated sandstones differs significantly from crystalline rock models in size, geometry, and distribution of areas affected by deformation (Aydin, 1978; Aydin and Johnson, 1978; Pittman, 1981; Edwards et al., 1993; Antonellini and Aydin, 1994; Antonellini et al., 1994; Fowles and Burley, 1994). These authors describe a hierarchical model of deformation structures: slip surfaces, deformation bands, and zones of deformation bands (using the nomenclature of Aydin, 1978). Slip surfaces, the main fault surfaces, accommodate the greatest amount of displacement and have dimensions on the order of a meter wide and hundreds to thousands of meters long. Zones of deformation bands, which are defined as a host of adjacent, sometimes anastomosing, 1-2 mm wide bands of cataclasis and/or volume change, can occur singly or together with slip surfaces, accommodate up to a few decimeters of slip, and typically extend for tens of meters. Individual deformation bands are usually more densely distributed near to slip surfaces and zones of deformation bands (tens to hundreds per linear meter) but can be found tens to hundreds of meters from fault zones in reduced densities (one or more per linear meter). Deformation bands typically exhibit lengths on the order of meters to tens of meters and their maximum displacements of < 2 mm

are often sufficient to reduce porosity to nearly zero (Aydin and Johnson, 1978; Pittman, 1981; Edwards et al., 1993; Antonellini and Aydin, 1994; Fowles and Burley, 1994). Saturated permeability of cataclastic deformation bands has been estimated to be 10^{-3} to 10^{-4} of the parent sandstone permeability while slip surface permeability is 10^{-7} that of the parent (Antonellini and Aydin, 1994; Fowles and Burley, 1994). Despite continued research over the last several decades, there is yet no consensus about the importance of deformation bands and zones of deformation bands in compartmentalizing hydrocarbon sandstone reservoirs (Pittman, 1981; Antonellini and Aydin, 1994; Fowles and Burley, 1994; Berg and Avery, 1995).

After mapping a wide variety of faults, Caine et al. (1996) generalized the hydrogeologic conceptual model of Smith et al. (1989) by suggesting fault zone permeability is a function of the proportions of gouge core and damage zone thickness to total fault zone thickness. The greater percentage of gouge core, the more the fault will tend to act as a local barrier to fault-normal fluid flow; conversely, the greater the percentage of damage zone, the more the fault will act as a conduit to flow albeit parallel to fault dip or strike, unless the absence of a gouge zone allows cross-fault flow. The conceptual model predicts faults with extensive gouge cores and damage zones should act as both conduits and barriers to flow (Caine et al., 1996).

Faults in Poorly Consolidated Sediments

Though they have been the focus of studies to determine the recurrence interval of major earthquakes (Machette, 1978, 1982, and 1986; Machette et al., 1991), faults in poorly consolidated sediments have only recently received attention. Mozley and Goodwin (1995) reported observations of slip surfaces, deformation bands, and zones of deformation bands, similar to those described by Aydin and coworkers, in a major fault within the poorly consolidated sediments of the Albuquerque Basin of New Mexico. Extending for nearly 50 km, the Sand Hill fault accommodated ~600 m of displacement and serves as the western boundary for the Albuquerque Basin (Hawley and Haase, 1992). Mozley

and Goodwin (1995) observed deformation bands with widths up to 1 cm, fracturing and/or elongate grain reorientation within several centimeters of a given deformation band boundary, and the presence of tectonically mixed zones of bedding up to 3 m wide within the fault zone. Pods of material showing little to no deformation were also preserved within the fault zone. Heynecamp et al. (1995) noted a positive correlation between the Sand Hill fault zone width and average grain size of the surrounding undeformed materials: fault zone width decreased from several meters to a few centimeters when the surrounding sediments changed from coarse sands and gravels to fine sands and silts. Cementation was extensive in the sands and gravels, but minor or absent when the fault passed through fine-grained sediments (Mozley and Goodwin, 1995; Heynecamp et al., 1995).

Assessing the hydrologic importance of each of the structures reported for faults in poorly consolidated sediments, e.g., slip surfaces, deformation bands, horses, and mixing zones, awaits determination of their individual hydraulic properties relative to undeformed parent sediments.

Hindrance or Help: Faults and Fluid Flow

Evaluation of fault zone impacts on fluid flow and transport through single fluid-phase saturated media has usually focused on determining whether the fault in question acts as a conduit or barrier to fluid flow. Approaches include inferring the fault zone's behavior from observed hydraulic head or fluid pressure distributions or from estimated fault zone hydraulic properties or using models to investigate the limits of faulted flow systems.

Petroleum Reservoirs

Reservoir pressure data and gas-oil-water interface locations in hydrocarbon reservoirs have long been used to infer whether faults impede or facilitate hydrocarbon flow (e.g., Smith, 1966 and 1980; Weber, 1978; Harding and Tuminas, 1988; Gibson, 1994). Berg and Avery (1995) note that growth faults in interbedded sandstones and shales of the Texas Gulf Coast can act as seals where shales are

dragged along dip but may leak where sandstone is cleanly juxtaposed against sandstone. Bredehoeft et al. (1992) applied numerical modeling to contrast the case that faults in Wyoming's Big Horn Basin are potential conduits for vertical flow with the cases that either the faults have no influence on horizontal flow or are barriers to horizontal flow. Treating faults as fractal quantities, Gauthier and Lake (1993) augmented 3D seismic maps of faults at the Pelican Field (North Sea, UK) with fractally-generated equiprobable realizations of seismically unresolved faults and used a reservoir production simulator to examine how well the augmented fields matched the production history. Testing the importance of fault-zone permeability on hydrocarbon movement through sand-shale reservoir units with a multi-grid finite-element numerical model, Matthai and Roberts (1996) demonstrated cross-fault flow from footwall to hanging wall decreases quickly as fault permeability becomes less than that of the least permeable aquifer unit.

Aquifers

By mapping hydraulic heads across faults in present-day aquifer systems, Titus (1963) and Maclay and Small (1983) demonstrated that faults can sufficiently impede groundwater flow to create head differences of tens of meters or more. Huntoon and Lundy (1979) described preferential flow parallel to, but outside, fault zones located in the interbedded sandstones and limestones of the Casper aquifer near Laramie, Wyoming. Observations of hydraulic head jumps and water quality changes across large-displacement thrust faults in the same region showed these faults create independent groundwater circulation systems by severing flow between the foot wall and hanging wall aquifers (Huntoon, 1985). Huntoon (1981) suggested parallel-to-strike flow along and through high-angle normal fault zones enabled groundwater from the upgradient east side of the Colorado River to discharge via springs into the river from the west side. Similarly, Kolm and Downey (1994) concluded that fault-normal flow was reduced and fault-parallel flow was enhanced in faulted aquifers beneath the Amargosa Desert of southern Nevada and California. Based on borehole packer tests to

measure the permeability of the Ramapo Fault in northern New Jersey (United States), Ganser (1987) determined little or no recharge to the adjacent water supply aquifer flowed through the fault zone.

Recent, simple models have direct bearing on saturated flow through fault zones. Bernard et al. (1989) used numerical modeling to explore the sensitivity of saturated flow to fault "throw" or offset within a simple faulted aquitard-aquifer-aquitard system without any permeability difference between the fault and parent material. Shan et al. (1995) developed analytic saturated flow solutions for determining the transmissivity of steeply dipping fault zones cutting homogeneous aquifer-aquitard-aquifer systems from pumping test data. Haneberg (1995) modeled faults using a one-dimensional analytical solution to the groundwater flow equation. Differing combinations of transmissivity ratios and recharge/discharge produce distinct head profiles which can be qualitatively used to infer the nature of hydrogeologic systems. Haneberg (1995) applied the modeling approach to help interpret a real flow system within the Albuquerque Basin. Pine (1995) employed a numerical model to investigate three-dimensional flow around faults. Among his findings are: (1) faults have locally significant impacts on vertical and horizontal head gradients; (2) information on fault displacement, reverse-drag profile, fault-dip, and fault zone permeability distribution are needed to accurately model impacts on groundwater flow; and (3) vertical head gradients are more sensitive to fault dip than horizontal gradients.

Other modeling studies of fault impacts on fluid flow have focused on coupled fluid flow and heat transport (Forster and Smith, 1988; Smith et al., 1989; Forster and Evans, 1991). Ge and Garven (1994) coupled deformation and groundwater flow to model the high pore fluid pressures along low permeability faults within a thrust sheet of the Canadian Rockies.

Faults and Effective Hydraulic Properties

Hydrogeologic conceptual models of faults introduced during the last several years focus on a single fault or fault zone and its single-phase permeability. Yet thicknesses of individual fault zones are typically many orders of magnitude smaller than a modeller's discretized domain unit length, requiring calculation of upscaled or effective permeabilities for each faulted grid block. Essentially an averaging process, permeability upscaling utilizes information about fault areal density, spatial distribution, thickness, and fault zone permeability distribution, most of which presently remains little more than speculation. Effective permeability also depends on the assumed dimensionality and orientation of the flow field and location and type of boundary conditions (Bear, 1972).

Assuming faults are oriented sub-parallel to one another, e.g., in rift basins such as the Rio Grande rift, permits application of a number of approaches originally devised by petroleum engineers to estimate effective permeability of the interbedded shale and sandstone sequences often encountered in hydrocarbon reservoirs (e.g., Deutsch, 1989; Durlofsky, 1991 and 1992). Sub-parallel faults substitute for shales as low permeability baffles within a more or less uniform sand aquifer. Unfortunately, shale thickness and spatial distribution data are readily available whereas equivalent data for fault zones are not, suggesting simulation approaches are best suited to constrain estimation of effective fault zone single-phase permeability. Still far less is known about fault influence on other effective hydraulic properties such as unsaturated permeability or macrodispersivity.

Summary

Faults in poorly consolidated sediments are commonplace in extensional tectonic regimes such as the United States' Basin and Range Province. Despite their areal extensiveness, little is known of their influence on fluid flow through aquifers or petroleum reservoirs. Numbers of small-displacement faults, which are typically not mapped but may affect fluid flow, can be estimated from observations of larger faults using a fractal-based conceptual model of fault spatial distribution.

Deformation and diagenesis tend to reduce single-phase permeability in clastic rocks but can both reduce and increase the permeability of crystalline rock fault zones. Skewing the pore-size distribution to smaller sizes is the primary cause of decreased permeability in clastic fault zones. The increased proportion of smaller pores in fault zone rocks suggests faults may potentially demonstrate unsaturated permeabilities larger than those for the undeformed sediments given the high capillary pressures common in arid southwest vadose zones.

Saturated fluid flow can be impeded, aided, or both by faults depending on the extent of deformational and diagenetic alterations. Low permeability faults, relative to the surrounding materials, can create strong local gradients as well as trap non-wetting fluids such as oil or gas by acting as capillary barriers.

It is not presently possible to determine whether the conceptual hydrogeologic models of Smith et al. (1989), Scholz and Anders (1994), Antonellini and Aydin (1994), or Caine et al. (1996) pertain to faulted basin-fill sediments without data on the single fluid phase permeability and porosity of the deformational structures. The research described in the following pages represents a first step in understanding the hydrologic role of faults in poorly consolidated sands.

GEOLOGIC SETTING

The Rio Grande Rift provides a generous field laboratory for testing whether small-displacement faults can significantly alter the permeability of poorly consolidated sands. Intermittent crustal extension over the last ~30 million years (Ma) has created thick basin fill deposits and large numbers of faults in the rift's central NM basins (Kelley, 1977; Chapin and Cather, 1994; Cather et al., 1994; Hawley and Cather, 1996). Sands are observed throughout the Santa Fe unit, but well sorted sands are particularly frequent in the younger Santa Fe deposits (Hawley and Haase, 1992; Hawley and Cather, 1996). Fault displacements from hundreds of meters to centimeters have been observed in these younger sands (Heynecamp et al., 1995; Mozley and Goodwin, 1995).

Abutting the Colorado Plateau, the Basin and Range physiographic province, and the continental craton, the Rio Grande rift runs more than 1000 km from south-central Colorado into northern Mexico. The rift expresses itself within central New Mexico as several west-stepping, *en echelon* basins, including the Albuquerque and Socorro Basins (Figure 1). Crustal extension, most of which occurred during the Miocene but began in the late Oligocene, and rotation of the Colorado Plateau downdropped the basins (Chapin and Cather, 1994). Although the majority of the basin fill was laid down in the Miocene, deposition of the Santa Fe Group continued until the Rio Grande became a through-flowing river during the Plio-Pleistocene (Kelley, 1977; Hawley and Haase, 1992; Cather et al., 1994; Chapin and Cather, 1994; Lozinsky, 1994). Fluvial sands and gravels, sandstones, flood plain silts and clays, fanglomerates, mudstones, siltstones, playa deposits, eolian sands, and volcanics (basalts and tuffs) are all elements of the Santa Fe Group (Kelley, 1977; Hawley, 1978a; Hawley and Haase, 1992; Hawley et al., 1996). Late and post-Santa Fe Group fluvial deposits, e.g., ancestral axial Rio Grande channel deposits and Plio-Pleistocene sands and

FIGURE 1: Rio Grande Rift Basins of New Mexico.
Adapted from Russell and Snelson, 1994.

gravels, provide the most productive aquifers within the Albuquerque Basin (Hawley and Haase, 1992; Hawley et al., 1996). Many researchers have sought to identify basin-wide consistent members of the Santa Fe Group, but the complexities in timing and rates of faulting, erosion, and tilting have created such strongly localized variability that identification of members is problematic (Cather et al., 1994). Faulting continued throughout the Quaternary after large-scale sedimentation had ceased as demonstrated by the large number of faults displacing late and post-Santa Fe deposits (Kelley, 1977; Machette, 1982; Chapin and Cather, 1994).

The Albuquerque Basin, one of the largest and deepest of the rift's New Mexico basins, comprises an east-tilted, northern half-graben separated from a west-tilted southern half-graben by an accommodation zone which may be an extension of the Tijeras Fault (Russell and Snelson, 1990 and 1994). The basin is estimated to have undergone 17% extension across its northern sub-basin and nearly 30% across the southern sub-basin (Russell and Snelson, 1990 and 1994). Large, mappable faults are numerous throughout the basin (Figure 2), though they are better exposed in more indurated rock, such as the Santa Ana basalt flow northwest of Bernalillo, NM, than in the poorly consolidated Santa Fe Group sediments. Syn-rift Santa Fe Group thicknesses vary from less than 600 m to more than 4000 m within the basin (May and Russell, 1994).

The Socorro Basin appears to possess a more complicated structure than its northern neighbor because the Popatosa Basin, precursor to the modern-day basins, underwent 50% extension during Oligocene and Miocene times (Chamberlin and Osborn, 1984; Chapin and Cather, 1994). The Popatosa Basin split into the La Jencia and Socorro west-tilting, half-graben basins with the uplift of the Lemitar-Socorro Mountains during the Miocene (Cather et al., 1994). The second study site lies in the southern end of the Socorro Basin, where it opens into the Jornada del Muerto and San Marcial Basins. Far fewer subsurface or surface geologic data are available for this area, compared

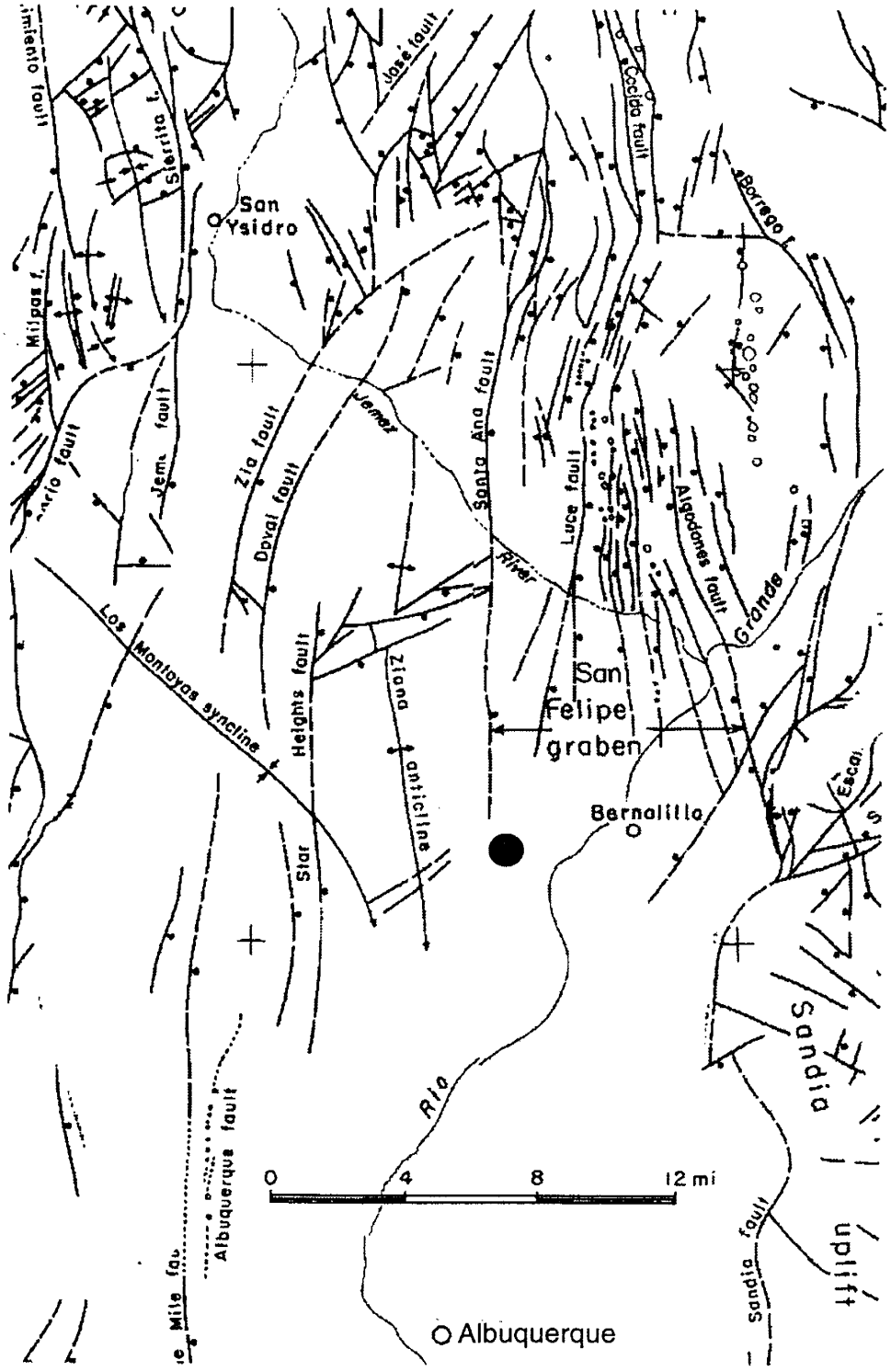

FIGURE 2: Fault Map of Northern Albuquerque Basin.

Lines with dots represent faults; dot indicates downthrown side. Large black dot shows approximate location of Santa Ana study site. Adapted from Kelley, 1977.

to the Albuquerque Basin, but faulting has continued throughout the Quaternary (Machette, 1982; Cather et al., 1994; Lewis and Baldridge, 1994). Basin-fill thickness is believed to vary from 300 to 3000 m (Chapin et al., 1978). The Albuquerque Basin's relatively high permeability Upper Santa Fe member is given the name Sierra Ladrones within the Socorro Basin. The lower and middle Santa Fe members are named the lower and upper Popatosa Units.

Elmendorf Site

Located 200 km south of Albuquerque, NM in the Socorro Basin, the first study site is part of an extensive fault zone found near the southern boundary of the Bosque del Apache Wildlife Refuge. The outcrop lies on the west side of NM Route 1 immediately north of the railroad bridge and less than two km west of the modern Rio Grande (Figure 22 in Appendix I). The primary facies consists of a fine-grained, well sorted, moderately indurated, buff sandstone. It is overlain by a thin (< 1 m) layer of colluvium. Facing southeast, the outcrop is oriented N 60°E - S 240°W and has a vertical slope of approximately 80 degrees. Its length is approximately 25 meters and it attains its greatest height of roughly 12 meters near its mid-point. The study site covers a five meter section near the southern end of the outcrop.

Large scale (4 - 8 m) tangential cross-stratified and planar bedding structures are readily observable immediately north of the study site (Figure 3). The cross-bed sets dip steeply at the top and are tangential at the base. The bedding structures to the south and within the fault zone comprise much smaller (roughly 0.5 m) and fainter tangential laminae. Longer (0.5 - 1.5 m) tangential laminae, oriented perpendicular to the study site outcrop face, are present within an erosion cut at the northern edge of the study site. The study site sets do not dip as steeply near the top as those to the north but are tangential at the base. Laminae are poorly defined with gradational contacts. Sand grain sizes range between 1.5 and 3.0 phi units (0.125 mm to 0.354 mm). Calcareous cemented beds and concretions are present along several horizontal planes (Figure 3).

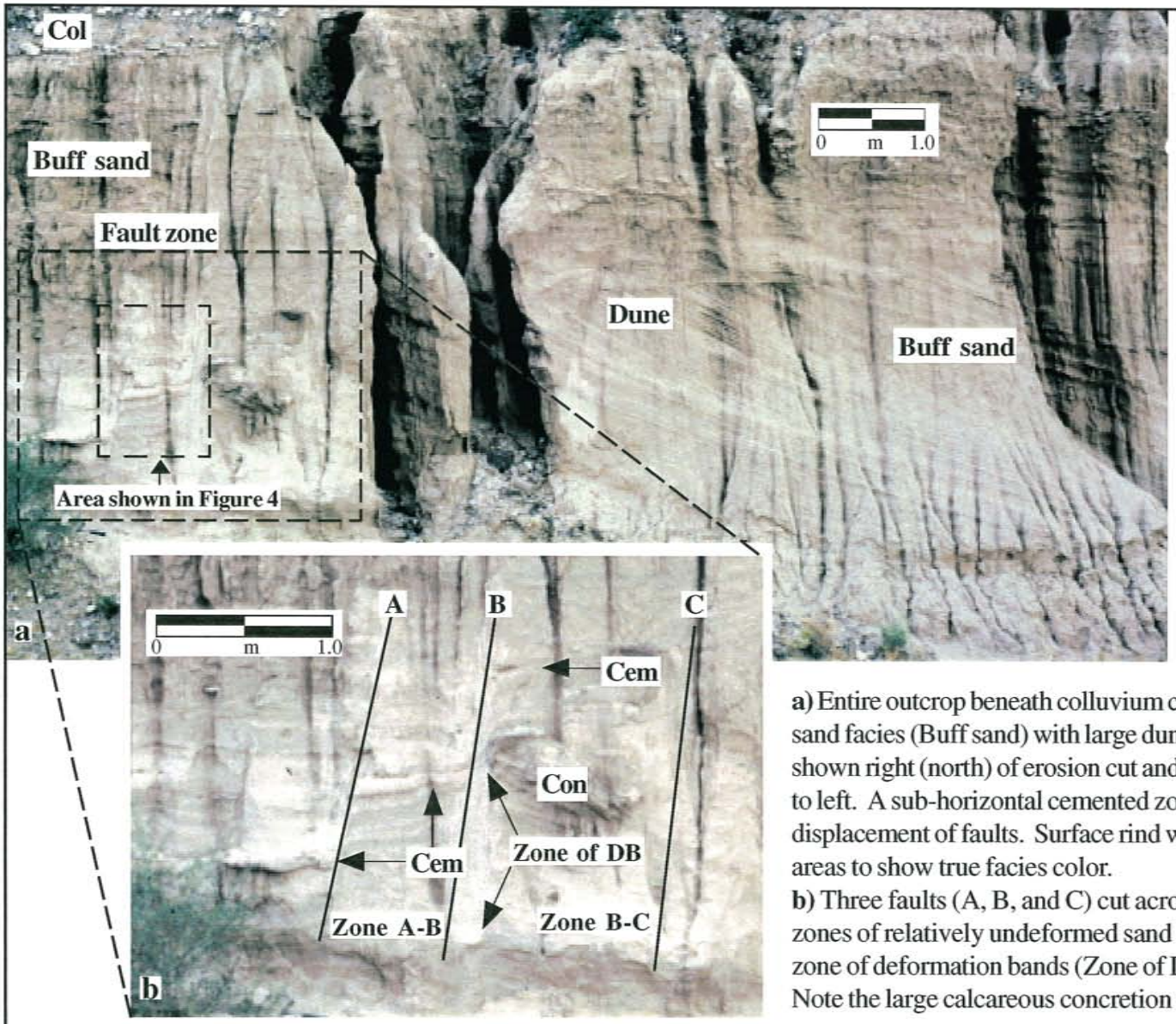

FIGURE 3: Elmendorf Lithology and Fault Zone Structure.

a) Entire outcrop beneath colluvium cap (Col) consists of buff fine sand facies (Buff sand) with large dune cross-bedding (Dune) shown right (north) of erosion cut and smaller dune cross-bedding to left. A sub-horizontal cemented zone (Cem) marks vertical displacement of faults. Surface rind was removed from bright areas to show true facies color.

b) Three faults (A, B, and C) cut across outcrop, separating zones of relatively undeformed sand (zones A-B and B-C). A zone of deformation bands (Zone of DB) lies adjacent to fault B. Note the large calcareous concretion (Con) within zone B-C.

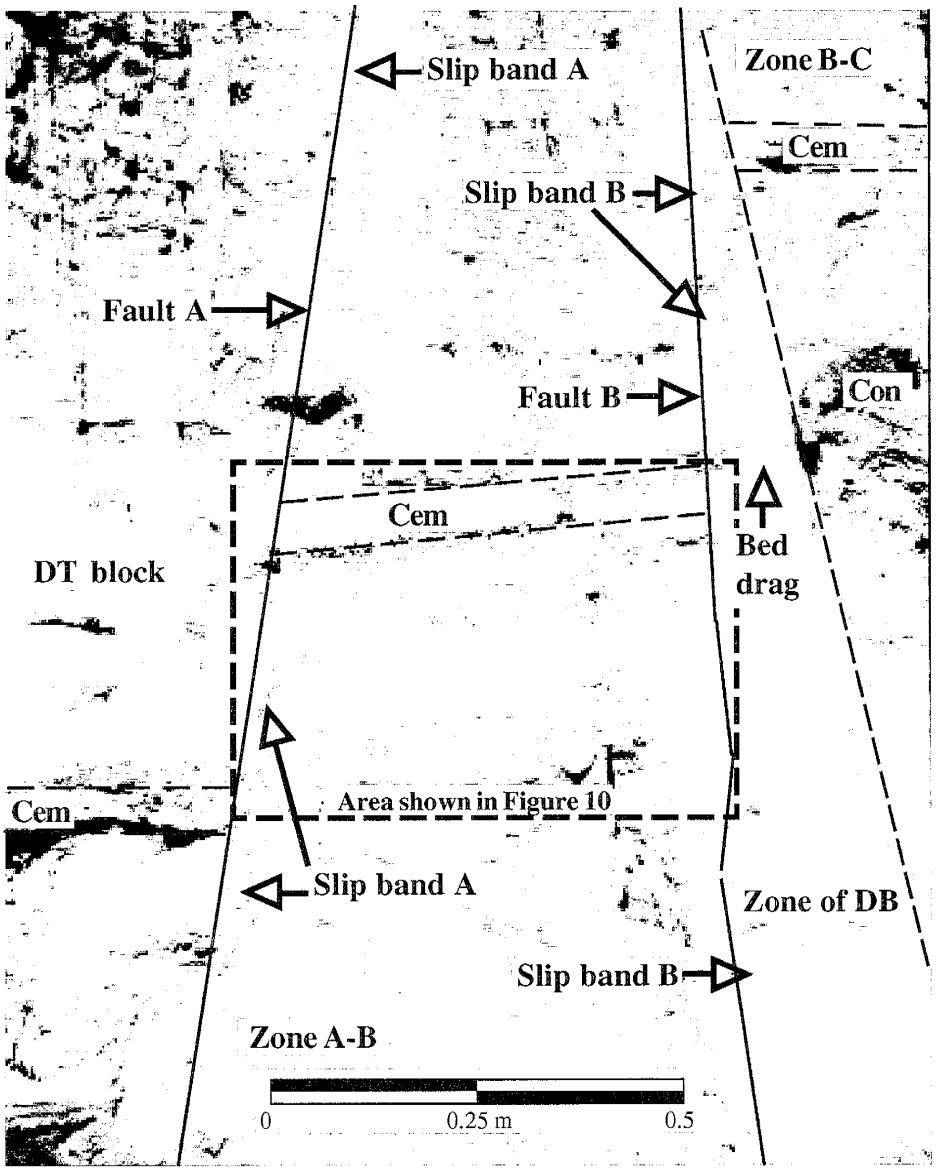

Figure 4: Detailed Elmendorf Fault Zone Structure. Solid black lines (Faults A and B) stand to immediate left of slip bands A and B, which are < 1.5 cm wide. Slip band A separates downthrown block (DT block) from zone A-B; slip band B lies between zone A-B and zone of deformation bands (Zone of DB). Sub-vertical white traces are most numerous within the zone of deformation bands but occur within the two zones of undeformed sand. Note zone of deformation bands pinches out near top of figure and widens towards the bottom. Zone B-C is located to right of zone of deformation bands. Gray fine-medium sand with planar bedding in center of zone A-B is shown deformed and dragged (stair-step structures) within the zone of deformation bands (Bed drag). Cemented bed (Cem) marks vertical displacement for each fault. Part of large concretion (Con) is shown at far right in zone B-C.

The outcrop has been identified as part of the Popatosa or lower member of the Santa Fe Group, dating back to the Miocene (Davis, 1994). It is interpreted to be of eolian origin based on the maturity, excellent sorting, large scale dune-bedding structures, and dip orientation of the tangential laminae sets (Davis, 1994).

Three high angle faults: A, B, and C, cut across the study site and separate the upthrown and downthrown blocks from two pods of relatively undeformed sand - zones A-B and B-C (Figure 3 and Figure 4). Each fault is the result of < 1 m of vertical displacement as estimated from separations between cemented marker beds and concretions. No slickensides or horizontally displaced correlative features were observed, which precludes determination of whether strike-slip displacement had occurred. Dips range between 65 - 75 degrees. All three fault dips fall within the range associated with normal faults in extensional regimes.

Each fault consists of a narrow quasitabular zone within which shear displacement has been accommodated (Figure 4). These bands of displacement accommodation vary in width from 5 to roughly 15 mm, extend from the bottom to at least 4 m up the outcrop, have only minor changes in dip, and display reduced grain size but increased induration relative to the surrounding sand. Band width and induration appear to vary along dip.

These structural features resemble in appearance the deformation bands reported by Aydin (1978) for the porous and well indurated sandstones of southeastern Utah (Navajo and Entrada Formations) as well as the cataclastic slip bands observed by Fowles and Burley (1994) in the high porosity eolian sandstones of northwest England and southwest Scotland (Penrith Formation) . The structures described by these authors were restricted to shear displacements on the order of 1 - 2 centimeters or less whereas the vertical displacements observed at the Elmendorf site are at least an order of magnitude larger and thus commensurate with the range of displacements expected for the

zones of deformation bands and slip surfaces reported for the Navajo and Entrada sandstones (Aydin and Johnson, 1978) or the cataclastic slip zones of the Penrith Formation (Fowles and Burley, 1994). As defined in numerous studies of porous, well indurated sandstones, a slip surface is a through-going, striated plane of negligible width demarcating a discontinuity in shear displacement (> 1 m) between the two fault blocks whereas a zone of deformation bands (or a cataclastic slip zone) contains two or more deformation bands (cataclastic slip bands) which share the same strike and dip (Aydin and Johnson, 1978 and 1983; Antonellini and Aydin, 1994; Fowles and Burley, 1994; Antonellini and Aydin, 1995). However, the fault structures observed at the Elmendorf site do not have negligible widths, unlike slip surfaces, and multiple deformation bands are not visible within them, unlike zones of deformation bands. Accordingly, the term: *slip bands* is introduced to describe these quasitabular zones of shear in poorly consolidated sands.

The slip band for Fault A is a sub-vertical planar band, 7 to 13 mm wide, and better indurated than the sands on the upthrown and downthrown blocks (Figure 3 and Figure 4). Shear displacement was accommodated within the band by fracturing of grains leading to grain size reduction. Petrographic analysis (see the Results chapter) shows evidence of both cataclasis and compaction. Based on measurements of displaced beds, Fault A accommodated 54 cm of vertical slip. Zone A-B, appears to have undergone little deformation beyond formation of numerous deformation bands (Aydin, 1978) which appear as sub-vertical, white traces and bed drag at its intersection with Fault B (Figure 4). The slip band for Fault B is a white, sub-vertical band which is slightly narrower and less well indurated than slip band A, although grain size is reduced relative to undeformed sand. Adjacent to slip band B is a zone of white, sub-vertical traces which begins part way up the outcrop and reaches its greatest width of 22 cm near the bottom of the outcrop (Figure 4) and is interpreted as a zone of deformation bands (Aydin, 1978). The zone is more indurated than the parent sand. Displaying a stair-stepped appearance, beds (which can be traced to Zone B-C and part way back to Zone A-B)

accommodated a vertical displacement of 20 - 25 cm through both shear displacement and bed drag within the zone of deformation bands (Figure 4). Total vertical displacement across Fault B is 60 cm, which suggests that slip band B accommodated 35 - 40 cm of vertical shear displacement. Zone B-C is roughly a meter in width, has relatively undisturbed planar bedding, and contains a large concretion (Figure 3). The slip band for Fault C, which bounds Zone B-C on the north, has a width which ranges between 0.5 and 1 cm. It, too, is better indurated than the surrounding material. Total vertical displacement across Fault C was not estimated because no marker beds or other correlative features were observed at the outcrop.

The outcrop is interpreted to be part of the Elmendorf Fault zone (D. Love, personal communication, 1996) which comprises a complex series of relatively small-displacement faults at both the study outcrop and a long, east-west oriented, faulted outcrop further to the east (Figure 22). Faulting is interpreted to have occurred during the Miocene based on observations of fault termination within the first few feet of Miocene age alluvial fan facies which cap the same buff eolian sand facies at another Elmendorf outcrop located a few hundred meters from the study site.

Santa Ana Site

The second study site is found on the bank of an active arroyo in the Albuquerque Basin approximately 100 meters south of Idalia Road and approximately five km (three miles) west of NM 528 (see Figure 23 in Appendix I). Idalia Road is located in the City of Rio Rancho roughly 6.4 km (four miles) south of the junction of NM 44 and NM 528, some 32 km (20 miles) north of the City of Albuquerque. Facing north, the outcrop is L-shaped with a total length of roughly 10 meters and a maximum height of four meters. The study site is located along the easternmost five meters of the outcrop and is oriented N 50° E - S 230° W with a vertical slope of approximately 90 degrees.

Cutting across its center, the outcrop is separated by a fault zone into two blocks, each of which exposes several facies (Figure 5). The upthrown fault block consists of roughly 2 m of buff fine sand

overlain by ~ 1.5 m of fine-medium red sand and a thin (<0.5 m) layer of colluvium. The downthrown block consists of approximately 2 m of buff fine sand overlain by a thick (~1.5 m) red-brown clay bed, 0.5 meter of well-cemented (calcite) coarse red sand, and <0.5 m of colluvium.

The most prominent facies, the buff fine sand, is well sorted and massively bedded with no observable laminae. Sand grain sizes range between 2.0 and 3.0 phi units (0.125 mm to 0.250 mm) and grains are sub-rounded. There is little difference in either bedding or grain size between the upthrown and downthrown buff fine-grained sands, but they are likely not from the same stratum given the most probable minimum fault displacement (see below).

Two planes of calcareous concretions cut across the buff fine-grained sand unit on the downthrown block. The lower plane extends across nearly the full length of the base of the block, varying in width between 10 and 30 cm. The upper plane is found roughly 30 cm beneath the clay bed. It thins from approximately 35 cm at the center of the block to 2 - 5 cm at either end, where fault slip is evident. The upper calcareous plane appears to sharply switch from a sub-horizontal to sub-vertical orientation where it meets the boundary of the fault zone (Figure 6). This "re-orientation" most likely did not occur during slip because the re-oriented cemented layer shows no signs of the fracturing expected from displacement. The angled cemented layer may have been created by precipitation of new calcareous cements from the increased fluid flow associated with slip events (Sibson, 1981; Edwards, et al., 1993) or from preferential flow paths created by a juxtaposition seal. A 30 cm long, sub-vertical possible rhizoconcretion can be seen in Figure 5. Numerous other small calcareous concretions ($\leq$ 5 cm in greatest dimension) are distributed across the downthrown block.

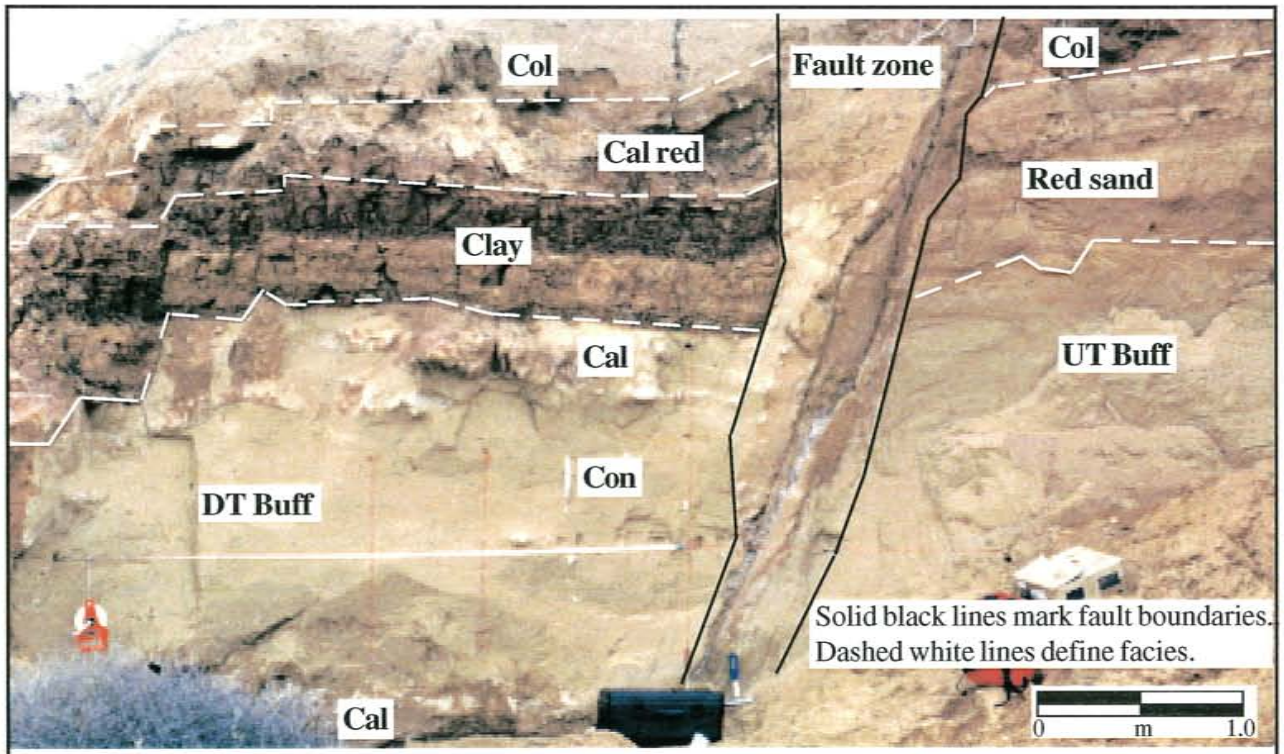

FIGURE 5: Santa Ana Lithology. Downthrown buff fine sand facies (DT Buff) overlain by red-brown clay bed (Clay), calcite-cemented coarse red sand (Cal red), and colluvium (Col) comprise the downdropped block, shown left (east) of the fault. Upthrown block shows buff fine sand (UT Buff) overlain by red fine to coarse sand facies (Red sand) and colluvium. Two horizontal, calcareous cemented zones (Cal) cut across the buff sand facies on the downthrown block and several white concretions, including a vertically-oriented concretion (Con), are also visible. Note smaller downdropped blocks in clay facies to the left. The horizontal white line across the downthrown block is a tape measure. The outcrop faces roughly to the north.

FIGURE 6: Structure of Santa Ana Fault Zone.

Solid black lines delineate fault zone; dashed white lines define deformed zones.

Undeformed buff sand (Buff) is downthrown (DT) to left (east) of and upthrown (UT) to right (west) of fault zone. Slip bands (SB) A and B, which appear as white bands, bound the fault zone. The main slip surface (SS) lies within the clay core (CC), which splays off (CC Splay) and surrounds a pod (Pod) of mixed sand and clay. Deformed zones Buff 1 (B1) and Buff 2 (B2) surround the better-indurated Red 1 (R1) and Red 2 (R2) deformed zones, which sandwich the clay core. Located between R2 and B2, the cataclasite (Cat) zone is the most indurated deformation structure. Calcite concretions (Con) appear as white patches. White deformation bands (DB) appear in and out of the fault zone.

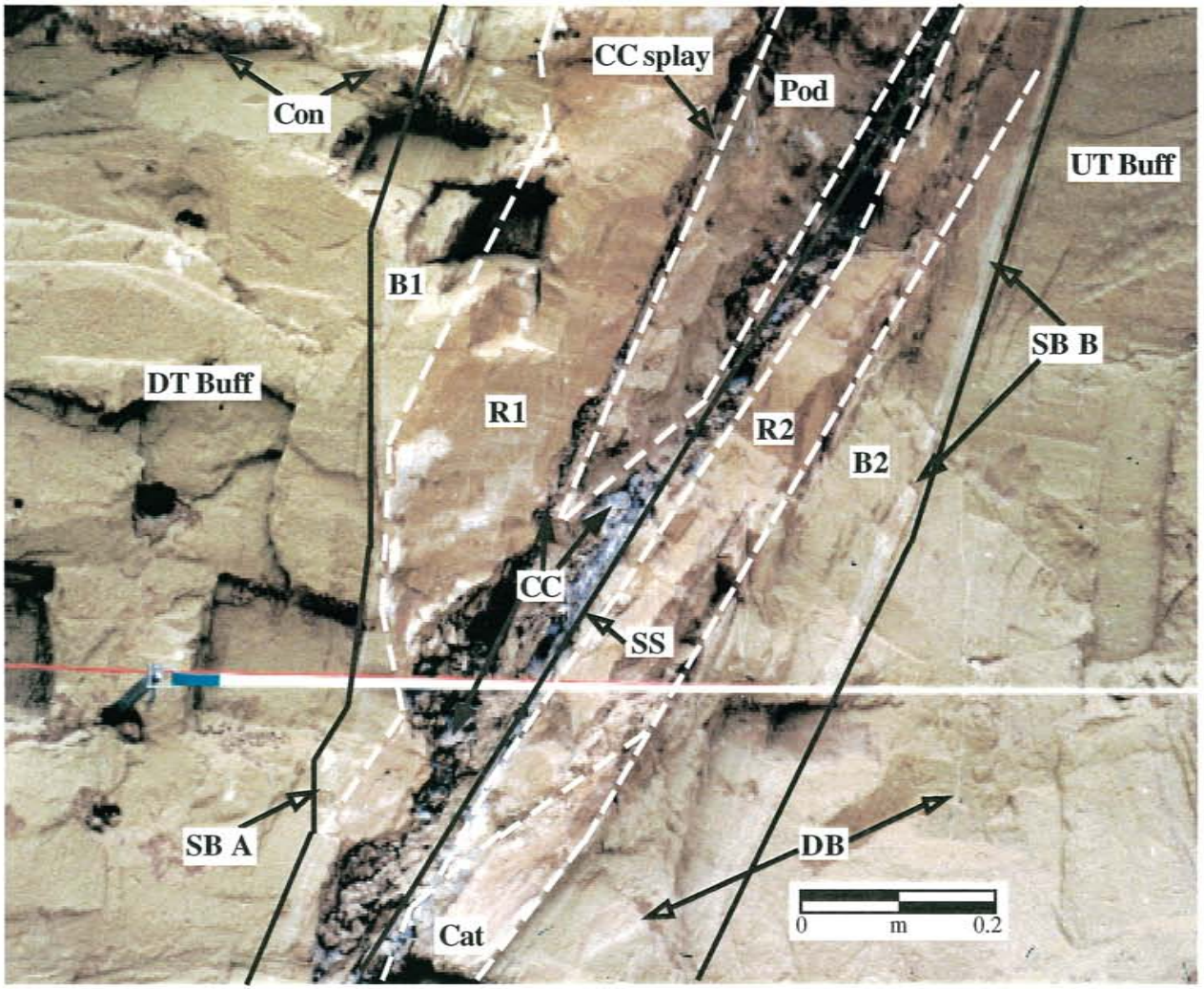

Extending across the entire upthrown block, the red fine-medium sand facies displays planar bedding. Small scours with gravel, coarse sand, and clay envelopes are observed along the erosional contact with the buff fine-grained sand facies. Average grain size (0 - 2.5 phi units) is larger than that for the buff fine-grained sand facies.

The distinctive red brown clay facies consists primarily of clay with thin interbedded sands. It is only present in the downthrown block and is truncated by the fault. Mottled areas, common throughout the bed, typically contain a large amount of sand, possibly indicating bioturbation.

The outcrop is interpreted to be part of the upper Santa Fe Group (J. Hawley, personal communication, 1994). Kelley (1977) mapped the area surrounding this branch of the Arroyo de Barranca as a Quaternary eolian sand facies; however, upsection outcrops expose mainly fluvial sands and muds with occasional eolian interbeds. The gravel scours, grain size mean and range, bedding, and clay envelopes observed in the red fine-medium sand facies suggest it originated from a moderate energy fluvial depositional environment. The clay bed is interpreted as originating from a lower energy fluvial environment based on its very fine mean grain size, bedding structures, and the indications of bioturbation. The massive buff sands observed in both fault blocks are interpreted as an eolian reworking of fluvial deposits because clasts too large for eolian transport are found scattered throughout the facies and because the apparent lack of bedding structure is more likely the result of eolian than fluvial transport.

A sole slip surface cuts through the center of the fault zone from the outcrop bottom to the colluvium. It strikes N 20° E - S 110° W, and dips 70° along its upper extent (Figure 5). Dip decreases along the lower-most half meter of the outcrop. Fault zone width is greatest (~1 m) along most of the fault's upper extent then narrows to 10-15 cm along the lower-most half meter of the outcrop (coincident with the change in fault dip). The eastern fault block is interpreted as the

downthrown block because the thin, horizontal beds of the western block's red medium-fine sand unit are dragged down into the fault zone. Two white sub-vertical bands with varying width (1 - 3 cm) and dip form the contacts between the fault zone and the two blocks (Figure 5 and Figure 6). These two bands are interpreted as slip bands because of their increased induration and evidence of a slight grain size reduction. Slip band A forms the contact between the fault zone and the downthrown (eastern) block, truncating the clay bed, and contains several small (< 8 cm) cemented pods or concretions (Figure 5 and Figure 6). Slip band B separates the upthrown (western) block from the fault zone (Figure 5 and Figure 6); along its bottom ~30 cm, it changes appearance from a uniformly white band to a zone of deformation bands because buff sand is visible between the 5 - 8 white deformation bands, each of which is 1 - 2 mm wide. Several other minor displacement slip surfaces are visible along the easternmost part of the study site, giving the red brown clay bed a stepped appearance (Figure 5).

Absence of observed correlative features precludes accurate estimation of total vertical displacement across the fault zone. Furthermore, the massive bedding of the buff fine sand units lacks any distinctive features with which to estimate vertical shear displacement across either of the two slip bands. Although the site was initially interpreted as a small displacement fault, the minimum amount of vertical displacement is estimated to be 3 to 3.5 m by assuming the ~1.5 m thick fine to medium grained sand and ~2 m thick buff fine sand units observed on the upthrown block lie just beneath the buff fine sand unit on the downthrown block.. There are no data to constrain the maximum amount of vertical displacement. Even though this fault does not fit this study's definition of a small displacement fault, it provides a useful contrast to the small displacement Elmendorf fault zone.

The Santa Ana fault zone displays a much more complicated structure than the Elmendorf fault zone (compare Figure 5 with Figure 3 and Figure 6 with Figure 4). The fault zone comprises a slip surface, a dragged clay bed, numerous deformation bands, two slip bands, and five elongate, parallel

to dip, sub-vertical zones which vary in width, color, induration, and grain size. Each of these components is described below.

Adjacent to the slip surface lies a 1 - 15 cm wide sub-vertical band of red brown clay (Figure 6). Cracked and friable, this fault clay core follows the slip surface along the entire height of the fault with a splay that branches out and rejoins the fault clay core within the uppermost 2 - 3 m of the fault zone. An elongate pod of red brown sand and clay, oriented sub-parallel to fault dip, is circumscribed by the clay core and its splay.

The clay core and its splay separate the fault zone into two asymmetric pairs of elongate, parallel to fault dip, sub-vertical zones which differ in color and induration. Slip band A separates the downthrown block from an elongate, parallel to fault dip zone of buff fine sand (buff 1) which varies in thickness between 0 and 15 cm (Figure 6). The zone closely resembles the undeformed buff fine sand of the downthrown block in color and grain size, but is slightly better indurated. An elongate parallel to fault dip zone of red, more indurated sand (red 1) is bounded by the buff 1 zone and the clay core. The red 1 and buff 1 zones give no evidence of bedding and may have originated from a unit with massive bedding such as the buff fine sand units. They also share a sharp, stair-stepped contact which contains several small calcite concretions. A second pair of red and buff zones (red 2 and buff 2) are present on the upthrown side of the fault clay core with widths ranging between 2 - 25 and 0 - 15 cm, respectively (Figure 6). As with their downthrown counterparts, the red 2 zone is better indurated than the buff 2 zone, which in turn is slightly better indurated than the undeformed buff fine sand of the upthrown block. The red 2 zone consists of sub-vertical, parallel to fault dip, bedding-like structures which vary in width, color, grain size, and induration. At least one of these bedding-like layers appears to contain primarily the fine to medium grained red sand from the upthrown block, which suggests the possibility that the structures were formed by bed drag. White deformation bands, 1-3 mm thick, have two major orientations: sub-parallel to fault dip and roughly

perpendicular to fault dip, forming a fairly regular network across both pairs of zones. Average grain sizes appear to be relatively unchanged in the buff zones and slightly reduced within the red zones.

Evidence collected to date is not sufficient to conclusively identify which mechanisms created the red and buff zones within the Santa Ana fault zone; however, there are enough data to encourage speculation. It is possible that bed drag created the red 2 zone (upthrown side) because its multiple layers are oriented parallel to fault dip and contain differing colors and grain size means and ranges; perhaps each layer corresponds to a different source bed or different degrees of mixing. Cataclasis was not an important formative process because there appears to be little or no change in grain size within the four zones. The structureless bedding of the two undeformed (outside the fault zone) buff fine sand units precludes determining in the field whether the buff 1 and 2 zones experienced any deformation; they may be the product of drag associated with formation of the slip surface or of subsequent slip movement. The relatively homogeneous nature of the red 1 and buff 1 zones and their sharp stair-stepped contact suggest that if the two zones were formed together with the slip surface then they are not the product of bed drag. A more likely explanation is that the two zones were separated by fault slip after formation of the slip surface. They may have been created with the slip surface through bed drag or some other process, later fault slip created the observed network of deformation bands. One or more unknown diagenetic processes changed the color from buff to red (and induration) of the section closest to the fault but was then impeded from altering the current buff 1 zone by the thicker deformation bands which form the present contact between the two zones. In general the two pairs of zones display some evidence of deformation through bed drag (red 2 zone) and shear displacement (deformation bands and slip bands).

Induration reaches a maximum within a 15 cm wide by 40 cm long pod oriented parallel to fault dip and sandwiched between the red 2 and buff 2 zones (Figure 6). Consisting of reddish-brown, very well-mixed fine sand and clay, the pod has a much smaller average grain size than found in any of the

other fault zone structures. It is interpreted as a cataclasite because of the substantial reduction in grain size. Petrographic analyses (see the Results chapter) provide additional confirmation that grain size decreases substantially within the cataclasite pod.

The fault is interpreted as the southern tip or a splay of the major intrabasinal Santa Ana fault based on its strike and a recent mapping of the southern Santa Ana fault trace several kilometers to the north (J. Hawley, personal communication, 1996). Other possibilities include identifying the study site fault as an isolated fault of unknown displacement or as a southern segment or splay of the intrabasinal Luce fault, which lies just to the east of the Santa Ana (Figure 2). Faulting occurred during the late Pliocene based on dating of a pumice bed displaced by a fault considered to be a segment of the study site fault (J. Hawley, personal communication, 1997).

METHODS

The primary hypothesis: faulting can significantly change the permeability of poorly consolidated sands, was tested by measuring the permeability of deformed (faulted) and undeformed poorly consolidated Santa Fe Group sands from the Rio Grande rift. Permeability measurements were limited to small-scale in-situ samples (≈ 1-10 cc) collected with two portable mini-permeameters. Several measures of spatial variability in permeability (e.g., semi-variograms, non-ergodic covariance) were used to investigate the importance of spatial heterogeneity on comparing undeformed-zone and fault-zone permeability. Testing of the second hypothesis, permeability change within poorly consolidated sand fault zones was caused by deformational and diagenetic processes, was achieved through petrographic analysis. Point count, X-ray diffraction, and scanning electron microscopy techniques were used to identify the deformational and diagenetic processes responsible for differences in permeability and porosity observed between deformed and undeformed sands.

Geologic Mapping

Two Santa Fe unit outcrops containing well exposed, small-displacement faults were identified within the Albuquerque and Socorro basins of the central NM Rio Grande rift. Outcrops were selected for nearly vertical outcrop face, limited number of lithofacies, and horizontal extent sufficient to characterize the spatial variability of the parent material's permeability.

Lithofacies and sedimentary structures were mapped at each outcrop. Mean grain sizes were estimated using comparators. Transect lines were set along each of the outcrop faces, providing a local two dimensional coordinate system for locating measurements and samples. Fault zone structures such as deformation bands, slip surfaces, zones of deformation bands, slip bands, and pods of relatively undeformed sediment were identified and mapped at each site.

Measurement of Permeability

The primary hypothesis was tested through determination of the permeability difference between the deformed and undeformed zones at each site. The permeability difference is defined as significant if there is little overlap between permeability distributions observed for deformed and undeformed sands. To be significant a difference in mean permeability (or log10 permeability) must exceed measurement error and zone-specific local variations in permeability. A large difference between deformed and undeformed sand is not significant if the undeformed sand's permeability varies just as widely across the outcrop because of local variations (e.g., cementation).

Air and gas mini-permeameters were used to measure the permeability within each zone. Mini-permeameter measurements provide a rapid field means to determine saturated (single fluid-phase flow) permeability values in a variety of rocks (Goggin, et al., 1988ab; Chandler et al., 1989; Dreyer et al., 1990; Davis et al., 1993, 1994; Antonellini and Aydin, 1994). A gas permeameter typically consists of a tip seal, gas or air supply (compressed gas tank or syringe), and a means of determining gas flow rate and pressure behind the tip seal or some surrogate of these. Using a modified form of Darcy's Law, permeability is computed as a function of the differential between absolute atmospheric pressure and the pressure behind the tip seal, gas flow rate, temperature, gas viscosity, tip seal geometry, and the sample or sample location geometry (Goggin et al., 1988a; Davis et al., 1994). The observed permeability is also a function of the pressure applied to hold the tip seal against the outcrop face (Tidwell and Wilson, 1997). The rock volume interrogated by the mini-permeameter is a function of the tip seal size: typical sample volumes range from 1 to 7 cc. Initial experimentation indicated two mini-permeameters were required to adequately capture the wide range in permeabilities at each study site.

Two different mini-permeameters were used to estimate permeability of sands. Permeability of undeformed sands was measured with a syringe air mini-permeameter (SAMP) designed and

constructed at the New Mexico Institute of Mining and Technology (Davis, 1994; Davis et al., 1994). It measures the amount of time taken to deliver a constant volume of air from a glass syringe and was specifically developed for measuring the relatively high permeability (1 to 200 darcies) poorly consolidated sands and gravels of the Upper Santa Fe Group (Davis et al., 1993). The relatively low permeability of the deformed sands was measured with a continuous flow N_2 gas mini-permeameter (CFMP) developed at Sandia National Laboratories similar to the one described by Tidwell and Wilson (1997). This instrument directly measures the pressure behind the tip-seal and the gas flow rate. It has a permeability range in the field roughly between 0.001 and 5 darcies.

Measurements were taken along vertical and horizontal transects with standard spacing of 10 cm. More closely spaced measurements were required within the fault zones to adequately detail rapid changes of permeability. Nearly all of the measurements were made with the mini-permeameter tip seal oriented perpendicular to the outcrop face, i.e., roughly parallel to fault strike, and are referred to as "parallel to fault" permeability. A limited number of measurements collected on an exposed portion of slip band A at the Elmendorf site were oriented perpendicular to the fault plane and are referred to as "normal to fault" permeability. Measurements were also made on selected concretions and cemented zones for comparison purposes.

All sampling locations were scraped with a putty knife, trowel, or rock hammer and gently brushed to remove weathering effects, such as clay or silt wash, and loose grains prior to permeability measurement. Measurements were collected at least several days after a rainfall to allow the outcrops sufficient time to dry and thereby ensure that the confounding effects of moisture content on permeability estimation were negligible. Ambient air temperature was measured several times during each sampling date to help correct for changes in air (or gas) viscosity. Absolute atmospheric pressure measurements for Santa Ana were collected from the National Weather Service office at the Albuquerque International Airport for the Santa Ana site. An average of absolute atmospheric

pressure measurements made in Socorro during the previous year was used for the Elmendorf site because there is no source of daily measurements available.

Measurement error was quantified by recording a minimum of three replicates at each sampling location and by remeasuring selected locations at least once more each sample date. Selected sample locations were also measured on several different sampling dates. Repeated same-day measurements at individual locations were used to control for operator error and temperature-air viscosity variations. Measurements of individual locations repeated over several sampling dates were used to control for errors from variability in moisture content, absolute atmospheric pressure, and operator technique.

Observed permeability is inversely related to the tip seal application pressure - greater application pressures tend to improve the seal, which increases resistance to air or gas flow because less flow escapes to the atmosphere. Therefore, better seals tend to yield lower, more representative permeability measurements, but outcrop compaction occurs if too much tip seal pressure is applied to the sand. If a series of measurements showed a steady decrease in permeability, the sample location was scraped and brushed before resampling.

The relative importance of within-sample (i.e., replicate) and between-sample (i.e., location-specific) variances to total variance was estimated through single classification, random treatment analysis of variance (ANOVA). Each location is considered as a treatment, allowing comparison of replicate-based within-sample variability and location-based between-sample variability. The percent of variation among locations was calculated by dividing total variance into between-location variance (Sokal and Rohlf, 1981, page 216). The impact of multiple sample dates was also quantified by testing the hypothesis that all sampling dates (i.e., treatments) had equivalent means using single classification, random treatment ANOVA. All calculations were made using Microsoft Excel for Windows, version 5.0.

Measurement error was also controlled through the repeated measurement of small (~5 cm each side) Berea sandstone blocks and calibrated 100 cc artificially cemented sand cylinders which were manufactured at NM Tech (Davis, 1994). The manufactured sandstones, denoted as standards 21, 15, 11, and 2A, were used to calibrate the SAMP and the Berea sandstone blocks, labeled as R1, B1, and C1, were used to calibrate the CFMP instrument along with standard 21. The whole-sample permeability of the four manufactured sandstone standards had been determined previously using a continuous flow permeameter and a Hassler-type sleeve which formed a gas-tight seal around the stainless steel sample holders (Davis et al., 1994). The permeability of the Berea sandstone blocks was measured on the syringe air permeameter at the NM Tech Petroleum Resource Recovery Center (Suboor and Heller, 1995) and on a gas permeameter designed and built at Sandia National Laboratory (Tidwell and Wilson, 1997). The calibration standards were measured at the field site prior to every start of sampling at a minimum and often one or more additional times during each sampling date.

Replicate measurements were treated in two ways after removing measurements which indicated either a poor tip seal or outcrop compaction from the data set. First, each replicate was treated as an individual measurement and second, replicate measurements and their base 10 logarithms were averaged for each location measured. First treatment data, which yielded many observations for each sampling location, were used to estimate sampling error and variability. Second treatment data, which produced an average permeability and variance per location, were used as input to exploratory data analysis and variography. Descriptive statistics were calculated for second treatment data which had been grouped by zone, i.e., undeformed and fault zone, for each site (zonal permeability), and by fault-zone structure, e.g., slip band, cataclasite, etc.

To test whether the spatial variability of permeability within a zone might interfere with comparisons of permeability between undeformed and fault zones, e.g., if permeability differences

between zones were dependent on sample location, the spatial correlation structure of permeability within each zone was analyzed using geostatistical techniques. Sample semi-variograms and measures less sensitive to data clustering and extreme values were calculated separately for undeformed and deformed zones using mean permeability logarithms (second treatment) to determine the presence of any spatial correlation structure and an associated correlation length scale. The methods applied are described in Appendix II.

Petrography

Thin-Section Analysis

A total of seven outcrop samples, two from the Elmendorf site and five from the Santa Ana site, were collected for thin-section analysis. Samples were taken of both undeformed and deformed zones from each site. Table 1 lists the samples, their locations, and salient features. Cost constraints precluded collection of replicate samples. The individual undeformed sand samples are very likely representative of their respective units because the sands are well sorted and consistent in their bedding and average grain size. This consistency was further reinforced by the uniformity of the permeametry results (see the Results chapter). The samples were dried and then impregnated with blue-dyed epoxy. Standard size thin sections were prepared (one per sample), stained for potassium feldspar, and examined to qualitatively determine the following petrophysical characteristics:

- grain size reduction and changes in grain angularity;
- elongate grain re-orientation; and
- cementation.

Table 1: Thin-Section Sample Descriptions

THIN SECTION	SITE	DESCRIPTION[1]
OC1 A	Elmendorf	Undeformed area 20 cm left of slip band A
OC1 B	Elmendorf	Cuts across slip band A and undeformed Zone A-B.
OC2 A	Santa Ana	Cuts across 2 mm deformation band 1.5m east of fault zone
OC2 B	Santa Ana	Cuts across easternmost fault boundary and buff 1 zone
OC2 C (2)	Santa Ana	Cuts across contact between buff 1and red 1 zones
OC2 D	Santa Ana	Cuts across contact between cataclasite and buff 2 zone
OC2 E	Santa Ana	Cuts across contact between cataclasite and red 2 zone

[1] *See Figure 4 and Figure 6 for description of fault zone structures.*

Counts of 300 points were taken to estimate the abundance of quartz, K-feldspar, plagioclase, rock fragments, porosity, and clay-size fraction (csf) within deformed and undeformed zones. All observations were made using a Nikon petrographic microscope equipped with a mechanical stage driven by an electronic counter. Counts were collected for plutonic, metamorphic, sedimentary, and undifferentiated rock fragment types as well as chert, chalcedony, biotite, carbonate rock fragments, carbonate cement, undifferentiated carbonate fragments (detrital or cement), clay minerals, sericitization, and diagenetic alterations (e.g., replacement and light, moderate, and complete dissolution) of feldspars and rock fragments.

Porosity was classified as one of two types whenever a point count fell on blue-dyed epoxy: macro- porosity or micro-porosity. Macro- porosity was defined as an observation of wholly-blue epoxy with little or no clay-sized material apparent within an intergranular void. Micro-porosity was defined as an observation of small amounts of blue-dyed epoxy interspersed within clay-sized material or within an altered grain. When the cross-hair indicated both clay-sized material and blue-dyed epoxy the count was assigned to micro-porosity and clay-size fraction categories in an alternating

fashion. All counts, including assignment to micro-porosity/clay-size fraction categories, were made with the maximum available magnification of 400 diameters (400x), indicating the micro-porosity category had a minimum pore size of approximately 1 micron (10^{-6} m).

X-ray Diffraction of Clay-Size Fraction

Hand-sized samples collected from the Santa Ana Fault were examined to determine the mineral composition of the clay-size fraction. After disaggregation, the clay-size fraction was separated from the remaining sediments using a hydrometer, dried, and then analyzed using the X-ray diffraction equipment at the NM Bureau of Mines and Mineral Resources in Socorro, NM. The Bureau's X-ray diffraction equipment identifies the clay and other minerals found within the clay-size fraction and provides a semi-quantitative estimate of their abundance. Samples were collected from the clay bed capping the downthrown block, the undeformed sediments below it, and within the fault zone (Table 2).

Table 2: X-ray Diffraction Sample Descriptions: Santa Ana Site

Sample ID	Sample Location
GA95062	Undeformed buff sand - downthrown block
GA95057	Buff 1 zone - downthrown side
GA95061	Red 1 zone- downthrown side
GA95058	Cataclasite
GA95060	Fault clay core
GA95059	Clay bed overlying downthrown block

Scanning Electron Microscopy

Samples of undeformed and fault zone sediments were collected from both fault sites for examination using the University of New Mexico Institute of Meteoritics' (Department of Earth and Planetary Sciences) Hitachi S450 scanning electron microscope with secondary and backscattered

electron detectors under the direction of Dr. Michael Spilde. Each sample was cemented with epoxy to a stub, coated with gold and then placed into the SEM's vacuum chamber for imaging. Determination of the differences in clay-size fraction abundance, mineralogy, and distribution between deformed and undeformed zones was emphasized. Photomicrographs were taken as needed to document salient features.

RESULTS

Permeability

More than 1000 replicate permeameter measurements were collected at 146 sampling locations across the Santa Ana site and at 62 locations across the Elmendorf site. Nearly all measurements were made parallel to the respective fault (i.e., normal to the outcrop face) with the majority taken within the undeformed zones at each site. A total of 23 normal to fault replicate measurements at five locations in the Elmendorf fault zone were also collected. Data reduction through calculation of a mean permeability and mean log permeability for each sampling location (treatment 2) yielded 47 undeformed zone and 20 fault zone data points at the Elmendorf site versus 96 undeformed and 50 fault zone data points at the Santa Ana site (Table 3). The following discussion refers to these location-specific mean permeability and mean log permeability data unless otherwise stated.

At the Elmendorf site, parallel to fault permeability ranges between 4 and 12 darcies within the undeformed zone and between 0.2 and 10 darcies in the fault zone, yielding a span of roughly two orders of magnitude between the lowest fault-zone permeability and the highest undeformed-zone permeability (Table 3). Santa Ana site parallel to fault permeability ranges from 7 to 13 darcies in the undeformed zone and from 0.1 to 7.6 darcies in the fault zone, also giving a two order of magnitude span between the lowest fault-zone permeability and the highest undeformed-zone permeability (Table 3). The Elmendorf site undeformed-zone permeability average is roughly twice the fault-zone permeability average (7.9 versus 4.0 darcies, respectively) and the Santa Ana undeformed zone permeability average is roughly three times the fault zone permeability average (10.4 versus 3.0 darcies, respectively). The small difference between undeformed and fault zone permeability averages is attributed to the wide range of permeability observed within each fault zone.

Table 3: Summary Statistics for Parallel to Fault Permeability by Zone

	Average	Variance	CV*	Min	Median	Max	n
Elmendorf Fault							
Undeformed Zone (darcies)	7.9	3.6	0.25	4.2	7.7	12.3	47
Log_{10} Permeability	0.88	0.01		0.63	0.88	1.09	
Fault Zone (darcies)	4.0	14.6	0.96	0.2	4.4	9.8	15
Log_{10} Permeability	0.22	0.49		-0.71	0.64	0.99	
Santa Ana Fault							
Undeformed Zone (darcies)	10.4	1.5	0.12	7.7	10.4	13.6	96
Log_{10} Permeability	1.02	0.003		0.89	1.02	1.14	
Fault zone (darcies)	3.0	5.7	0.80	0.1	3.0	7.6	50
Log_{10} Permeability	0.25	0.29		-0.86	0.48	0.88	

**CV = Coefficient of Variation ≡ (standard deviation) (mean)$^{-1}$*

The hypothesis that the undeformed-zone and fault-zone log permeability averages originate from the same population (i.e., have an expected difference of zero) is rejected at the 95% confidence level by Student's t-test of means with variances assumed unequal for both the Santa Ana ($t_{observed} = 10.1$ versus $t_{critical}[\alpha = .025, 2\ tail] = 2.3$) and Elmendorf sites ($t_{observed} = 3.7$ versus $t_{critical}[\alpha = .025, 2\ tail] = 2.5$). Despite the relatively small difference in undeformed-zone log permeability averages for the two sites (1.02 versus 0.89 darcies for Santa Ana and Elmendorf sites, respectively), the hypothesis that the log permeability averages originate from the same population is rejected at the 95% confidence level by Student's t-test of means with variances assumed unequal ($t_{observed} = 8.1$ versus $t_{critical}[\alpha = .025, 2\ tail] = 2.3$). The same hypothesis for the two fault-zone log permeability averages, however, is not rejected by a similar t-test of the sample means ($t_{observed} = 0.1$ versus $t_{critical}[\alpha = .025, 2\ tail] = 2.4$).

Undeformed-zone log permeability distributions display very narrow ranges and very small variances relative to the fault-zone log permeability distributions (Table 3 and Figure 7). Based on

probability-scale plots, which display normal distributions as straight lines, undeformed-zone log permeability data from both sites appear to originate from normal distributions, i.e., the observed undeformed-zone permeability distributions are log normal (Figure 8). Sample cumulative frequency curves for undeformed-zone log permeability closely match cumulative normal distribution frequency curves computed using the observed sample means and variances, whereas the fault-zone sample cumulative frequency curves do not match at all (Figure 9). Further supporting the case for the normality of undeformed-zone permeability, Kolmogorov-Smirnov test statistics reject the hypothesis that the observed undeformed-zone log permeability distributions differ from those expected from normal distributions with equivalent moments, because the differences are no larger than those anticipated from random fluctuations given a 95% confidence level. The cumulative frequency curves for undeformed zone permeability do not match their associated normal cumulative frequency curves as well as the log permeability data (Figure 9), but the Kolmogorov-Smirnov test statistics for undeformed-zone permeability from both sites cannot disprove that the measurements also originate from normal distributions.

Unlike the unimodal undeformed-zone permeability distributions, fault-zone permeability measurements display bimodal distributions in the probability and histogram plots (Figure 8 and Figure 9). The two modes are attributed to distinct permeability ranges associated with fault-zone deformation structures (e.g., slip bands, cataclasite, zone of deformation bands, etc.) and relatively undeformed zones, similar to horses. Observed cumulative frequencies for both fault-zone permeability distributions differ from those expected for normal distributions with equivalent moments according to Kolmogorov-Smirnov test statistics at a 95% confidence level.

Elmendorf fault-zone structures with the greatest extent of deformation exhibit the lowest permeability values relative to the undeformed sand. The lowest permeabilities are found within the narrow, sub-vertical slip bands: slip band A, which accommodated the greatest amount of vertical

Figure 7: Box Plots of Log Permeability by Zone

Boxes encompass 50% of data; bars show extrema. Box widths are proportional to the square root of n for each group.

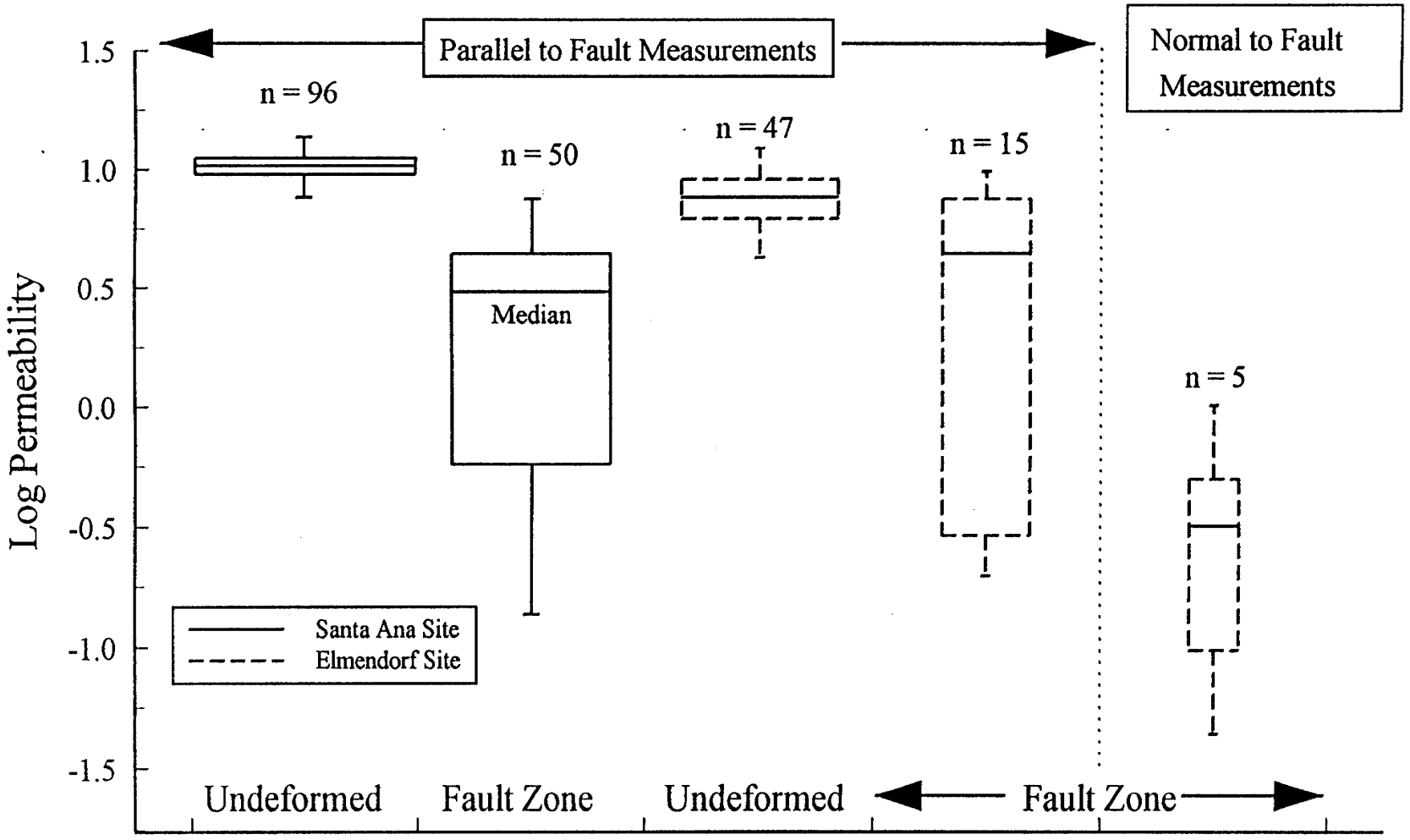

Figure 8: Probability Plot of Log Permeability by Zone

All measurements were made parallel to the fault.

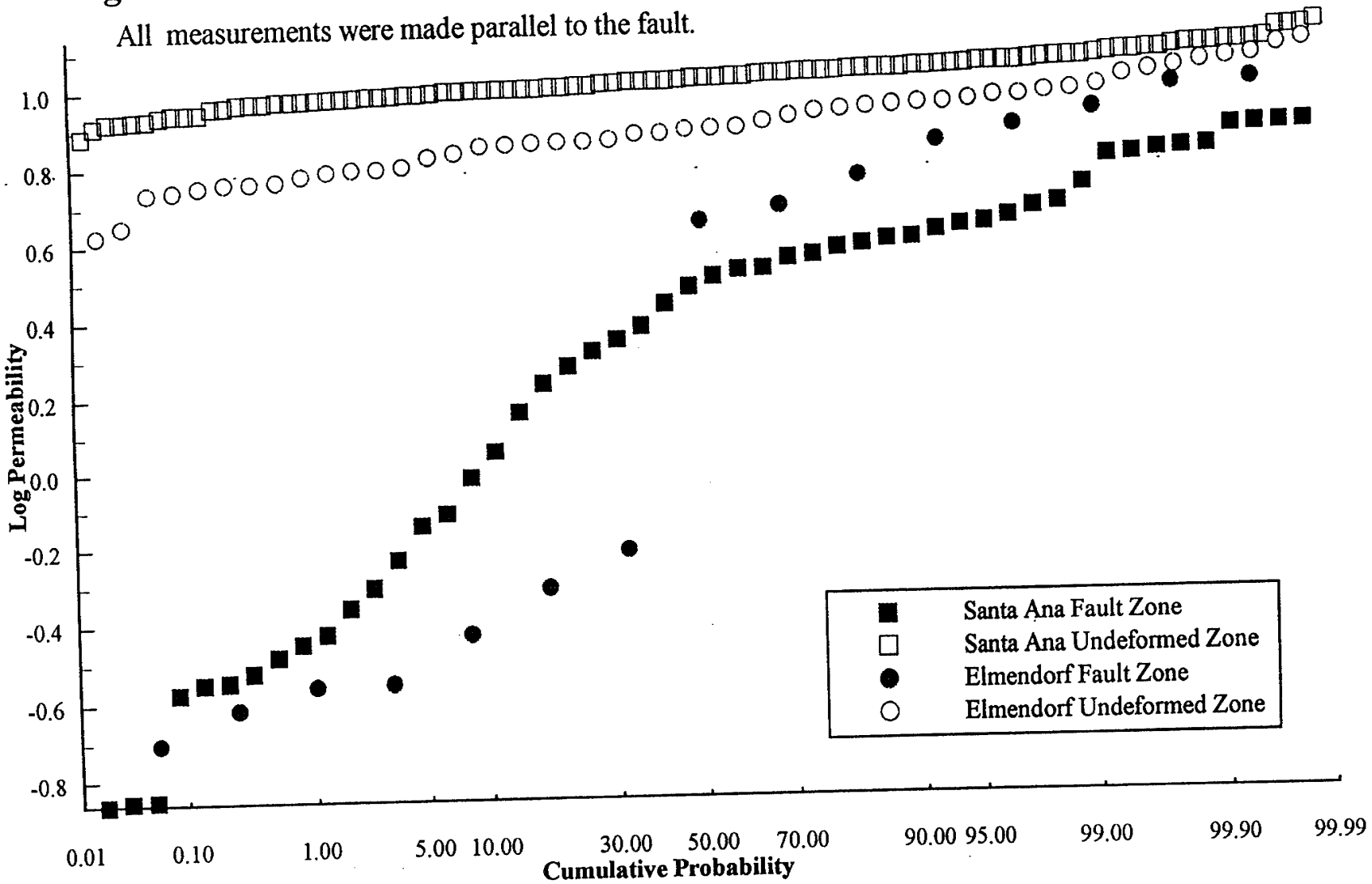

Figure 9: Histogram Plots of Permeability by Zone

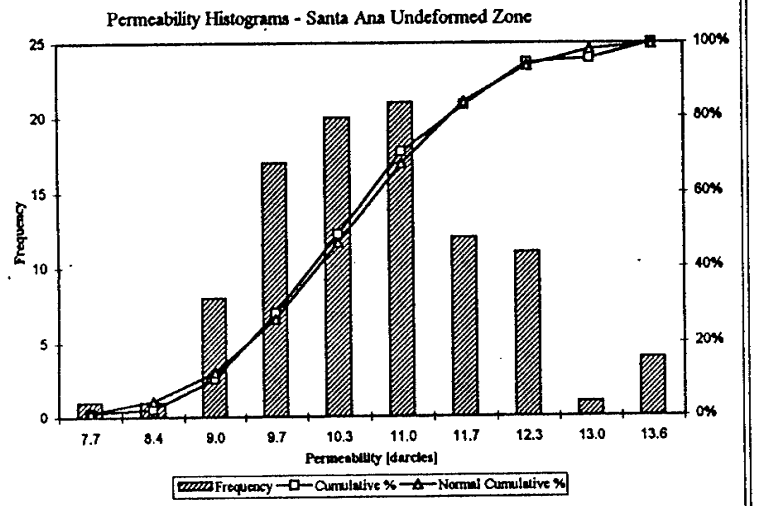

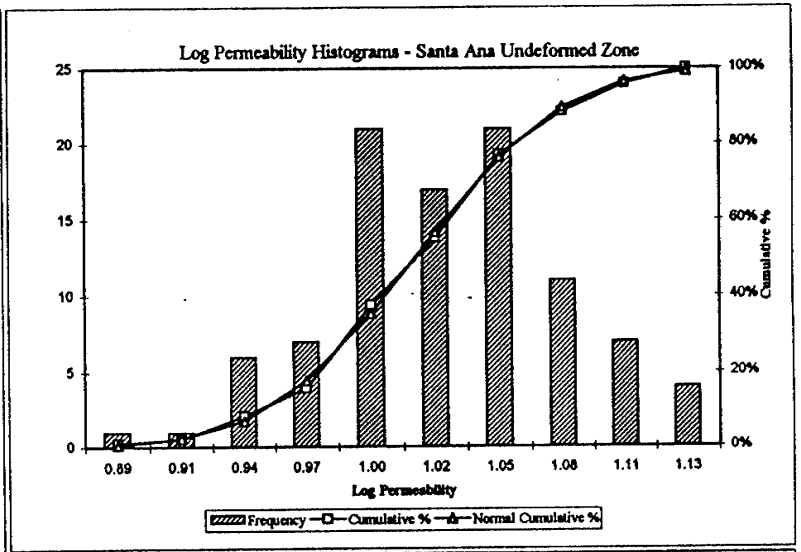

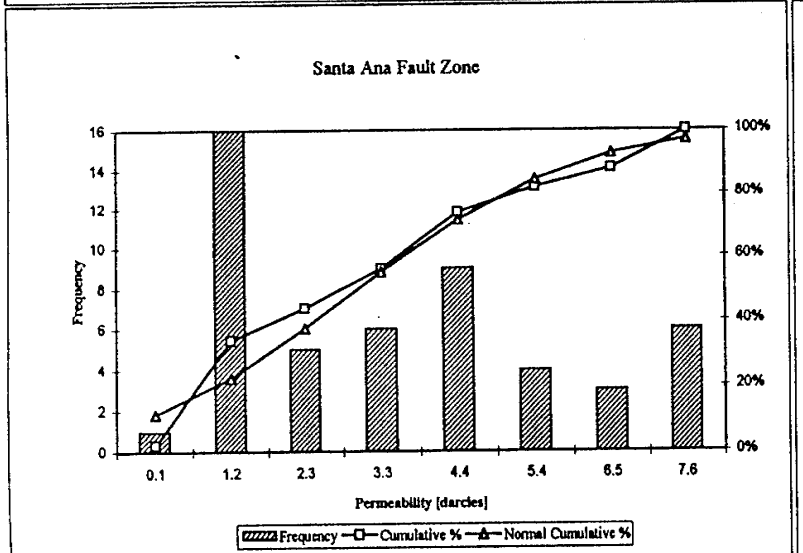

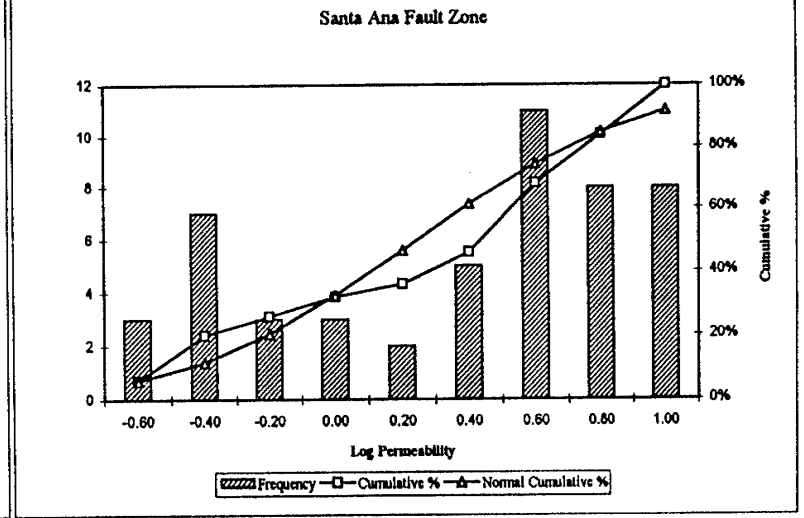

Normal cumulative % shows the cumulative frequency (in %) for a normal distribution with the same mean and variance as the observed permeability data.
All measurements were made parallel to the fault (normal to outcrop).

Figure 9: Histogram Plots of Permeability by Zone continued

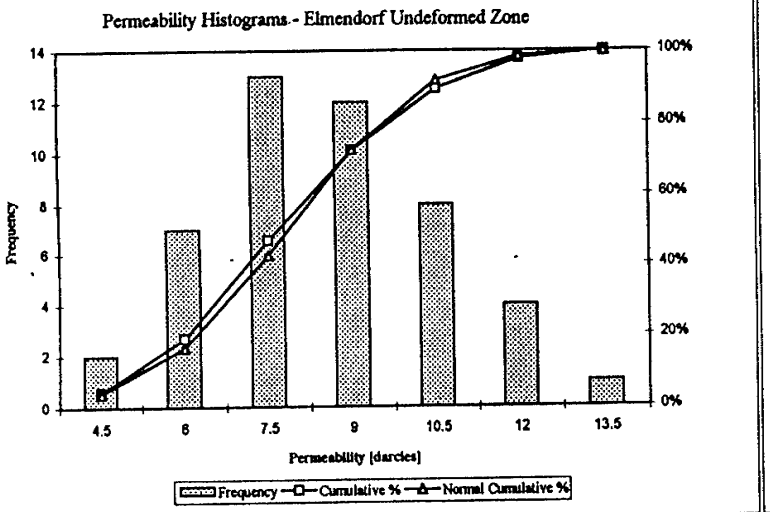

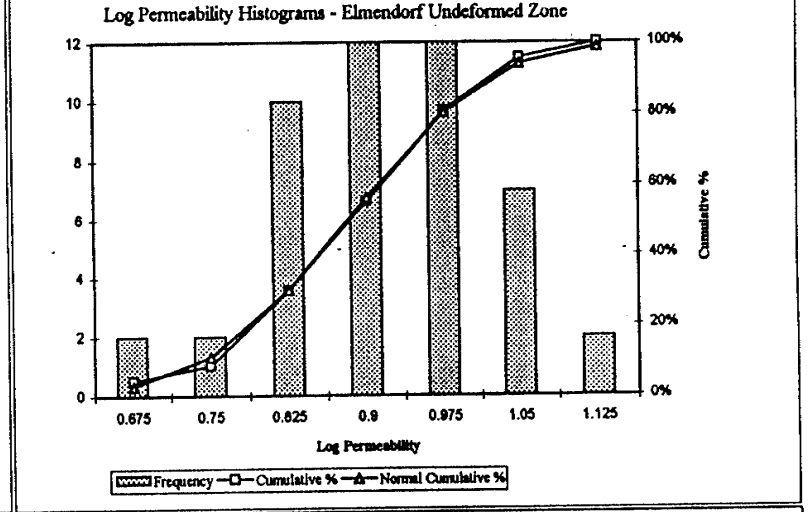

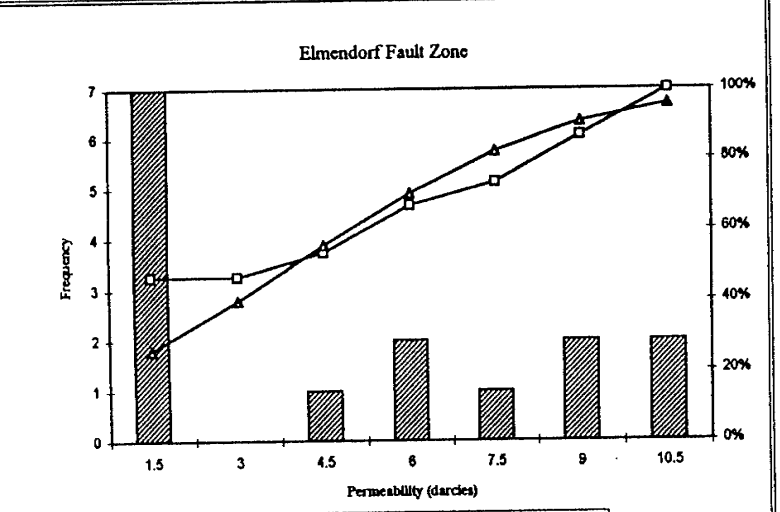

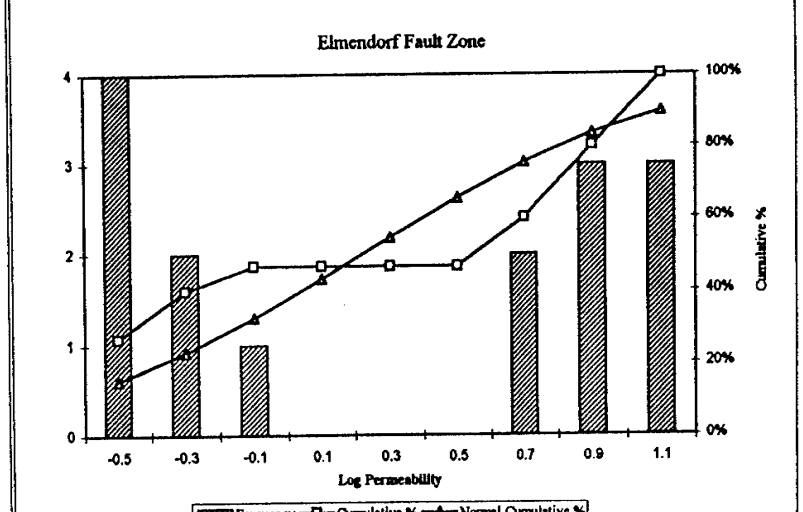

Normal cumulative % shows the cumulative frequency (in %) for a normal distribution with the same mean and variance as the observed permeability data.
All measurements were made parallel to the fault (normal to outcrop).

displacement, has a parallel to fault permeability range of 0.2 to 0.5 darcies whereas the two measurements made on slip band B, which is thinner and less well defined than slip band A, were both on the order of 0.2 darcies (Table 4). Measurements made normal to the plane of slip band A are lower still, falling between 0.04 and 1.0 darcies (Table 4 and Figure 10), although excluding the largest outlier reduces the range to 0.04 - 0.5 and reduces the structure-specific average from 0.4 to 0.2 darcies. This outlier may have been influenced by a small crack near the sampling location. The normal to fault measurements increase the span between undeformed and deformed sand permeability to roughly three orders of magnitude. Permeability measurements fell between 4 and 8 darcies within the zone of deformation bands, which accommodated less vertical displacement than the two slip bands (Table 4 and Figure 10). Deformation bands were too narrow (< 2 mm) to permit measurement of structure-specific permeability.

Table 4: Summary Statistics for Elmendorf Permeability[1] by Fault-Zone Structure

	Average	Variance	CV[2]	Min	Median	Max	n
Slip band (SB) A (darcies)	0.3	0.01	0.31	0.2	0.3	0.5	4
Log_{10} Permeability	-0.48	0.02		-0.62	-0.50	-0.32	
Normal to SB A (darcies)	0.4	0.14	1.01	0.04	0.3	1.0	5
Log_{10} Permeability	-0.63	0.26		-1.36	-0.50	0.004	
Slip band B (darcies)	0.2	0.003	0.23	0.2	0.2	0.3	2
Log_{10} Permeability	-0.63	0.01		-0.71	-0.63	-0.56	
Zone of deformation bands	5.8	4.8	0.37	4.4	4.8	8.4	3
Log_{10} Permeability	0.75	0.02		0.64	0.68	0.92	
Zone A-B (darcies)	6.7	11.5	0.50	0.6	7.3	9.8	6
Log_{10} Permeability	0.71	0.21		-0.22	0.86	0.99	

[1] *All permeability measurements were made parallel to fault unless otherwise stated.*

[2] *CV = Coefficient of Variation ≡ (standard deviation) (mean)*$^{-1}$

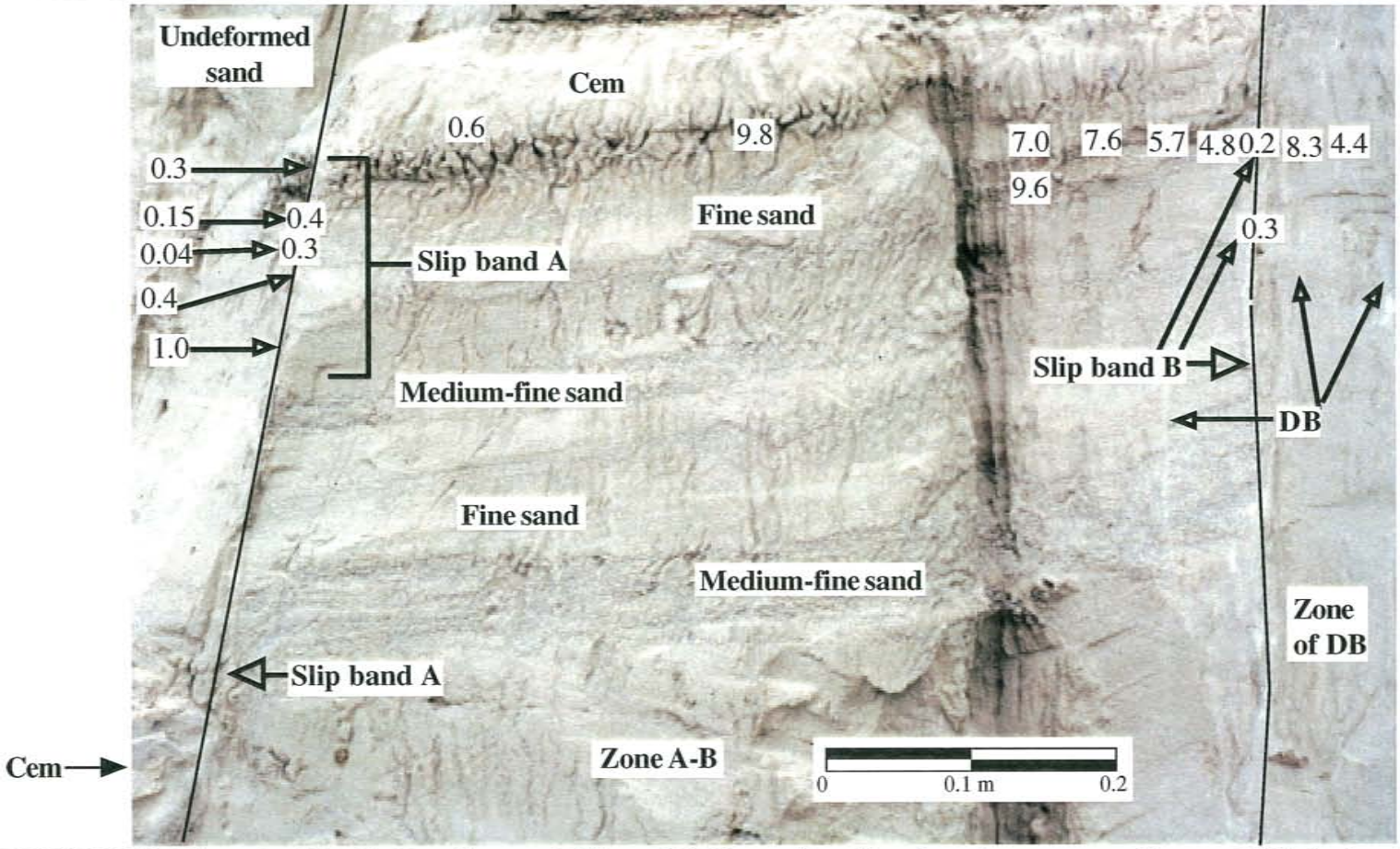

FIGURE 10: Elmendorf Fault-Zone Permeability and Deformation. Numbers show measured permeability in darcies. Slip bands (SB) A and B accommodated 50 - 60 cm of vertical displacement downdropping to the left (south) and show the lowest permeability. All values were measured parallel-to-fault except for those shown pointing at SB A, which were measured normal-to-fault. The undeformed buff sand shown at left is slightly less permeable than zone A-B, in which the original eolian crossbeds, abruptly terminated by SB A and B, are preserved with little deformation. The zone of deformation bands (Zone of DB) contains numerous, sub-vertical, white deformation bands (DB). The cemented bed (Cem) marks vertical displacement.

Zone A-B, the Elmendorf fault-zone structure which experienced the least amount of deformation, showed permeability values close to or larger than the undeformed-zone average of 7.9 darcies. All Zone A-B measurements located within the interbedded medium and fine sands are between 5 and 10 darcies, whereas the measurement collected in the calcite-cemented bed overlaying the interbedded sands was 0.6 darcies (Figure 10).

Although variography results indicate directional anisotropy and a possible periodic or nested spatial correlation structure in undeformed-zone permeability (see Appendix II), spatial heterogeneity does not appear to affect the observed permeability differences between undeformed and deformed zones because the overall variance of undeformed-zone permeability is so small and because the estimated correlation length is short relative to the outcrop area studied (< 1.0 m). The spatial correlation structure observed in the undeformed sand is very likely a function of the eolian cross-bedding (see Appendix II). Fault zone data were too few to permit estimation of semi-variograms.

Parallel to fault permeability varies gradually across the Santa Ana fault zone, in contrast to the sharply localized permeability changes observed in the Elmendorf site. No normal to fault measurements were collected. Permeability is lowest in the cataclasite (ranging from 0.1 to 1.0 darcies), coincident with the greatest induration (Table 5 and Figure 11). The upthrown red and buff 2 zones are less permeable (average permeabilities are 1.2 and 2.0 darcies, respectively) than their downthrown counterparts (red 1 average = 3.2 darcies and buff 1 average = 6.8 darcies), which reflects each zone's individual combination of various parent sediments, permeability differences between the parent materials, and, possibly, varying amounts of deformation. Fault-zone permeability variances are greatest for the two red zones, within which permeability ranges from the outcrop minimum (0.1 darcies) to several darcies.

Table 5: Summary Statistics for Santa Ana Permeability by Fault-Zone Structure

	Average	Variance	CV*	Min	Median	Max	n
Downthrown buff 1	6.8	0.6	0.12	5.3	6.6	7.6	9
Log_{10} Permeability	0.83	0.003		0.72	0.82	0.88	
Downthrown red 1	3.2	1.7	0.41	0.1	3.5	4.8	19
Log_{10} Permeability	0.40	0.17		-0.86	0.54	0.68	
Cataclasite	0.4	0.07	0.63	0.1	0.4	1.0	9
Log_{10} Permeability	-0.45	0.08		-0.86	-0.46	-0.02	
Upthrown red 2	1.2	1.4	0.98	0.3	0.8	3.9	9
Log_{10} Permeability	-0.09	0.15		-0.55	-0.12	0.59	
Upthrown buff 2	2.0	0.05	0.11	1.9		2.2	2
Log_{10} Permeability	0.30	0.002		0.27		0.34	

**CV = Coefficient of Variation ≡ (standard deviation) (mean)$^{-1}$*

Variography results suggest there is no discernible spatial correlation structure for undeformed-zone permeability and a strong spatial trend (i.e., non-stationary behavior) in fault-zone permeability for the scales investigated ($\lesssim$ 3m) at the Santa Ana site (Appendix II). Spatial heterogeneity in permeability thus has a negligible impact on this study's comparison of undeformed and fault zone permeability because undeformed-zone permeability does not depend on location and because it shows little variability. The trend in fault-zone permeability is caused by the relatively abrupt changes in permeability associated with the buff, red, and cataclasite zones.

FIGURE 11: Santa Ana Fault-Zone Permeability and Deformation.
Numbers give measured permeability in darcies. Slip bands (SB) A and B bound the fault zone. The main slip surface (SS) lies in the clay core (CC), which splays (CC Splay)about a pod (Pod) of mixed sand and clay. Downthrown undeformed buff sand (DT Buff) has the highest permeability. The Buff 1 (B1) zone is least indurated and has the highest mean permeability within the fault zone. The more indurated Red 1 (R1) zone has roughly 50% of B1 permeability. The cataclasite (Cat) zone has the lowest mean permeability. Mean permeability is only slightly greater within the Red 2 (R2) zone. The Buff 2 (B2) zone is more permeable than Red 2 and the cataclasite zones, but less permeable than the R1 and B1 zones. No data are available for the upthrown undeformed buff sand (UT Buff).

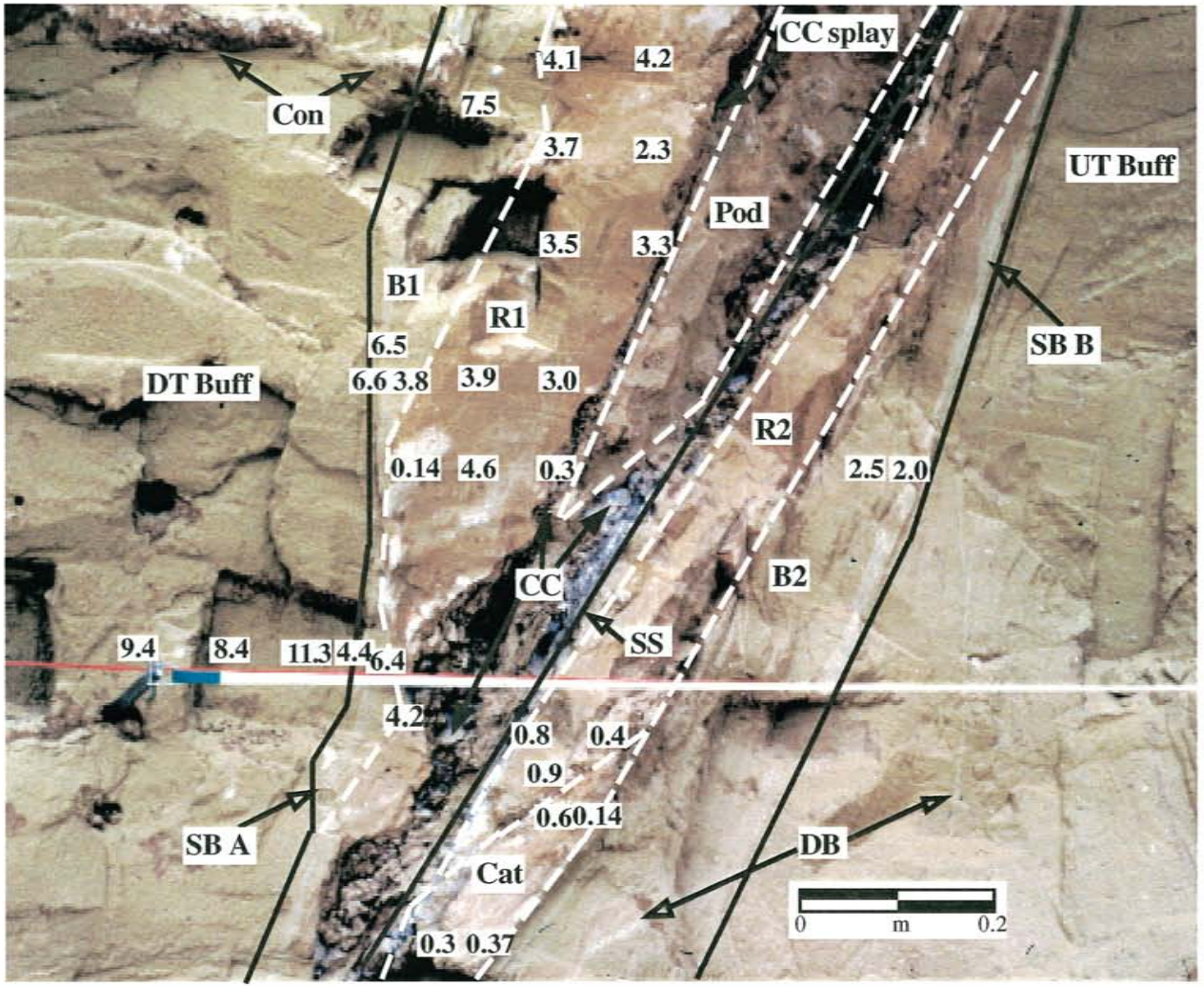

Measurement Error and Calibration

Quantified as the variance contributed by variability of replicates within each sample, measurement error constitutes a relatively minor component of total variance for the undeformed and fault zones (Table 6). Total variance for each zone comprises the variance from spatial heterogeneity (location-specific, considered here as a treatment) and the variance from the sum of measurement error (replicate measurements) components, including operator error, variable moisture content, imprecise relocation, outcrop scraping, tip-seal orientation, and errors in determining absolute atmospheric pressure and air viscosity. Measurement error had the largest impact within the Santa Ana undeformed zone, where it accounted for 34% of the total variance, and is likely a function of the outcrop's greater friability - resulting in frequent re-scraping, and more frequent resampling due to compaction. Measurement errors for the Elmendorf undeformed zone accounted for 14% of total variance and fault zone errors accounted for only 1% of their respective total variances. Observed F statistics are all significant at the 95% confidence level, indicating location-specific variance does not account for the entire total variance.

Table 6: Replicate Measurement Variance versus Total Variance

Zone	Within-Sample Variance as % Total Variance	F statistic (Observed)	F Critical Value[1]
Elmendorf Undeformed	14	28.5	1.45
Elmendorf Fault Zone	1	793.1	2.11
Santa Ana Undeformed	34	9.5	1.37
Santa Ana Fault Zone	1	522.0	1.57

[1] *F critical given for two-tailed, 95% confidence level.*

Analysis of variance in which resampling is considered as a treatment showed that resampling added additional variance to the 29 sampling locations which had been remeasured at least once. For example, replicate permeability data from an Elmendorf sampling location which was measured on

three separate sampling dates was used to construct an ANOVA table within which the different sampling dates were considered as a treatment. Computed F statistics exceeded critical two-tail F values at a 95% confidence level for 7 of the 15 resampled Santa Ana locations and 6 of the 14 resampled Elmendorf locations, indicating additional sampling error was introduced by sampling at several different times. The error variance, which is attributed to removal of several millimeters of outcrop before each sampling incident, errors in relocating the sampling location, changes in moisture content or air viscosity or atmospheric pressure, and differing application pressures and orientations, is still small in comparison to the variance contributed by spatial heterogeneity.

Agreement between field SAMP permeability calibration measurements and the laboratory-based measurements obtained by Davis (1994) using a continuous flow mini-permeameter (CFMP) is quite good for manufactured sandstone standards 2A and 21 and poor for standards 11 and 15 (Figure 12). SAMP calibration measurements are relatively consistent for all the manufactured sandstone standards during the three month long field campaign. Given the good agreement observed for standards 2A and 21, possible causes for the disparity between CFMP and SAMP measurements for standards 11 and 15 include changes to the standards (e.g., damage during transport to and from the field), instrument bias in the 15 darcy range, or errors in the original CFMP calibration measurements. A log-log plot of SAMP theoretical permeability versus time, based on the relationship reported by Davis et al. (1994) with parameter values appropriate for this study, reveals a linear relation for times greater than two seconds, thus the instrument should be equally sensitive across the 1 - 40 darcies range (Figure 13). Therefore, the SAMP instrument is theoretically not biased within the 10 - 20 darcy range. SAMP and field CFMP measurements showed good agreement (1.5 versus 1.9 darcies) at the sole sampling location where both instruments were utilized, further corroborating the SAMP's sensitivity within the 1 - 10 darcies range. Results from an F-test of the sample variances and a Student's t-test of the sample means

Figure 12: Measurement Variability of Calibration Standards

a. Santa Ana Site

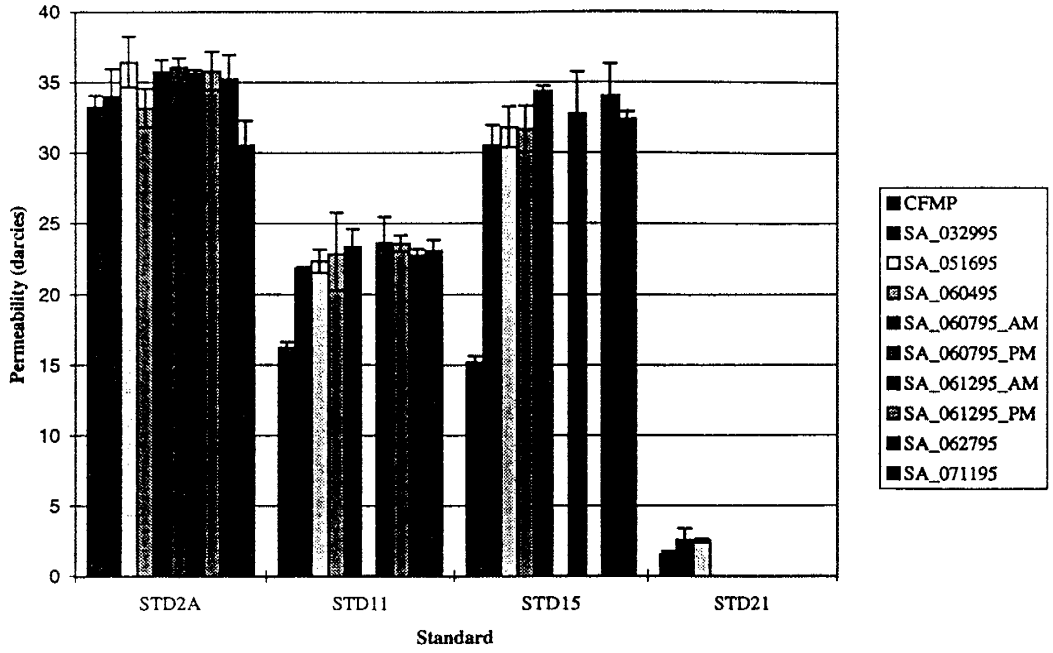

b. Elmendorf Site

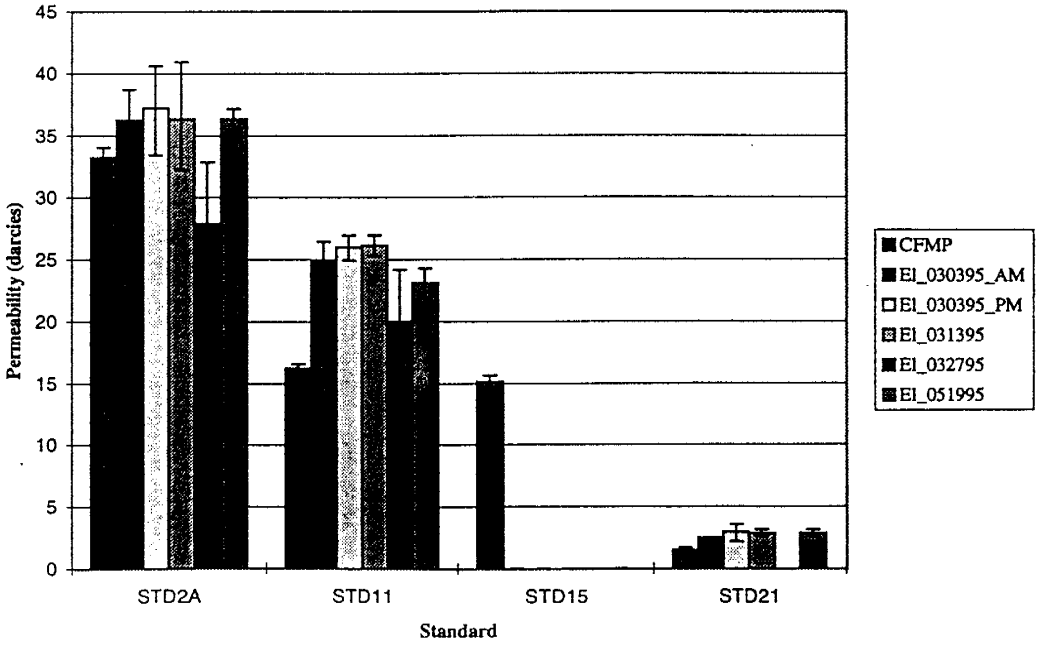

Error bars show the average plus or minus 1 standard deviation.

Figure 13: Theoretical Syringe Air Mini-Permeameter Time Sensitivity

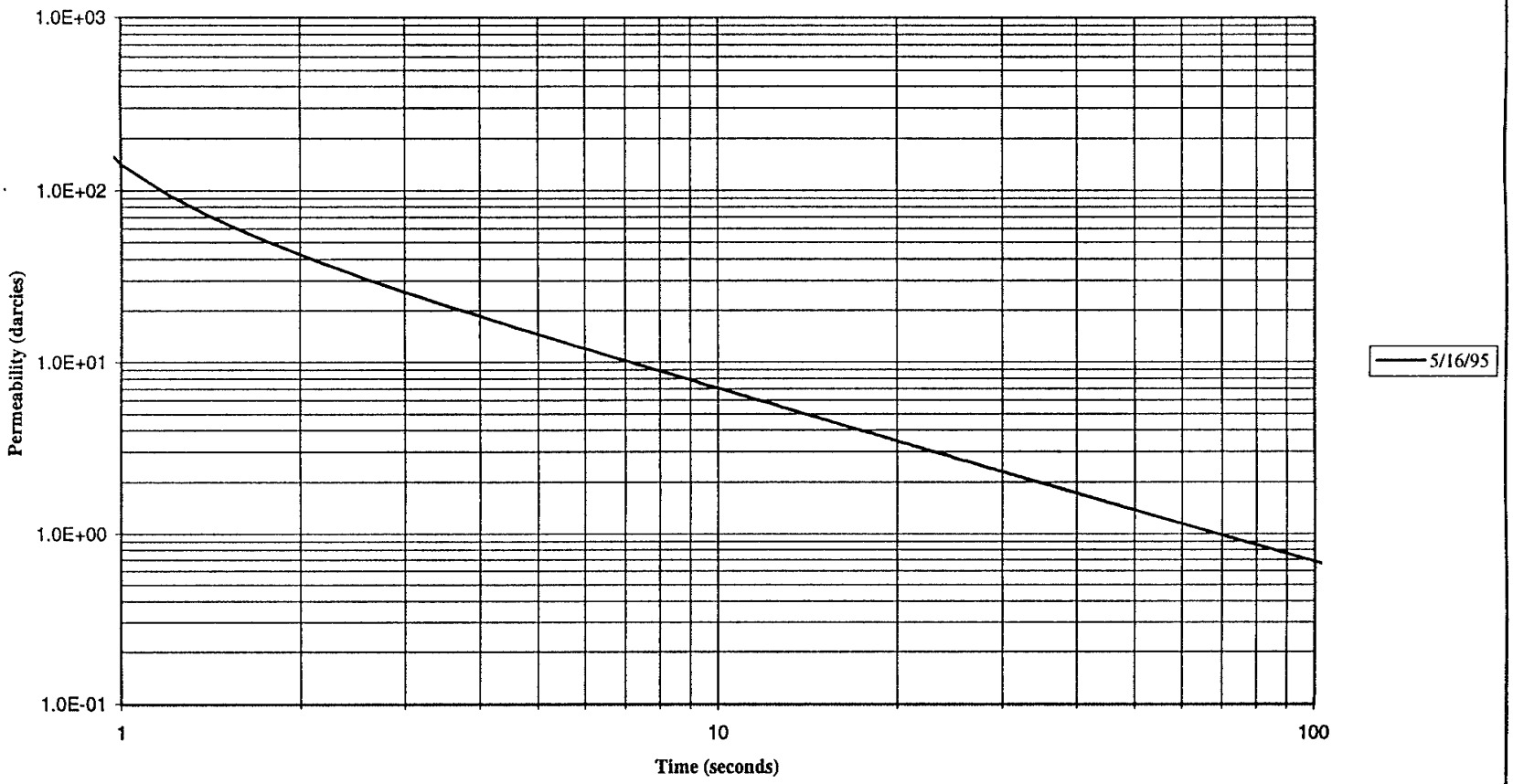

Graph of the relation between syringe travel time and permeability according to Davis et al. (1994) using parameter values appropriate for the Santa Ana site.

did not reject the hypothesis that the sample statistics are the same for the SAMP and field CFMP instruments at a 95% significance level. This all suggests either (or both) lab-based CFMP measurement error or damage to standards 11 and 15 is more likely responsible for the disparity between CFMP and SAMP permeability estimates.

As shown by the ± one standard deviation error bars in Figure 12, the variability about field SAMP calibration measurements is relatively small. Calibration measurements made at the Elmendorf site are slightly more variable than those made at the Santa Ana site. Calibration measurement standard deviations did not exceed five darcies on all but one sampling date for the high permeability standards 2A, 11, and 15. Standard deviations for the low permeability standard 21 were typically much less than a darcy except for one sampling date when it reached one darcy.

Petrography

Composition, Fabric, and Texture

According to Folk's (1968) classification system, all study site sands are lithic arkoses, indicating a relative abundance ordering (most to least) of feldspars, rock (lithic) fragments, and quartz detrital grains, respectively (Figure 14). Plagioclase is the most common feldspar, typically at least twice as abundant as potassium feldspar. Volcanic rock fragments constitute the largest percentage of recognizable rock fragments, with much smaller percentages of sedimentary lithic fragments and rare to absent metamorphic lithic fragments. Chert is persistent in trace amounts across sites and across deformed and undeformed zones. Scanning electron microscopy revealed authigenic smectite on some grains from the Elmendorf undeformed zone. Cements are absent in all samples except those from the Santa Ana cataclasite and red 2 zones where calcite cement is rare.

Undeformed zone sands appear fairly similar for the two sites. Both are well sorted and mature to supermature with sub-rounded grains and relatively small (≤ 20%) amounts of monocrystalline

detrital quartz (Table 7 and Table 8). Volcanic lithic fragments are more abundant in the Elmendorf undeformed sands than the Santa Ana undeformed sands, which agrees with Lozinsky's (1994) observation that lower Santa Fe Group sediments are richer in volcaniclastics than their upper Santa Fe Group counterparts. Santa Ana undeformed sands are richer in feldspars than Elmendorf sands. No cements were observed, although trace amounts of undifferentiated calcite (either remnant grains or cements) were found. The two undeformed zones have similar fabrics; specifically, undeformed sands are grain supported, as opposed to matrix supported, and have tangential grain contacts. Elongate grain orientation is mostly sub-horizontal, following the Elmendorf site's tangential bedding, whereas Santa Ana sands do not exhibit any evidence of bedding (compare Figure 15 and Figure 20a). Clay-size fraction forms a minor portion (< 6%) of undeformed sands from both sites.

Table 7: Mineral Abundance - Elmendorf Site

Constituent	Undeformed Zone[1]	Slip Band A	Δ	Δ without Porosity
Detrital Quartz	14.0	15.2	1.2	-0.6
Potassium Feldspar	7.7	4.2	-3.5	-5.3
Plagioclase Feldspar	20.2	18.7	-1.5	-4.6
Total Rock Fragments	26.7	21.5	-5.2	-10.0
Volcanic RF	10.0	5.0	-5.0	-7.4
Metamorphic RF	0.0	0.2	0.2	0.2
Sedimentary RF	3.8	3.0	-0.8	-1.5
Undifferentiated RF	12.8	13.3	0.5	-1.2
Clay-Size Fraction	5.7	23.2	17.5	20.3
Folk 1968 Classification	*(See Figure 14 for ternary plot)*			
Quartz Pole	20.5	25.5		
Feldspar Pole	40.8	38.9		
Rock Fragment Pole	38.7	35.6		

[1] *Undeformed and Slip Band columns show percent abundance (% of total rock volume), Δ shows change in percent abundance between undeformed and deformed zones, and Δ Without Porosity gives the same change calculated without including macroporosity and microporosity.*

Figure 14: Folk (1968) Classification of Study Site Sands

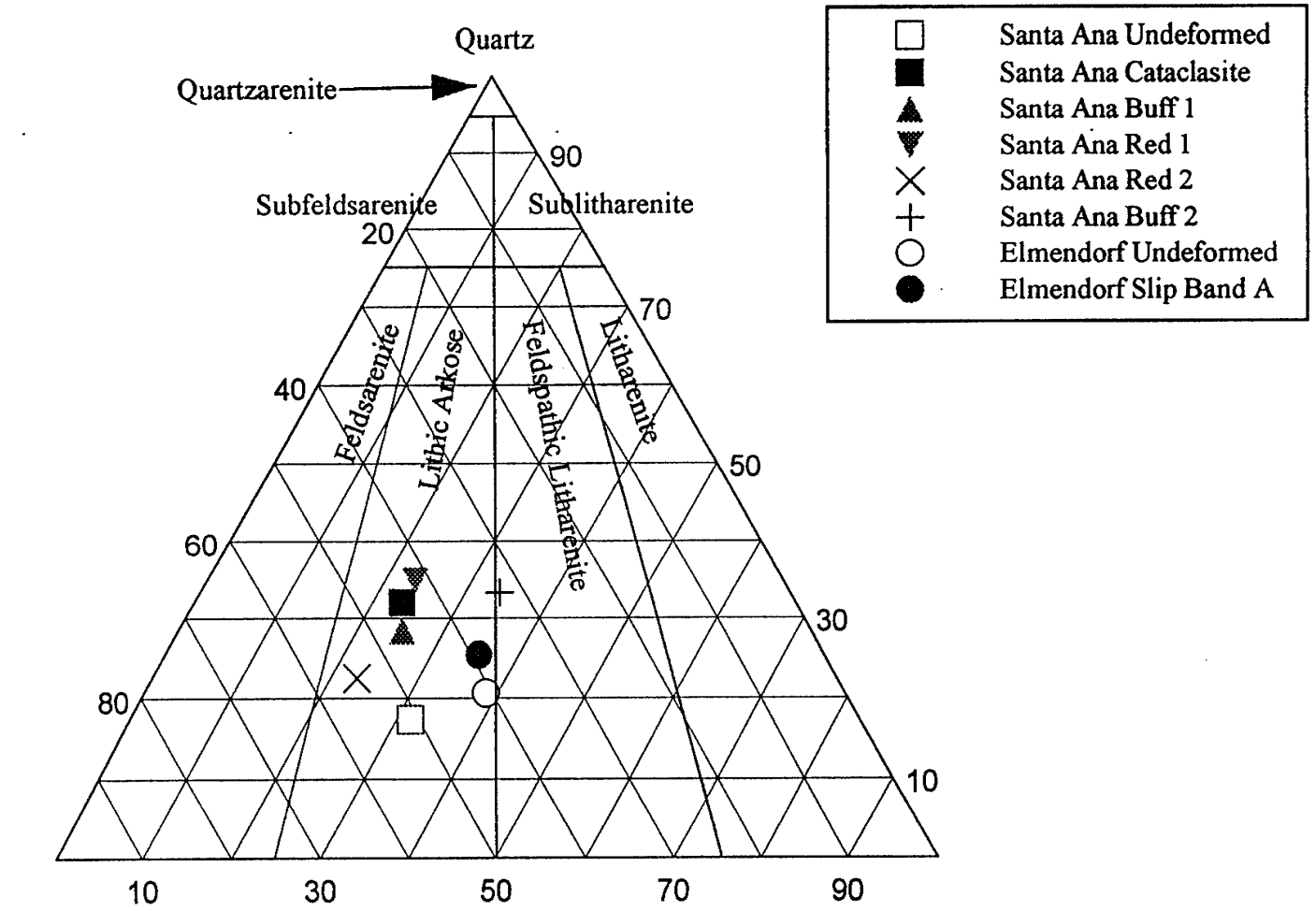

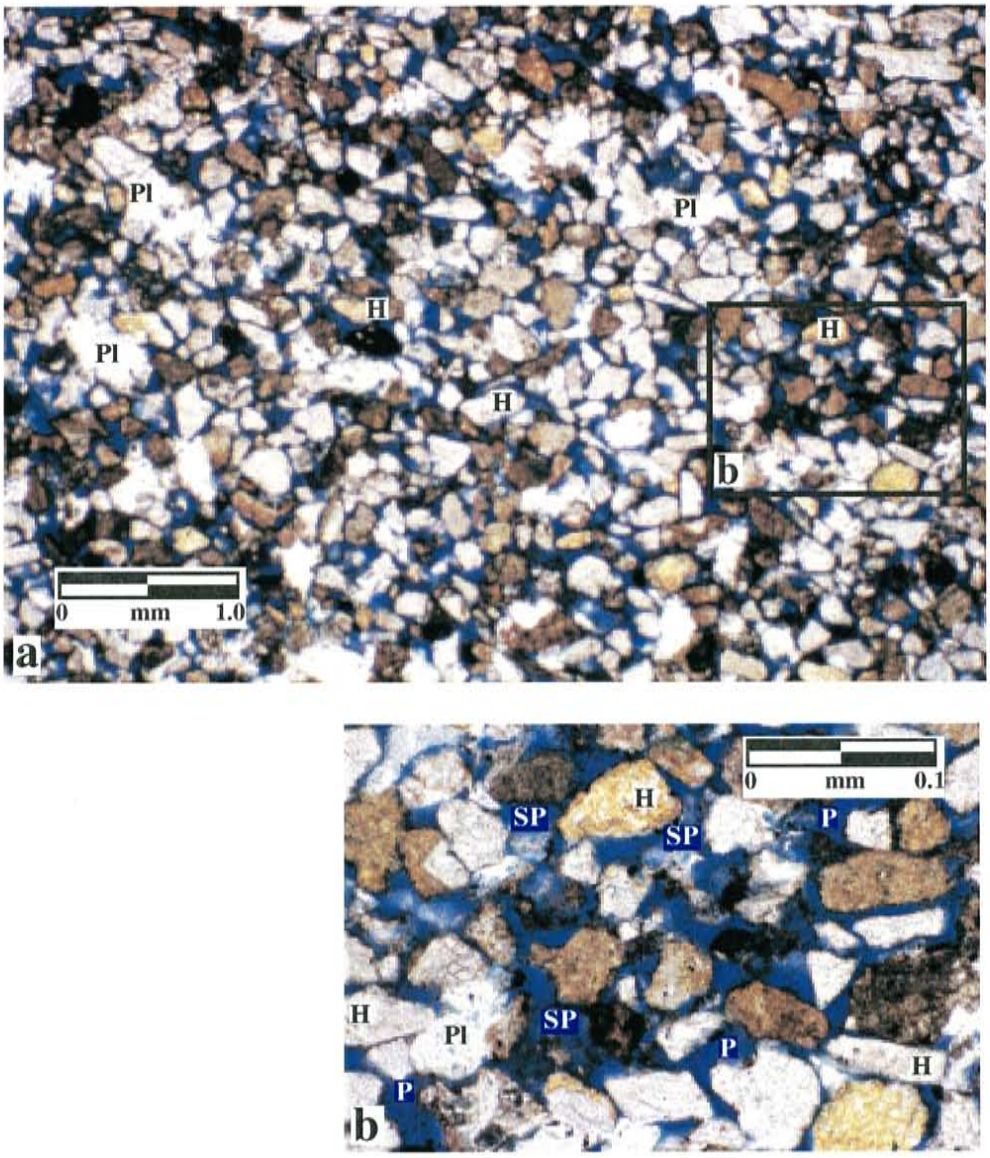

FIGURE 15: Thin-Section Photomicrographs of Elmendorf Undeformed Sand.
a) 20X magnification displays relatively large pores (P) filled with blue-dyed epoxy, sub-horizontal orientation of most elongate grains (H), and tangential grain contacts. Plucked grains (Pl) leave large white areas.

b) Close-up (200X) of undeformed sand grains, showing detail of blue pore space (P), sub-horizontally oriented elongate grains (H), and tangential grain contacts. Note relative absence of clay-sized material dispersed in the pores. Secondary porosity (SP) is created by dissolution or corrosion of grains.

Composition and fabric are substantially different for deformed sand within slip band A at the Elmendorf site. Clay-size fraction increases by four-fold, balanced in part by decreases in volcanic lithic fragments and potassium feldspars (Table 7 and Figure 16). Average pore and grain sizes (and sorting) decrease substantially relative to undeformed sand and the fabric changes from grain-supported to matrix-supported because most grains are surrounded by clay-sized material (Figure 17). Elongate grains formerly aligned with the tangential bedding are reoriented sub-parallel to dip (Figure 17).

The mineral abundance data support the hypothesis that slip band A at the Elmendorf site is the product of cataclasis, i.e., it is composed of cataclasite. After recalculating the change in mineral abundance between undeformed and deformed sand by excluding porosity, both potassium feldspar and plagioclase show a large decrease (slip band A abundance - undeformed sand abundance = ~5%) exceeded only by the decrease in volcaniclastics (~7%). These relatively large reductions, when compared to the negligible change in detrital quartz (<1%), suggest that cataclasis increases clay-size fraction through preferential fracturing of weaker feldspar and volcaniclastic grains instead of the more resistant quartz grains, assuming mass is conserved.

Figure 16: Elmendorf Mineral Abundance & Permeability

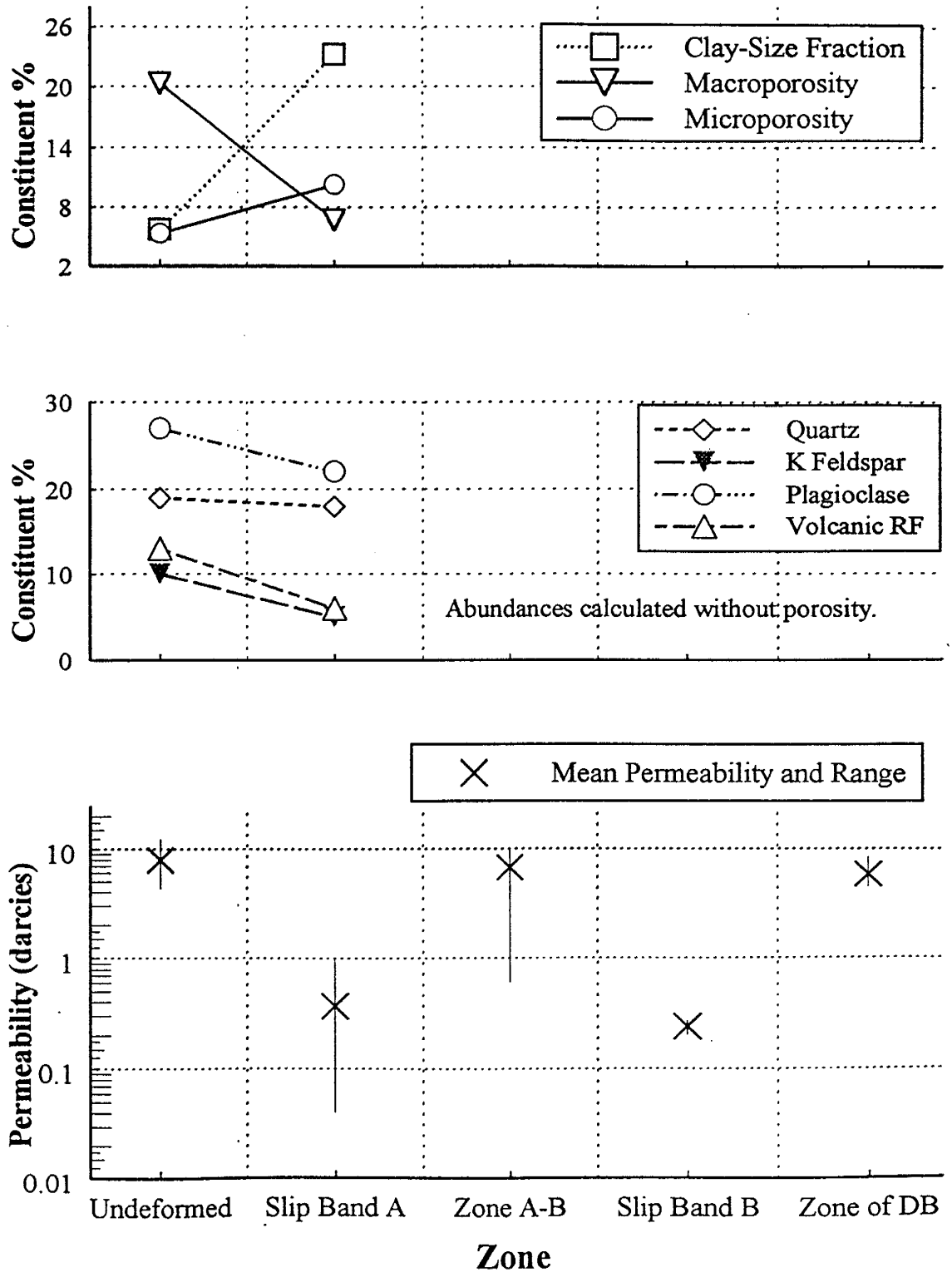

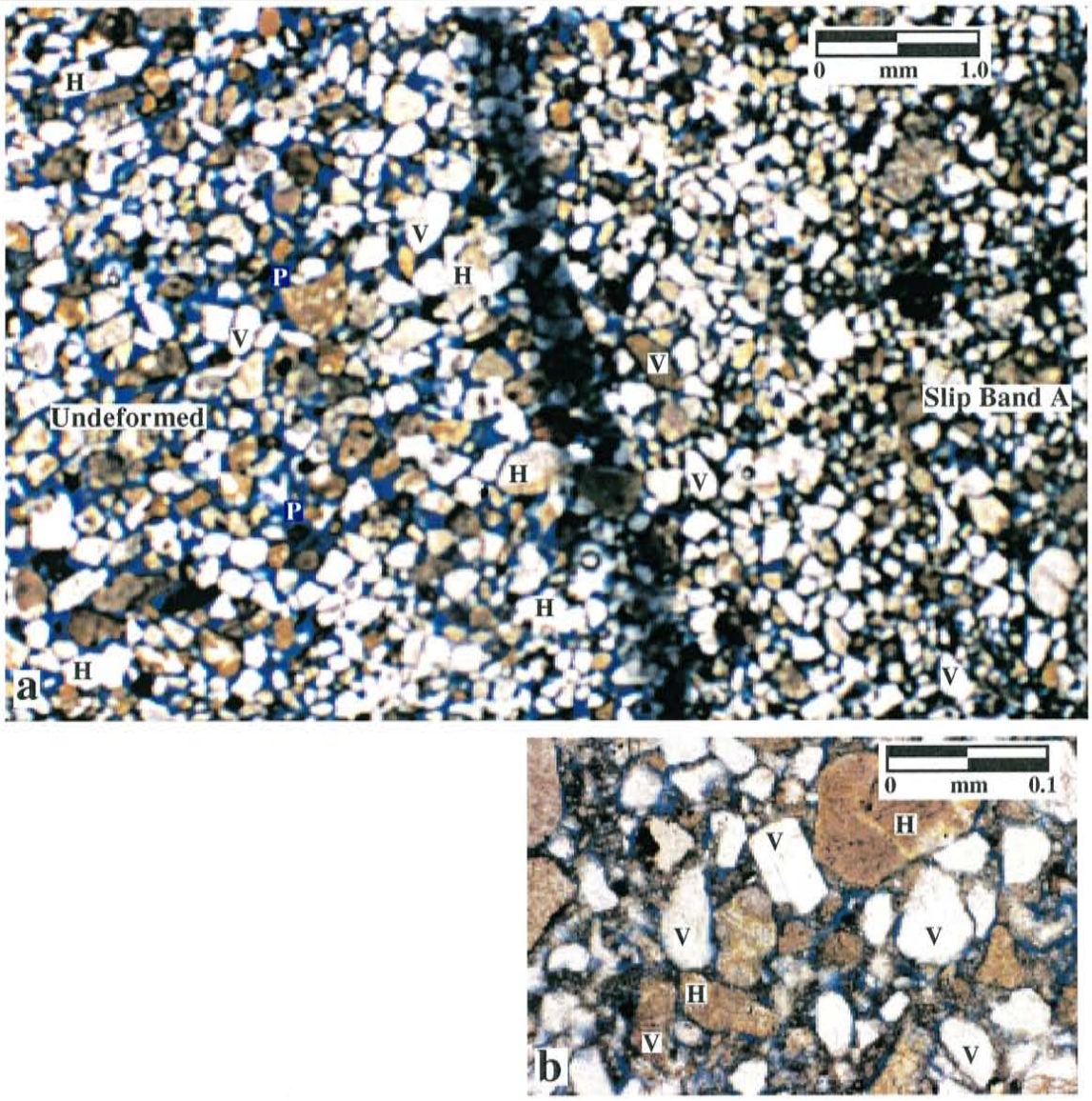

FIGURE 17: Thin-Section Photomicrographs of Elmendorf Fault Zone.

a. Contact between undeformed buff sand (Undeformed) on left and slip band A on right. Blue color shows epoxy-impregnated pore space (P). The dark band (drawn with marker pen) defines the transition from undeformed sand, with large pores and primarily sub-horizontally oriented elongate grains (H) to deformation structure, with reduced porosity and a large increase in clay-sized materials. Many elongate grains are reoriented parallel to dip (V) within slip band A. Grain and pore sizes appear significantly smaller in the deformed zone.

b. Close-up of deformed buff sand in slip band A. Pores are narrower than in the undeformed sand but appear to remain interconnected. Most of the pores are partially occluded with red or red-brown clay-sized material. Grain size appears to be more variable than pore size.

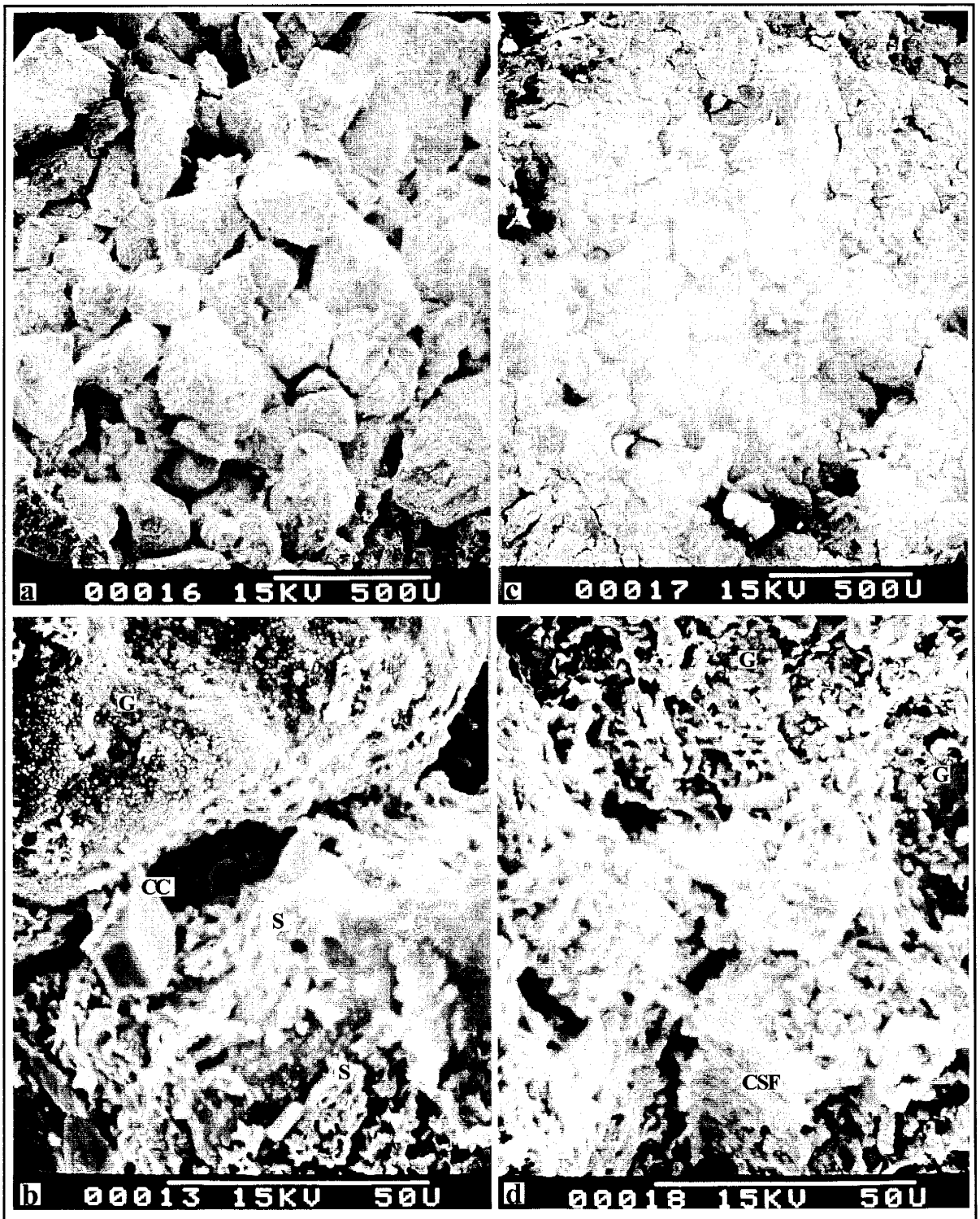

FIGURE 18: SEM Photomicrographs of Elmendorf Sands. a) Undeformed-zone sand shows large, open pores and few grain coatings. **b)** Close-up of undeformed sand grains (G) with clinoptilolite crystal (CC) and smectite (S). **c)** Slip band A reveals increased clay-size fraction (CSF) coats grains and occludes pores. Grain and pore sizes appear smaller than in a). **d)** Close-up of slip band A shows grains (G) are well-coated with CSF. Plucked grain reveals pore body filled with CSF at bottom center. ($U = 10^{-6}$ m)

Mineral composition and clay size fraction vary widely within the Santa Ana fault zone, yet lack of constraint on the number and type of different parent sediments confounds determination of the degree to which the variation was caused by cataclasis, diagenesis, bed drag, or mixing. Clay-size fraction is greatest in the cataclasite (27%) and red 2 zones (22%), roughly three times greater than that observed in the red 1 and buff 2 zones and nearly five times greater than the buff 1 zone clay-size fraction (Table 8 and Figure 19). Some or all of the clay-size fraction may be attributable to bed drag and mixing of clay-rich beds within the fault zone; cataclasis and diagenesis of weaker minerals may have contributed also. Potassium feldspar abundance is consistent across the fault zone (9 to 12%), except in the cataclasite, where it is less common (7%); plagioclase is also fairly consistent across the fault zone (18-22%), barring the buff 2 zone (11%) (Table 8). Quartz abundance varies widely (13 to 24%) and volcaniclastics are rare to absent (0 - 2%) (Table 8).

Table 8: Mineral Abundance - Santa Ana Site

Constituent	Downthrown Undeformed[1]	Buff 1	Red 1	Cataclasite	Red 2	Buff 2
Detrital Quartz	11.5	20.0	23.7	18.0	13.3	20.7
Potassium Feldspar	8.8	12.0	10.3	6.8	10.0	9.0
Plagioclase Feldspar	24.7	19.7	17.7	18.0	22.0	11.3
Total Rock Fragments	21.0	17.7	16.3	12.8	13.7	21.0
Volcanic RF	4.8	0.7	0.0	2.0	1.3	1.0
Metamorphic RF	0.2	0.0	0.3	0.0	0.0	0.0
Sedimentary RF	1.5	2.0	2.0	2.8	1.0	3.0
Undifferentiated RF	14.5	15.0	14.0	8.0	11.3	17.0
Clay-Size Fraction	4.7	5.7	8.3	26.8	22.3	9.0
Folk 1968 Classification						
Quartz Pole	17.3	28.4	34.8	32.0	22.5	33.3
Feldspar Pole	51.0	46.4	41.7	44.6	54.5	32.8
Rock Fragment Pole	31.7	25.1	23.5	23.4	23.0	33.9

[1] *All but Folk poles (see Figure 14) are percent abundance (% of total rock volume).*

The geometry and contiguity of the fault zone's clay core, cataclasite, and pairs of sub-vertical zones imply that adjacent zones are more likely to be similarly composed than those which are not contiguous. For example, the buff 1 zone is more likely to resemble the red 1 zone and downthrown undeformed buff sand in mineral composition than the buff 2 zone. Furthermore, whereas the two red zones could be expected to closely resemble one another given their contiguity, the slip surface and clay core which separate them may have actually prevented sharing of sediments between the two zones. The petrographic results show the two red zones and the two buff zones differ substantially in composition (Table 8), as expected from fault zone geometry and contiguity.

Sedimentary texture varies significantly between the Santa Ana fault zone and the downthrown undeformed sand. Grain fabric changes from fully grain supported in the undeformed sand with primarily tangential grain contacts to locally matrix or grain supported within the cataclasite and two red zones. Average grain size is smallest within the cataclasite zone and largest within the two buff zones and the downthrown undeformed buff sand (Figure 20). The cataclasite and red zones are poorly sorted, whereas the two buff zones and the downthrown undeformed sand are well sorted. Although there is no preferred orientation for elongate grains in the downthrown undeformed sand, many grains are oriented sub-parallel to dip within the fault zone (Figure 20).

X-ray diffraction of the clay-size fraction separated from six Santa Ana site samples revealed clay minerals are present in both undeformed and deformed sands (Table 9). All major clay mineral families except chlorite were observed. The semi-quantitative measurements do not reveal a discernible trend in clay-mineral composition as a function of either fault zone geometry or extent of deformation. Nor do the data indicate clay minerals observed in the deformed and undeformed sands are significantly different from those found in the clay bed exposed in the downthrown block. Quartz, feldspars, calcite, and clinoptilolite, a zeolite, were also identified as clay-size fraction components.

Crystals of the latter are visible in SEM photomicrographs from the Elmendorf undeformed sand (Figure 18).

Table 9: Mineralogy of Santa Ana Clay-Size Fraction

Sample Location	Kaolinite[1]	Illite	Smectite	I/S[2]	Others[3]
Undeformed buff sand - downthrown block	2	3	1	4	Qtz, Fel
Deformed buff zone 1	2	4	2	2	(Qtz), (Cal), (Fel), (Clino)
Deformed red zone 1	4	1	2	3	**Cal**, Qtz, Fel
Cataclasite	2	2	2	4	Qtz, Cal, Fel, Clino
Clay core	2	2	3	3	Qtz
Clay bed	3	3	2	2	Qtz, Cal, Fel

[1] *Clay minerals reported as parts in ten.*

[2] *I/S = Mixed-layer illite and smectite clays*

[3] *Non-clay minerals: Qtz = quartz; Fel = feldspars; Cal = calcite; Clino = clinoptilolite.* **Bold** *face indicates major component and parentheses indicate minor component.*

Figure 19: Santa Ana Mineral Abundance & Permeability

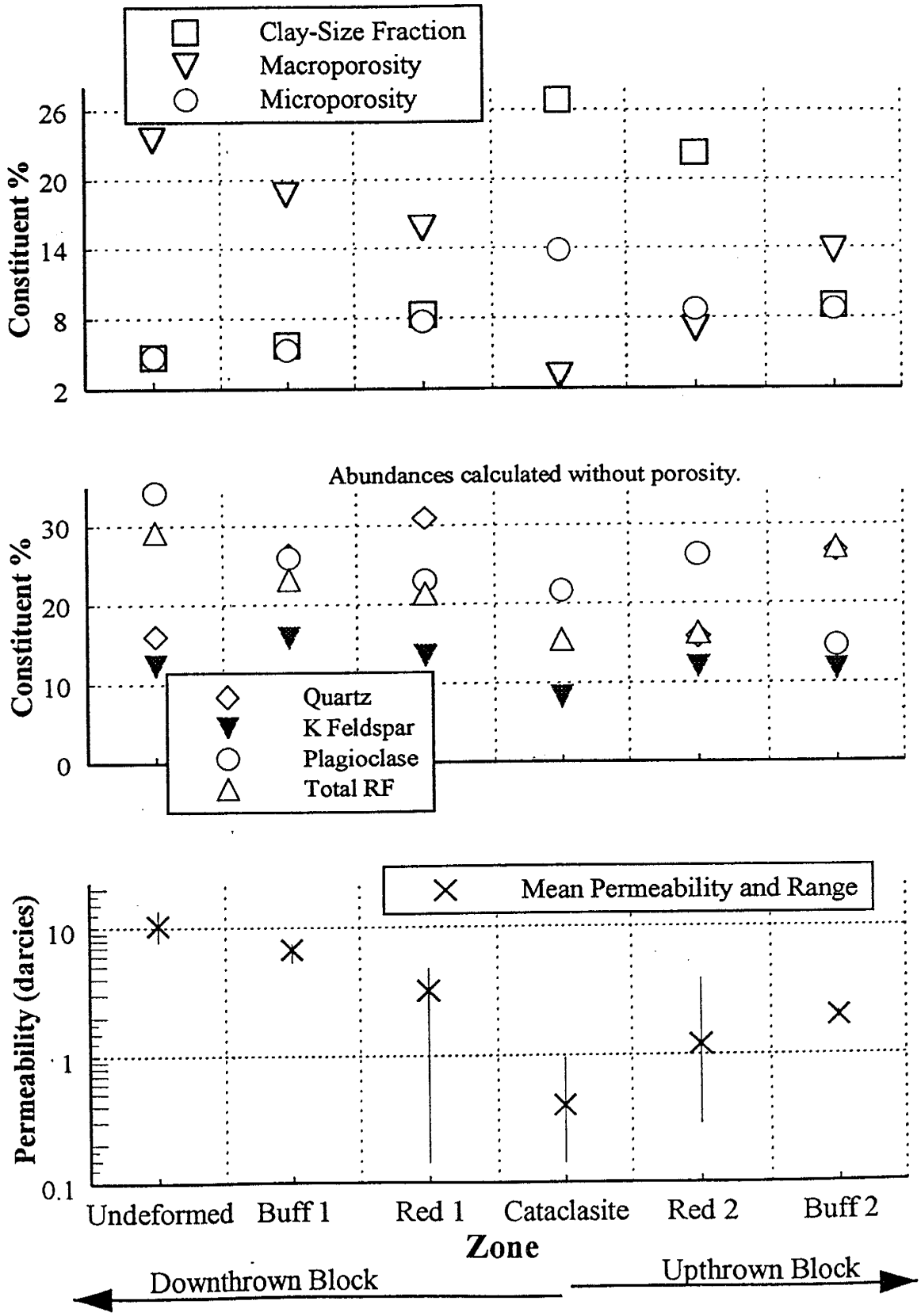

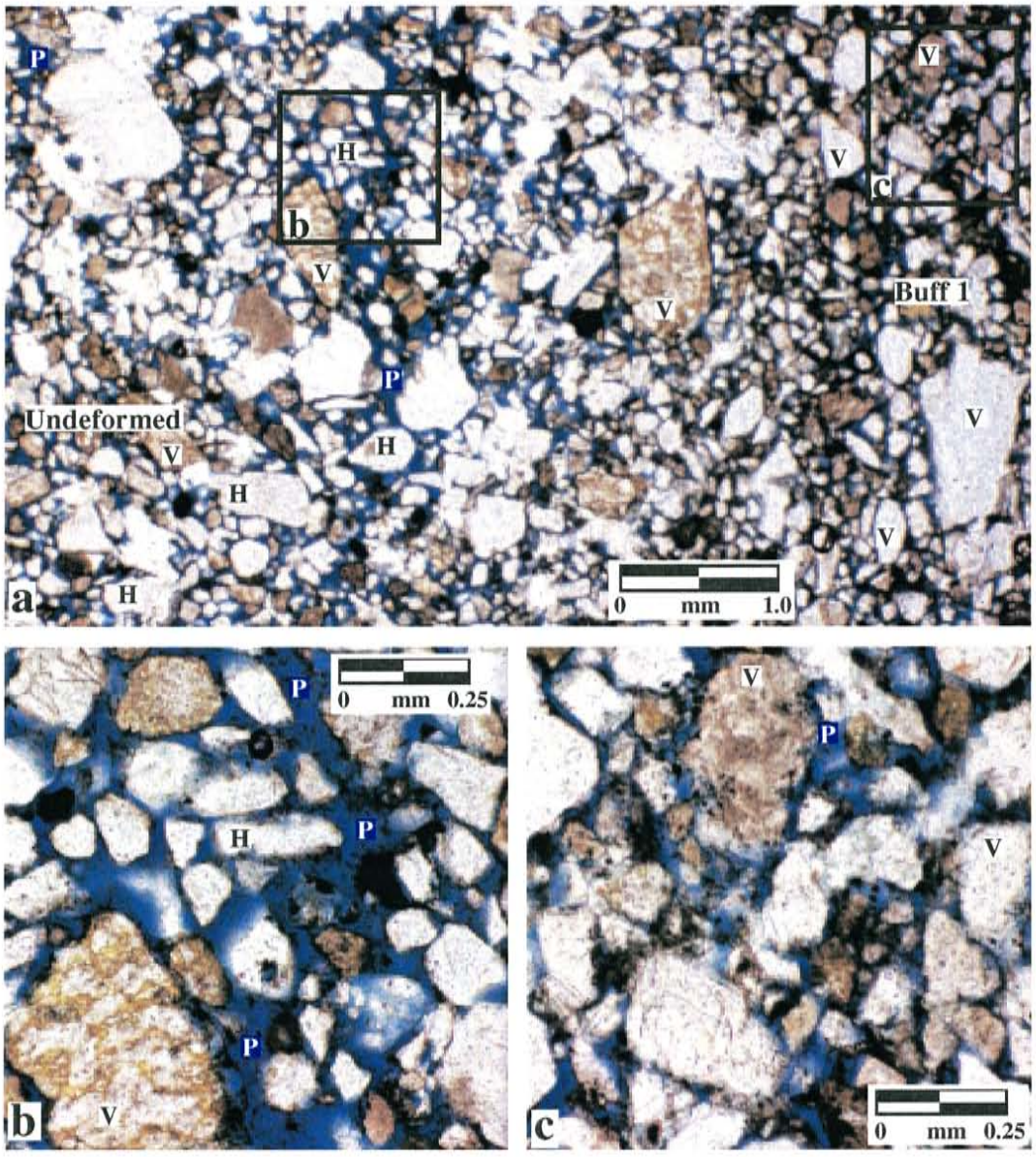

FIGURE 20: Photomicrographs of Santa Ana Undeformed and Deformed Sands.

a) Contact between undeformed buff sand (Undeformed) on left and least deformed zone (Buff 1) on right. Blue color shows epoxy-impregnated pore space (P). Note the gradational contact between undeformed and deformed zones in center. Elongate grains have both horizontal (H) and vertical (V) orientations in the undeformed zone while most are oriented subvertically (V) within the deformed zone. Grain and pore sizes appear slightly smaller in the deformed zone.

b) Close-up of undeformed buff sand. Pores appear relatively large with little brown or red-brown clay-sized material dispersed within the pores.

c) Close-up of deformed Buff 1 zone. Pores are smaller and contain more clay-sized material.

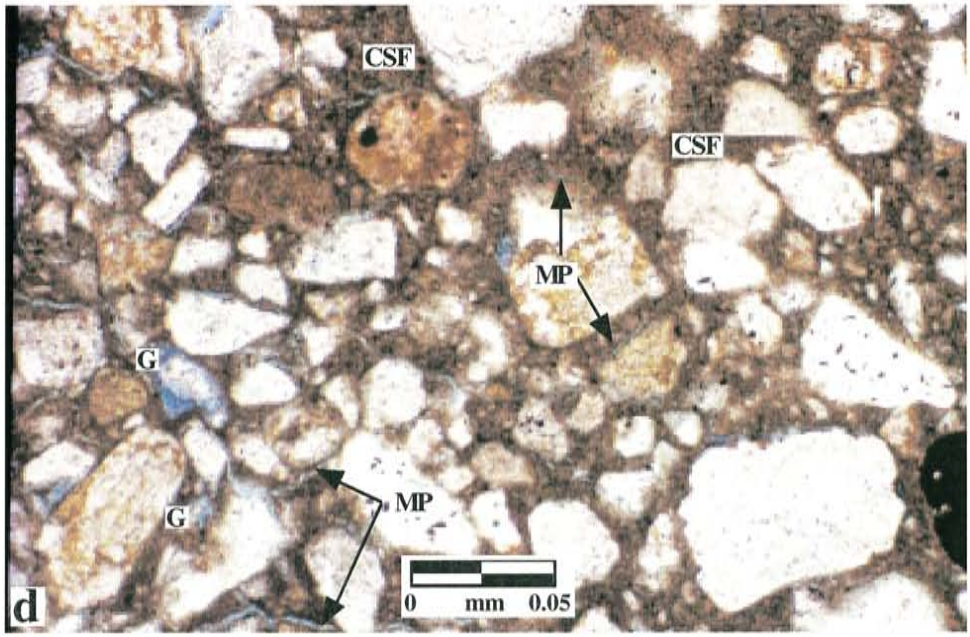

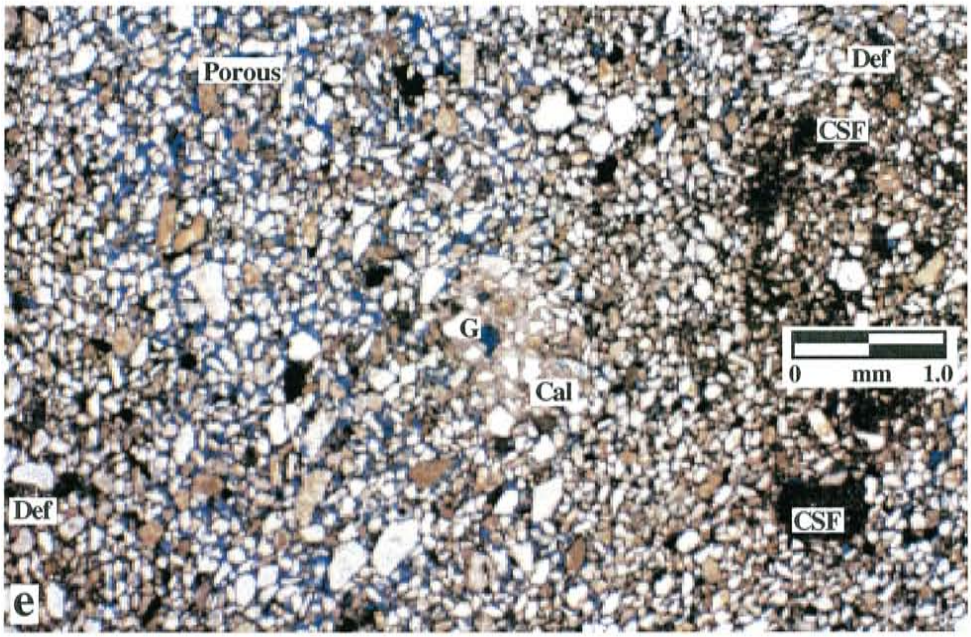

d) Close-up (400X) of cataclasite zone. Macroporosity is nearly eliminated by a substantial increase in red-brown clay-size fraction (CSF), leaving very narrow epoxy-filled bands, interpreted as micropores (MP). The largest pore is a ghost grain (G) formed by dissolution of a feldspar grain.

e) Cataclasite - Red 2 Zones. Zones of relatively greater deformation (Def) are separated by a more porous (center left) zone. Grain size is greatly reduced when compared to a). The clay-size fraction (CSF) remains very high on the right and left of the image. Rarely occurring calcite cement (Cal) is visible in the center surrounding a dissolution ghost grain (G).

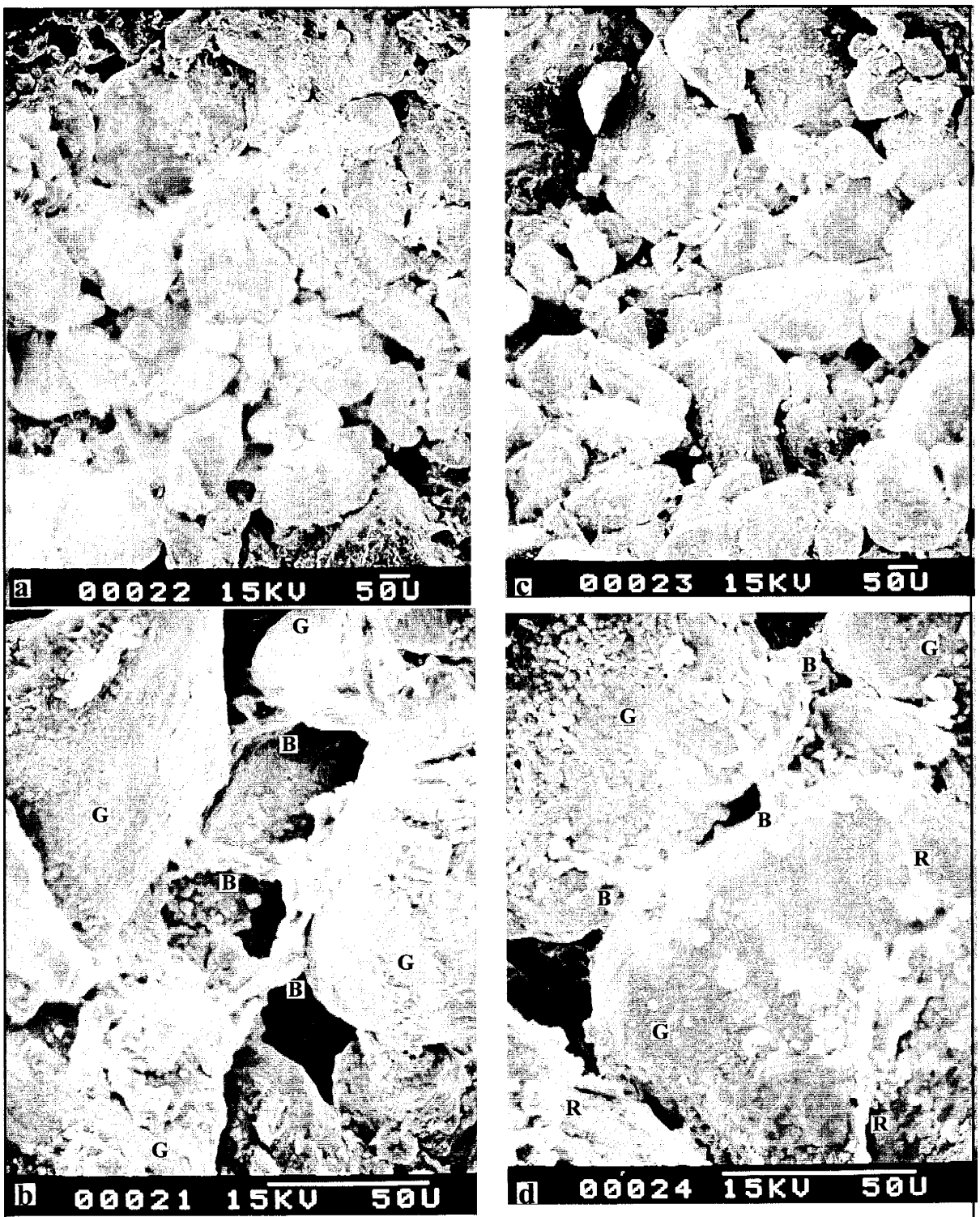

FIGURE 21: SEM Photomicrographs of Santa Ana Sands. a) Least-deformed fault zone structure (Buff 1 zone) pores are relatively open with few grains coated by clay-size fraction (CSF). **b)** Close-up of Buff 1 zone. Bridges (B) composed of CSF connect grains (G) and partially occlude pores. **c)** Red 1 zone appears similar to Buff 1 with small amounts of CSF.

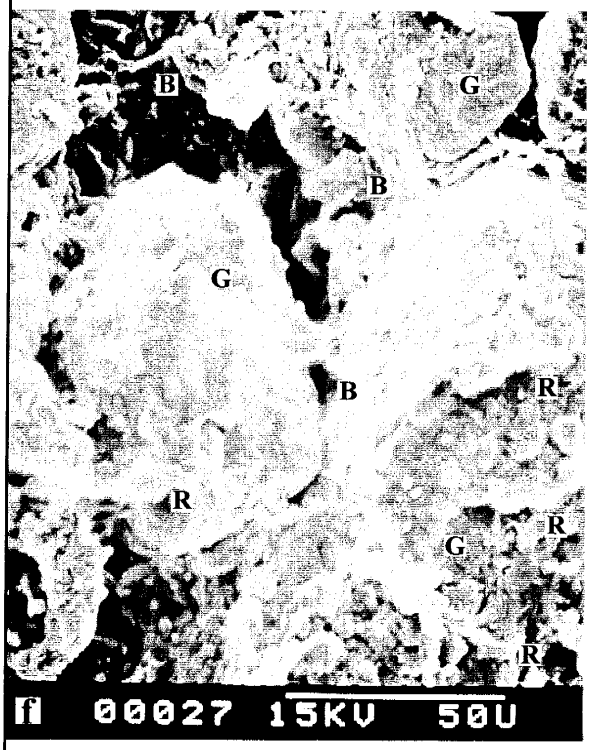

FIGURE 21: SEM Photomicrographs of Santa Ana Sands continued.

e) Cataclasite zone displays much more CSF coating grains and occluding pores.

f) Close-up of cataclasite zone. Bridges and ridges are thicker and more common.

g) Amount of CSF in Buff 2 zone is similar to that observed in Buff 1 zone. ($U = 10^{-6}$ m)

Porosity, Pore and Grain Sizes, and Clay-Size Fraction

Undeformed sands exhibit moderate macroporosity (> 20%), minor amounts of microporosity and clay-size fraction (< 6% each), and relatively large average pore sizes (Table 10, Table 11, Figure 15, and Figure 20). Total porosity, which is the sum of the two porosity types, is very similar for both sites: 26% and 28% for the Elmendorf and Santa Ana sites, respectively. Photomicrographs demonstrate slightly better grain sorting of Elmendorf undeformed sand (Figure 15) than Santa Ana undeformed sand (Figure 20a, b) and very little clay-sized material dispersed within the pores. Secondary porosity from grain dissolution is also observed in undeformed sands from both sites (Figure 15b and Figure 20b). SEM photomicrographs confirm the relative absence of clay-sized materials within pore spaces or coating the least deformed sand grains (Figure 18a, b and Figure 21a).

Table 10: Porosity Point Count Results - Elmendorf Site

Constituent[1]	Undeformed Sand	Slip Band A	Difference
Macroporosity	20.3	6.7	-13.6
Microporosity	5.3	10.3	5.0
Total Porosity	25.6	17.0	-8.6

[1] *Porosity types are percent abundance (% of total rock volume).*

Macroporosity decreases sharply within the Elmendorf fault zone's slip band A as microporosity doubles and clay-size fraction quadruples relative to undeformed sand. Total porosity, however, only drops by 34%. Slip band macroporosity and average pore size are greatly reduced by cataclasis as demonstrated by the observed grain-size reduction, grain reorientation, and the large increase in abundance of clay-sized materials (Figure 17). Compaction may also have reduced macroporosity. Pore size reduction is offset somewhat by secondary porosity created through grain dissolution (Figure 17b). SEM photomicrographs (Figure 18) further demonstrate the stark contrast between Elmendorf deformed and undeformed sands. The easily discernible undeformed-zone pores and grains (Figure

18a, b) are almost entirely occluded or blanketed by clay-sized materials within slip band A (Figure 18c, d). Clay-sized materials within slip band A are too thick, variable, and well-mixed to allow visual identification of component minerals, but their typical platy shape suggests that clay minerals constitute a sizable fraction (Figure 18).

Table 11: Porosity Point Count Results - Santa Ana Site

Constituent[1]	Downthrown Undeformed	Buff 1	Red 1	Cataclasite	Red 2	Buff 2
Macroporosity	23.5	18.7	15.7	3.0	7.0	13.7
Microporosity	4.7	5.3	7.7	13.8	8.7	8.7
Total Porosity	28.2	24.0	23.4	16.8	15.7	21.7

[1] *Porosity types are percent abundance (% of total rock volume).*

Porosity varies widely across the Santa Ana deformed zones and appears to be controlled by deformation and initial porosity of the different parent sands. Changes in macroporosity closely follow the pattern observed for mean permeability in undeformed and deformed zones (Figure 19). The cataclasite zone, with the lowest mean permeability, has the lowest macroporosity (3%), highest microporosity (14%), and lowest total porosity (17%) measured at the site (Table 11 and Figure 19). The red 2 and buff 2 zones have the next lowest macroporosity (and mean permeability) values and next highest microporosity values. The unknown but probably different porosity values for the parent red and buff sand units from the upthrown block may have been responsible for the lower total porosity and macroporosity estimates observed for the red 2 and buff 2 zones and, possibly, the cataclasite zone relative to the buff 1 and red 1 zones. As average grain size is smaller in the cataclasite than anywhere else in the fault zone, it is likely that cataclasis is also responsible for the cataclasite's low macroporosity and high microporosity values. The red 1 and especially the buff 1 zones display porosity values much closer to those observed for the downthrown undeformed sand, from which they likely derived some of their sediments.

Grain and pore sizes vary across and within the Santa Ana deformed zones (Figure 20). Average grain size is smallest in the cataclasite and next smallest in the red 2 zone, but largest within the buff zones (Figure 20a, e and Figure 21). Accordingly, average pore size is greatest within the buff zones but smallest in the red 2 and cataclasite zones, within which it is primarily confined to ghost grains and long, narrow, epoxy-filled channels which are interpreted as micropores (Figure 20d). Heavily deformed bands (large amounts of clay-size fraction and grain/pore size reduction) alternate with less deformed bands (relatively small pore and grain sizes and less clay-size fraction within the pores) in the cataclasite and red 2 zones (Figure 20d, e). Less deformed bands show evidence of elongate grain alignment sub-parallel to fault dip (Figure 20e).

SEM photomicrographs of Santa Ana deformed zones visually confirm the changes in clay-size fraction, porosity, and average sizes of pores and grains (Figure 21). Undeformed sand samples were too friable to permit SEM imaging. Deformation baseline is represented by the least deformed sample that can still be imaged with SEM (Figure 21a). Collected from the buff 1 zone, the baseline sample exhibits the least amount of grain coating and pore occlusion by clay-sized material. The red 1 zone displays slightly more and the cataclasite zone displays the greatest amount of clay-sized material (Figure 21). The buff 2 zone sample, taken from the 2-3 cm thick slip band B, has an amount of clay-sized material similar to that observed in the buff 1 and red 1 zones (Figure 20g). Higher resolution imaging revealed clay-sized materials coat grains and form microstructures which resemble ridges and bridges (Figure 21b, d, and f). Ridges are elongate microstructures rising up from a grain's surface. Bridges, too, are oriented more or less normal to grain boundaries but span pores. Thinner and sparsely distributed in the buff and red zones (Figure 21b and d), bridges appear appreciably thicker and more numerous within the cataclasite zone (Figure 21f). The cataclasite also contains assemblages of platy clay-sized materials that partially to completely fill pores and, unlike the bridges, are oriented roughly parallel to grain boundaries (Figure 21f).

DISCUSSION

Measuring the Permeability of Sands and Sandstones

Given the primary hypothesis test's heavy dependence on mini-permeameter measurements, prudence dictates an examination of their accuracy and potential biases. This section compares undeformed-zone permeability measurements from this study with those from previous permeameter studies of sands and sandstones and then discusses a probable bias in Elmendorf slip band permeability measurements caused by differences between scale of the structure and scale of the measurement.

Undeformed Sands and Sandstones

The undeformed-zone mean permeabilities reported here are in close agreement with previous mini-permeameter studies of poorly consolidated Santa Fe Group outcrops. Davis (1994) identified four eolian, poorly consolidated facies at another location on the Elmendorf outcrop and, using the same syringe mini-permeameter, found facies-specific mean permeability to range between 4.4 and 7.8 darcies with similarly small variances of the logarithms (0.01 and 0.04). Syringe mini-permeameter measurements of presumed eolian and moderately to well sorted, horizontally-laminated, poorly consolidated Santa Fe sands (e.g., Railroad facies 3HL; Rio Bravo facies 5HL) made by Detmer (1995) were typically 15 darcies or lower.

The accuracy of syringe mini-permeameter measurements is supported in part by the close match between observed grain sizes for the two Santa Fe undeformed sands and permeability values estimated from grain-size parameters. Detmer (1995) found that Beyer's empirical equation (Vukovic and Soro, 1992), which utilizes only grain size parameters d_{60} and d_{10}, had one of the best linear regression fits to 1300 mini-permeameter measurements made on a wide variety of Santa Fe group sediments. When applied to the grain size ranges observed at the Elmendorf and Santa Ana

undeformed zones, Beyer's formula produces a relatively good match to the observed values, estimating permeabilities of 11 and 17 darcies, respectively.

Santa Ana and Elmendorf undeformed-zone mean permeabilities are also in relatively close agreement with gas mini-permeameter studies of well consolidated sandstones. Chandler et al. (1989) reported permeability, as measured with a continuous flow mini-permeameter, varied with stratification type in the eolian, relatively well indurated Page sandstone (Arizona): grain flow laminae had the highest mean permeability (7.8 darcies), inter-dune/extra-erg deposits had the lowest (0.7 darcies) and wind-ripple laminae exhibited an intermediate mean permeability (2.3 darcies). Goggin et al. (1989) collected thousands of gas mini-permeameter measurements to compare mean permeability of three different eolian sandstones: the Page (Arizona) sandstone core and outcrop surface (4 and 6 darcies) and the Wyoming's Nugget sandstone (0.06 darcies) and Tensleep Formation (0.04 darcies) subsurface cores, both of which are better indurated and more deeply buried than the Page sandstone. Goggin et al. (1989) also reported a mean permeability of 12 darcies within one outcrop area of the Page sandstone. Using a laboratory gas permeameter, Antonellini and Aydin (1994) determined an average permeability of 1.5 darcies in the high porosity, eolian sandstones of the Entrada Formation (Utah). Dreyer et al. (1990) found mean permeabilities of 3.9 and 2.0 darcies in two moderately to well sorted channel sand body facies using a field gas mini-permeameter.

Leaving aside the very well indurated, low porosity Nugget and Tensleep sandstones, average permeability measurements reported here for the undeformed, poorly consolidated, eolian Santa Fe sands all fall within a single order of magnitude of the mini-permeameter measurements reported for more indurated sandstones, e.g., Page (Arizona) and Entrada (Utah) sandstones. Adopting as a first order estimate of eolian sandstone permeability the Carmen-Kozeny relation, in which intrinsic permeability is defined as a function of the square of some grain size measure, and a conservative, two order of magnitude range in grain size, one would expect a four order of magnitude range in individual

permeability values. Even after averaging, mean permeabilities should span at least two orders of magnitude. Why then is the observed range of mean permeabilities so narrow? Possible causes include instrument and operator error, differing depositional/diagenetic controls on permeability evolution, and instrument biases. As it is not possible to evaluate instrument and operator errors for all the studies cited, the discussion focuses on the latter two possible causes.

Permeability evolution, which depends on sedimentary provenance, depositional environment, and diagenesis, may have been responsible for the narrow modern day permeability differences observed in the well indurated sandstones mentioned above and this study's two Santa Fe Group outcrops. Deposited in large (continental) scale erg environments, much of the Page and Entrada eolian sandstones (as opposed to their sabhka or interdune units) are typically composed of very fine to fine grained quartzose sands (Blakey et al, 1983; Kocurek and Dott, 1983), and so they contain less silt, clay, feldspars, and volcanic rock fragments relative to the Santa Fe Group eolian lithic arkose sands. These differences in provenance and depositional environment would tend to make the Page and Entrada sandstones more permeable than the two Santa Fe Group sands because they contain little of the permeability-reducing, finer-grained or easily altered sediments common at the Elmendorf and Santa Ana sites. Differences in diagenetic history, especially cementation, narrowed the gap in mean permeability because both the Page and Entrada sandstones contain larger amounts of cement (Pipiringos and Peterson, 1978; Blakey et al, 1983; Kocurek and Dott, 1983) relative to the uncemented, poorly consolidated Santa Fe Group sands. By decreasing pore and pore throat sizes, cementation reduced sandstone mean permeability. Therefore, evolution of permeability in the Page and Entrada sandstones began high and gradually decreased with cementation, whereas Santa Fe Group sands began with relatively low permeability (different provenance/depositional environment) but did not change through cementation, thus bringing mean permeabilities to closer agreement than would be expected on grain size differences alone.

Although it is not possible to compare instrumental bias between the syringe and continuous flow mini-permeameters used in the studies discussed above, tip seal quality is a problem common to all permeameter investigations (Hurst and Goggin, 1995; Suboor and Heller, 1995; Davis et al., 1993; Goggin, 1993 and 1988ab). Gas leakage through the tip seal - rock surface interface leads to overestimates of rock permeability. Leakage is controlled by a complex association of variables, including rock surface roughness, rock compressibility, tip seal material, tip seal application pressure, and tip seal orientation. Application pressure and orientation, which are most likely to vary with each operator as well as during each measurement, should contribute the greatest amount of variability across studies of similar rocks (e.g., sandstones). Recent laboratory continuous flow permeameter investigations of permeability upscaling demonstrated measurement sensitivity to tip seal application pressure: permeability measured using a 0.62 cm ID tip seal on a block of Berea Sandstone was found to decrease by 10% as the tip seal application pressure was increased from 1 to 3 MPa (Tidwell and Wilson, 1997). It is possible that indurated sandstone measurements are biased relative to poorly consolidated sediment measurements. Overestimation bias from tip seal application pressure is counteracted in these sediments to an unknown degree by compaction-induced underestimation of permeability. Recent innovations in mini-permeameter design made at the New Mexico Institute for Mining and Technology may help to quantify this bias by reducing the difficulty in achieving a consistent tip seal application pressure at the outcrop face (J. Wilson, personal communication, 1996).

This study's estimates of undeformed-zone permeability are supported by earlier mini-permeameter studies of poorly consolidated Santa Fe Group sediments. The narrow range in mean permeabilities for poorly consolidated Santa Fe Group sands and well indurated sandstones is probably caused by a combination of differences in mini-permeameter bias, operator and instrument error, and differences in permeability evolution.

Deformed Sands

The relatively small number of normal to fault measurements collected at the Elmendorf site show a significant decrease in the permeability of slip band A in comparison to the parallel-to-strike measurements made at the same or nearby locations. These differences may be caused by local variability in permeability. It is more likely, however, that the differences are a function of the tip seal's orientation to the fault surface. The two pairs of matched parallel to fault and normal to fault measurements were collected at locations along slip band A where the downthrown block is missing. The CFMP tip seal inner diameter (3 mm) spans one third to one fourth of the slip band A thickness. This implies violation of boundary and geometry conditions for the mini-permeameter's half space solution during parallel to fault measurements at these locations because gas interrogating the low permeability slip band quickly escapes through the narrow structure to the atmosphere. The normal to fault measurements at these locations are therefore more representative of the slip band permeability than the parallel to fault measurements. This perceived or artifact permeability anisotropy caused by the Elmendorf outcrop topography is not likely to be significant at the Santa Ana site given the greater thicknesses of its deformation structures.

Normal to fault measurements, while more representative of Elmendorf fault zone permeabilities, may still underestimate the structure-specific permeability of the distributed shear zones. First, CFMP measurements are prone to permeability overestimation from insufficient tip seal application pressure for the reasons discussed above. Secondly, CFMP depth of investigation may exceed the thickness of the slip bands at the Elmendorf fault zone. Suboor and Heller (1995) estimated the depth of investigation of the Petroleum Resource Recovery Center (PRRC) syringe permeameter at the New Mexico Institute of Mining and Technology, Socorro, NM to be equal to the outer radius of their tip seal multiplied by a factor of 1.7 for $b_D = 2$ (outer radius : inner radius). If the CFMP follows the same relationship as the PRRC permeameter then average CFMP depth of investigation is 10 mm,

suggesting normal to fault measurements are almost wholly confined to the 7 - 13 mm thick distributed shear zone. If, however, the CFMP interrogates a significant thickness of the high permeability (10 darcies) upthrown block sands adjacent to the slip band, the structure-specific permeability may well be lower than that suggested by the normal to fault measurements.

Deformation, Porosity, and Permeability

Permeametry results from this study support the primary hypothesis: faulting can create significant permeability differences between undeformed and deformed poorly consolidated sands. Petrographic observations reported in this study reveal the importance of deformation in dictating the permeability of faulted, poorly consolidated sands, and thereby provide partial support for the second hypothesis: permeability alterations within poorly consolidated sand fault zones is caused by deformational and diagenetic processes. This section examines the causal relationship between the permeability and porosity differences observed for deformed and undeformed sands and the deformational processes (e.g., cataclasis and its attendant grain and pore size reduction, repacking and reorientation of grains, and drag and mixing of clay laminae or beds) relevant to each study site. The resulting relationships between deformation, porosity, and permeability for faults in poorly consolidated sands are compared with those documented for well indurated sandstones.

At the Elmendorf site, the largest reductions in macroporosity and permeability relative to the undeformed parent sand are associated with sharply localized deformation, primarily cataclasis and possibly compaction, within the slip bands (Figure 10 and Figure 17). Drag and mixing of clay-rich beds into the slip bands are not likely to have been significant deformation processes because clay beds or laminae are rare at the Elmendorf site and limited to a centimeter or less in thickness. The largest single clay lamina at the site appears to been dragged into slip band A and may have helped increase clay-size fraction locally. The most important petrographic alterations attributable to cataclasis within slip band A include average grain and pore size reductions and a manifold increase in

clay-size fraction, relative to undeformed sand, by fracturing and comminuting weaker feldspar and volcaniclastic grains (Table 7, Figure 15, and Figure 17). By directly affecting pore and pore throat size distributions through these alterations, deformation significantly reduced slip band permeability.

Permeability does not appear to be very sensitive to vertical displacement for even though slip band B only experienced 65 - 74% of the vertical displacement accommodated by slip band A, the ranges of parallel to fault permeabilities observed for the two bands were roughly the same (A: 0.2 - 0.5; B: 0.2-0.3). Normal to fault permeability, which was not measured for slip band B, may be more sensitive to amount of displacement than parallel to fault permeability. Moreover, the two faults may have accommodated different amounts of strike-slip displacement. Petrographic analysis of slip band B and the numerous deformation bands should provide a better understanding of the relationship between displacement and reduction in grain and pore size, macroporosity, and permeability.

The observed association between a relatively small drop in slip band A macroporosity, from 20% to 7% (Table 10), and a two to three order of magnitude decrease in permeability is in keeping with reported ranges of macroporosity and permeability for sands and sandstones. Pittman (1981) determined that faulting in a friable sandstone caused a three order of magnitude decrease in permeability (from 2600 to 2.5 millidarcies) but only a 38% decrease in porosity (25.5% to 15.8%). Compaction and cementation reduced porosity from 16% to 5% but reduced permeability four orders of magnitude in the clean sandstones of the Lower Cretaceous Travis Peak Formation of east Texas (Dutton and Diggs, 1992). Likewise, Liu et al. (1996) measured a four order of magnitude permeability range but only a 25% to 5% porosity range in the Triassic Hawkesbury braided stream sandstone of Australia's Sydney Basin.

Deformation processes observed at the Santa Ana site include cataclasis and drag and mixing of clay-rich beds into the fault zone. Cataclasis can be inferred from the large reduction in average grain

size within the cataclasite zone relative to the rest of the fault zone, especially the adjacent red 2 and buff 2 zones (Figure 20 and Figure 21). Diagenetic alternation of the comminuted feldspar and volcaniclastic grains may then have contributed to the large clay-size fraction observed in the cataclasite and two red zones. Inferred from the thickness and vertical continuity of the clay core and the similar clay mineral compositions determined for the clay core, cataclasite, and downthrown block's clay bed (Table 9), drag and mixing are likely responsible for a significant proportion of clay minerals observed in the Santa Ana fault zone. X-ray diffraction data show little compositional difference between the downthrown block's clay bed and all fault zone samples (Table 9), and thus support the interpretation that material from the clay bed exposed in the downthrown block (Figure 5) had been dragged into the fault zone. Contiguity of the cataclasite and red 2 zones to the clay core suggest that mixing of dragged clay with the various parent sands could explain the large clay-size fraction observed within the cataclasite and red 2 zones relative to the rest of the fault zone. However, this is contradicted by the relatively small clay-size fraction determined for the red 1 zone, which is also contiguous with the clay core, unless drag and mixing behave differently for the footwall than the hanging wall.

Discerning deformation's contribution to fault-zone permeability at the Santa Ana site is complicated by lack of constraints on displacement history and number of and hydraulic characteristics of the various parent sediments which now form the fault zone. By reducing the average grain and pore sizes of the various unknown parent sediments as well as increasing the abundance of clay minerals and clay-sized particles, bed drag with mixing and cataclasis helped create the very low macroporosity and permeability values observed in the cataclasite and red 2 zones (Table 8, Figure 11, and Figure 19). Without the constraints on displacement and parent sediments, it is not possible to resolve the importance of mixing low permeability undeformed sediments into the fault

zone relative to the importance of deformation, nor is it possible to conclude that faulting significantly altered the permeability of the Santa Ana parent materials at the site.

Under fully saturated conditions, the clay core (Figure 6) may have a permeability many orders of magnitude lower than any of the red, buff, or cataclasite zones because of its primarily clay composition. Clay core permeability will be a function of its clay mineral composition, thickness (which ranges from 1 to 15 cm at the outcrop face), number and thickness of splays, and its lateral and vertical continuity. The clay core could resemble, in hydrologic behavior, clay smear seals created by faults in the interbedded shales and sandstones found in many hydrocarbon reservoirs (Smith, 1966 and 1980; Berg and Avery, 1995).

The association reported in this study between faulting-induced grain and pore size reduction and low permeability for faults in poorly consolidated sands has been well documented for faults in well indurated sandstones (Pittman, 1981; Antonellini and Aydin, 1994; Antonellini et al., 1994; Fowles and Burley, 1994). Fault structures in poorly consolidated sands, however, show several noteworthy differences.

The first difference is increased variability in porosity reduction within deformation structure as evidenced by bands of greater deformation alternating with bands showing much less deformation in the Santa Ana cataclasite zone (Figure 20d and e). Similar bands were also observed within the Elmendorf site's slip band A. In contrast, cataclasis in well indurated sandstones tends to eliminate all macroporosity for displacements greater than the several millimeters associated with deformation band formation (Pittman, 1981; Edwards et al., 1993; Antonellini and Aydin, 1994; Antonellini et al., 1994; Fowles and Burley, 1994). Thus, any given displacement greater than several millimeters yields smaller macroporosity reductions in poorly consolidated sand than in well indurated, porous sandstone.

The second difference lies in the four to five-fold increase in abundance of clay-sized materials, including clay minerals, through cataclasis of poorly consolidated sands. Pittman (1981) reported only rearrangement and disruption of illitic grain coatings for a 15 cm-displacement fault in friable sandstone, not increased clay-size fraction. Antonellini et al. (1994) described increased abundance of a very fine-grained cataclasite which had been partially altered to clay minerals, within well indurated sandstone deformation bands. None of the other studies cited above mention any sizable changes in clay-size fraction within faulted, well indurated sandstones.

Diagenesis, Porosity, and Permeability

Petrographic and X-ray diffraction results from this study further support the second hypothesis: diagenetic processes (as well as deformational processes) can cause permeability differences between faulted and undeformed sands. In particular, diagenetic processes such as alteration of less stable feldspars and rock fragments to clay minerals, fluid-mediated redistribution of clay-sized materials, and incipient cementation can be inferred from observations reported in this study. Each of these processes can, by reducing macroporosity and pore interconnectivity, decrease permeability. This section examines the evidence for and against inferring diagenesis and its influence on fault zone permeability at each site.

Santa Ana Site

Whereas the parallel to grain orientation of platy, pore-filling materials seen in the Santa Ana cataclasite zone (Figure 21f) suggests they may have been emplaced through deformation as clay-rich beds were dragged and mixed into the fault zone, the fragility of the ridges and bridges observed within the Santa Ana red, buff, and cataclasite zones suggests the microstructures could not have withstood much displacement (Figure 21). This leaves post-slip diagenesis as most likely responsible for forming these microstructure, but which particular process or processes? The choice depends in part on the composition of the microstructures.

SEM imaging did not reveal any recognizable clay minerals forming the Santa Ana fault zone bridges, ridges, platy assemblages, and grain coatings, but there is some evidence which supports a primarily clay mineral composition. First, the platy shape and small size of much of the Santa Ana fault-zone clay-size fraction points to a clay mineral composition. Second, the relatively equal semi-quantitative weightings given by XRD analysis to each of the four clay mineral families identified imply there is a low probability that any one clay mineral type will predominate and allow visual recognition with SEM. Furthermore, it is not possible to discriminate clay mineral abundance relative to the abundances of calcite, quartz, and feldspar, each of which was detected by XRD analysis within several Santa Ana clay-size fraction samples, because none of the three minerals were visually identified during SEM imaging and because the XRD results are only semi-quantitative. In the absence of more definitive mineral composition data (e.g., from electron microprobe analysis), the remainder of this discussion assumes the fault zone microstructures are primarily composed of clay minerals because of the typical platy shape and small size of the clay-size fraction particles imaged with SEM.

Mechanical infiltration of clays into sands is one diagenetic process potentially responsible for the Santa Ana ridges, bridges, and grain coatings. Clay mineral microstructures which appear very similar to those in the Santa Ana fault zone have been attributed to mechanical infiltration (Crone, 1975; Walker, 1976; Matlack et al., 1989; Moraes and de Ros, 1990), which is defined as a post-deposition process of emplacing clay minerals through periodic flooding of sands and gravels by muddy or silty water which then carries the clays into the sediments as it percolates downward. The clays adhere to the grains, forming cutans (clay particle coatings oriented parallel to grain surfaces), pendular aggregates or geopetal fabrics in which clay particles accumulate at the bottom of large pores, ridges, and bridges. It has been suggested the latter two microstructures can be formed under unsaturated conditions when clay particles accumulate along water films and menisci (Crone, 1975;

Matlack et al., 1989; Moraes and de Ros, 1990). Matlack et al. (1989) have also suggested bridges and ridges are cutans relicts from grain plucking caused by SEM sample preparation and observation. Evidence for mechanical infiltration of clays has been observed in several arid and semi-arid environments, including the southwestern United States (Crone, 1975; Walker, 1976; Walker et al., 1978; Moraes and de Ros, 1990).

Together with mechanical infiltration's definition as essentially saturated transport of clays, the differences in measured permeability between the downthrown undeformed buff sand and the Santa Ana fault zone do not support preferential mechanical infiltration of clays into the less permeable fault zone relative to the more permeable undeformed downthrown buff sand under saturated conditions. Clay minerals from the downthrown block's clay bed may have mechanically infiltrated into the undeformed downthrown buff sand because the XRD data show little or no differences in clay mineral composition between the two units (Table 9).

Fluid-mediated redistribution of clays, defined here as the diagenetic equivalent of two important pedogenic processes: eluviation and illuviation, is a more likely to have formed the Santa Ana ridges and bridges because it does not conflict with the measured permeabilities. Eluviation, defined as transport of clays away from a soil horizon (emigration of clays), complements illuviation in which clays are concentrated within a soil horizon (immigration of clays). Matlack et al. (1989) cite a number of soil scientists who have reported clay mineral microstructures similar to those seen in the Santa Ana fault zone and have attributed their formation to eluviation and illuviation. Although these pedogenic processes occur under saturated or unsaturated conditions, the association between small average grain and pore sizes, large microporosity abundance, high clay-size fraction (and clay mineral abundance), and greater density of ridges and bridges in the cataclasite and red 2 zones suggests that flow under unsaturated conditions is more plausible than saturated flow. Clay particles may have collected at air-water interfaces and been deposited as bridges or bridges once the menisci or films

dried up. Under this scenario, diagenetic redistribution of clays through unsaturated flow may further reduce permeability because the microstructures further constrict pores and pore throats.

The presence of optically unresolvable calcite, which was detected by XRD analysis within the clay-size fraction of several Santa Ana fault-zone samples, potentially supports the importance of unsaturated flow to fault zone diagenesis. Varying from a minor to major component, calcite was detected in the clay-size fraction from the red 1 and cataclasite zones and from the clay bed (Table 9). Calcite was not detected in the fault clay core or in the downthrown undeformed buff sand. Optical analysis revealed negligible quantities of calcite cements throughout the deformed and undeformed sands except in the red 2 zone, where trace amounts were found. This suggests that calcite detected in the clay-size fraction by XRD is sufficiently fine-grained micro-spar or micrite to escape observation by petrographic microscope. Moreover, higher calcite abundance in those zones with the highest clay content points to the likelihood that unsaturated flow increased calcite abundance, relative to the buff 1 zone (where calcite was a minor clay-size fraction component), because the unsaturated flow should be greater in materials with higher clay content and smaller pores (cataclasite and red 1 zones) than materials with larger pores and less clay (buff 1 zone). The lack of calcite in the fault clay core, as determined by XRD analysis, suggests that either the clay dragged into the fault did not originate from the clay exposed in the downthrown block or, more likely, that cementation of the clay bed postdated fault slip. It is also possible that the single fault clay core sample was unrepresentative or that the fault clay core had undergone leaching of calcite subsequent to fault slip. Further work, such as electron microprobe analyze, is required to better quantify calcite abundance and to identify the type and sources of calcite in the clay-size fraction.

Elmendorf Site

The well constrained vertical displacement at the Elmendorf site allows a more conclusive assessment of faulting-induced petrophysical and hydrological changes through direct comparison of

undeformed and deformed zones than is possible at the Santa Ana site. Changes attributable to diagenesis within the Elmendorf slip bands include preferential alteration of feldspars and possible alteration of the comminuted feldspar and volcaniclastic grains to clay minerals. Redistribution of clay minerals may also be a significant diagenetic process, but data are lacking in two important aspects. First, the composition of Elmendorf clay-size fraction is unknown (no XRD analyses were performed on samples from the Elmendorf site), but it is likely that slip band A's large clay-size fraction is primarily composed of clay minerals because of the many platy shaped particles seen in SEM (Figure 18c and d) and because a clay mineral, smectite, was observed coating an undeformed sand grain (Figure 18b). Secondly, there are no observations of ridges, bridges and other microstructures associated with redistribution of clay minerals, although slip band A grain coatings and pore fillings are so thick and extensive (Figure 18c and d) that they may be effectively obscuring all other microstructures. Note that an undeformed sand grain appears to have developed a ridge near its smectite coating (Figure 18b).

Point count data from the Elmendorf site reveal that 7% of slip band A's total feldspars are either corroded, heavily corroded, found as ghost grains, or exhibit large amounts of micro-porosity or carbonate replacement, versus 3% of all feldspars in the undeformed sand. These diagenetic alterations are commonly associated with preferential fluid flow: if more fluid flows through a unit, it should have a greater the number and degree of alterations than another unit with less fluid flux, assuming no differences in pore fluid chemistry or mineral abundance between the two units. The 133% increase in altered feldspars observed in slip band A relative to the undeformed sand indicates that fluids moved preferentially through slip band A because their compositions were initially the same and because there is little likelihood, given slip band A's small scale, that pore fluids varied significantly in composition between deformed and undeformed zones. Such an increased fluid flux would also be expected to alter the comminuted or crushed feldspar and volcaniclastic grain fragments

to clay minerals. The large differences in measured permeability between the undeformed sand and the slip bands make it unlikely that this preferential flow occurred under saturated conditions. Therefore, mechanical infiltration, as described by Moraes and de Ros (1990) and Matlack et al. (1989), and eluviation-illuviation under saturated conditions were not important diagenetic processes within slip band A, leaving increased fluid flux under unsaturated conditions as the most likely explanation.

Evidence reported in this study allows construction of an interesting hypothesis which interrelates fault-induced deformational and diagenetic alterations with changes in permeability and porosity, given the assumption that slip band A's high clay-size fraction is composed of mainly clay minerals. Grain comminution and crushing of corroded or vacuolized grains during fault-induced cataclasis increase clay-size fraction within the slip band. Gains in fine-grain abundance and microporosity as well as a concomitant decrease in average pore size likely improved the slip band's water-retention capacity, relative to the parent sand. Preferential water flux through the slip band, now under unsaturated conditions, would combine with the manifold rise in surface area to accelerate alteration of the comminuted or crushed grain fragments into clay minerals, further adding to the deformed zone's water retention capacity. Diagenetic alteration of whole grains would also quicken in comparison to the undeformed zone from greater water flux and possibly from the greater alkalinity (abrasion pH) released by grain crushing (Whitworth et al., 1996). Preferential unsaturated water flux might also redistribute clay minerals and other clay-size fraction materials to form ridges, bridges, pore fillings,, and grain coatings (such as those observed in the Santa Ana fault zone) in accord with the unsaturated physical processes, such as clay particle concentration at menisci during drying, cited by Moraes and de Ros (1990) and Matlack et al. (1989). Occlusion of pores and pore throats would further increase the deformed zone's ability to retain water under high hydraulic tensions and thus its unsaturated hydraulic conductivity. The sequence of physical processes

described in this hypothesis suggests fault zones in poorly consolidated sediments are self-reinforcing or self-organizing under unsaturated conditions. Before testing of such a hypothesis can begin, the clay-size fraction composition for the Elmendorf site must be determined and the differences in abundance of altered feldspars should be confirmed.

Summary

The hypothesis that faulting can significantly alter the permeability of poorly consolidated sands is supported by this study's permeability measurements. Undeformed-zone permeability measurements are in close agreement with other mini-permeameter studies of poorly consolidated Santa Fe Group sediments. The true difference between deformed and undeformed sands at the Elmendorf site is likely to be larger than reported in this study because the maximum volume interrogated by the continuous flow mini-permeameter probably includes some of the high permeability undeformed sand in zone A-B.

The hypothesized impact of deformational processes on fault-zone permeability (second hypothesis) is supported by observations of cataclasis and possibly compaction within the Elmendorf fault zone's slip band A and observations of drag and mixing of clay-rich beds to form a thick clay core and possibly contribute part of the large clay-size fraction/clay mineral abundance observed in the red and cataclasite zones within the Santa Ana fault zone. Low fault zone permeability is typically associated with reductions in macroporosity and average grain and pore sizes and with a large clay-size fraction or large clay mineral abundance.

Evidence for faulting-related diagenetic alterations further supports the second hypothesis that deformational and diagenetic processes change fault zone permeability. Increased frequency of microstructures such as ridges, bridges, and grain coatings are associated with low fault zone permeability at the Santa Ana fault zone; the microstructures' apparent fragility argues for creation by

diagenesis rather than deformation. Data from the Elmendorf site indicate that diagenetically altered feldspars may be much more abundant within slip band A than in the undeformed sand. The common association between such alterations and high fluid fluxes suggest that slip band A experienced preferential fluid flux, relative to the undeformed sand. Observed permeability differences between slip band A and the undeformed sand indicate that the increased fluid flux through slip band A did not occur under saturated conditions.

FUTURE WORK

If only because this study constitutes the author's first foray into several of the disciplines employed, a number of different methodological problems were encountered along with the new data. The list below of "lessons learned" point to future work which would further bolster the hypothesis tests described in this study as well as help incubate new hypotheses.

Petrologic sampling should be expanded to include replicate samples from undeformed and deformed zones to test whether the data presented in this study are truly representative. The upthrown block undeformed sands (both red and buff sand units) at the Santa Ana site and all of the unsampled Elmendorf fault zones structures (zone A-B, zone of deformation bands, slip bands B and C) should be examined. The composition of clay-size fraction from all Elmendorf site fault zone structures and the undeformed zone needs to be determined.

The expanded petrologic analysis should also compare outcrop face samples with those collected from deeper within the outcrop (at least 1-2 m) to test the influence of surface weathering on mineral abundance differences between undeformed and deformed sands.

Quantitative grain size analysis through sieving and optical microscopy would improve characterization of the undeformed sands and of the amount of deformation experienced in each fault zone structure. Digital imaging of pore networks will provide data for comparing pore size distributions and evaluating the connectivity of pores in undeformed and deformed sands.

Many more permeameter measurements are needed to fully characterize the permeability distribution within slip bands and other fault zone structures. The geostatistical analyses would benefit from more exhaustive sampling using a regular grid.

A larger number of faults encompassing a wider range of displacements should be investigated to satisfy doubts whether the two sites described in this study are truly representative and to see whether amount of displacement influences the amount of cataclasis and permeability reduction. Comparisons between faults in other poorly consolidated sediments: fluvial sands, silts, etc., with eolian sands will help elucidate controls exerted by grain size, grain cohesion, and strength.

In-depth study of fault controls on the permeability distribution of poorly consolidated sediments must be complemented with better information about fault density and spatial distributions before it is possible to determine at what scales these faults affect saturated fluid flow.

The changes in pore size and clay-size fraction strongly suggest that small displacement faults in poorly consolidated sands may possess unsaturated hydraulic conductivities which are greater than those of the undeformed sands at the high soil water tensions common in the arid Southwest. A comparison of unsaturated hydraulic properties for deformed and undeformed sands would help evaluate whether these faults can act as preferential pathways for unsaturated fluid flow.

CONCLUSIONS

Small-displacement slip events of at least 0.5 m within the poorly consolidated sands of the Santa Fe Group create a variety of laterally extensive deformation structures, notably deformation bands (< 0.2 cm thick), zones of relatively undisturbed sediments (60 - 90 cm wide), zones of deformation bands (< 30 cm thick), narrow (< 2 cm) slip bands, vertically continuous clay core (1 - 15 cm thick), and sub-vertical zones of varying deformation which vary in thickness from 0.7 to 20 cm.

Undeformed-zone permeability for the two poorly consolidated sands appears to fit log-normal distributions with small variances and, coincidentally, means of approximately 10 darcies.

Total vertical displacement (< 0.6 m) and parent sand characteristics are well constrained for the Elmendorf site. The minimum vertical displacement at the Santa Ana site is 2.5 m and may be much more. Comparisons of hydrologic and petrophysical characteristics between the Santa Ana fault zone and the downthrown undeformed buff sand are not warranted because the fault zone contains many different unknown parent sediments.

Permeametry results at the Elmendorf site support the hypothesis that faulting of poorly consolidated sands can significantly alter permeability of the faulted sands relative to the parent sands. Mean permeability for the Elmendorf fault zone is one half of the parent sand mean permeability. Variance about mean fault zone permeability is four times larger than the variance about the undeformed zone permeability. Mean permeability for the zone of greatest deformation, Elmendorf slip band A, totals no more than 4 - 5% of mean undeformed sand permeability. The range of individual parallel to fault permeability measurements for undeformed and deformed zones spans two orders of magnitude; normal to fault permeability measurements increase the span to roughly three orders of magnitude.

Permeametry data from the Santa Ana site also demonstrate a large difference in permeability between faulted and unfaulted sands, although some or all of this difference may be caused by the unknown permeabilities of various parent sands which formed the fault zone. The lowest measured permeabilities at the Santa Ana site are found in the cataclasite and two red zones within the fault zone. The lowest individual permeability measurement for the cataclasite zone is 0.14 darcies; minimum individual permeability measurements for the red 1 and red 2 zones are 0.14 and 0.28 darcies, respectively. Variance about mean fault zone permeability is four times that for the downthrown undeformed buff sand.

Permeametry measurement errors constitute a very small to negligible component of sampling location-specific permeability estimates. Geostatistical analysis indicated a very short-scale undeformed-zone spatial correlation structure at the Elmendorf site and no spatial correlation in the Santa Ana downthrown undeformed buff sand. Neither measurement error nor spatial heterogeneity in permeability have any impact on support for the hypothesis that faulting in poorly consolidated sands alters the permeability significantly.

Petrographic analytical results support the hypothesis that deformational processes contribute to the change in fault-zone permeability. Low fault zone permeability appears to correlate positively with the amount of deformation, which can be characterized by low macroporosity, small average grain and pore sizes, and large clay-size fraction or clay mineral abundance. For example, macroporosity decreased from >20% in undeformed sand to 5% in slip band A at the Elmendorf site whereas slip band A clay-size fraction increased four-fold. Deformation, through bed drag and mixing, helped alter fault zone permeability through formation of a continuous clay core and through contributing to the high clay mineral abundance observed in the cataclasite and two red zones, which also exhibited the lowest permeabilities.

Support for the hypothesis that faulting-related diagenetic processes influence fault zone permeability is demonstrated by redistribution of clay-sized materials subsequent to fault slip. Fault zone clay minerals or clay-size fraction materials are redistributed within the Santa Ana fault zone to form microstructures (grain coats, ridges, and bridges) which occlude pore bodies and throats. These microstructures resemble features attributed to the pedogenic processes eluviation and illuviation and mechanical infiltration of clays, which describe movement of clay minerals and clay-sized materials through porous media. The fragility of these microstructures strongly suggests they are the result of post-slip diagenesis and not deformation.

Support for the hypothesis that faulting-related diagenetic processes also influence fault zone permeability is also demonstrated by increased diagenetic alteration of fault-zone feldspars at the Elmendorf site. Diagenetic alteration of whole feldspar grains is more than twice as great within slip band A than in its parent undeformed sand, indicating slip band A experienced increased fluid fluxes relative to the undeformed parent sand.

This study's results support the hypothesis that deformational and diagenetic processes associated with small-displacement faults can significantly alter the original permeability of poorly consolidated sands through deformation and diagenesis. More work is required to better understand the spatial variability of fault zone petrophysical and hydrologic characteristics along strike and dip with the intent of more clearly discerning the hydrologic impact of small-displacement faults.

REFERENCES

Anderson, M.P. 1989. Hydrogeologic facies models to delineate large-scale spatial trends in glacial and glaciofluvial sediments. Geol. Soc. Amer. Bull. vol. 101 pages 501-511.

Antonellini, M.A., A. Aydin and D.D Pollard 1994. Microstructure of deformation bands in porous sandstones at Arches National Park, UT. J. Struct. Geol. vol. 16 :7 pages 941-959.

Antonellini, M. and A. Aydin 1994. Effect of faulting on fluid flow in porous sandstones: petrophysical properties. Am. Assoc. Petr. Geol. Bull. vol. 78 :3 pages 355 - 377.

Aydin, A. and A. M. Johnson 1983. Analysis of faulting in porous sandstones. Journal of Structural Geology vol. 5 :1 pages 19-31.

Aydin, A. and A.M. Johnson 1978. Development of faults as zones of deformation bands and as slip surfaces in sandstone. Pure and Applied Geophysics vol. 116 pages 931-942.

Aydin, A. and Z. Reches 1982. Number and orientation of fault sets in the field and in experiments. Geology vol. 10 :2 pages 107-112.

Aydin, Attila 1978. Small faults formed as deformation bands in sandstone. Pure and Applied Geophysics vol. 116 pages 913-930.

Barnett, J.A., J. Mortimer, J. Rippon, J. Walsh, and J. Watterson 1987. Displacement geometry in the volume containing a single normal fault. Am. Assoc. Petr. Geol. Bull. vol. 71 :8 pages 925-937.

Bear, J. 1972. Dynamics of Fluids in Porous Media . Dover. 764 pages.

Begg, S.H. and P.R. King 1985. Modeling the effects of shales on reservoir performance: Calculation of effective vertical permeability. Paper presented a the SPE Symposium on Reservoir Simulation, Dallas, TX 1985

Berg, R.R. and A.H. Avery 1995. Sealing properties of Tertiary growth faults, Texas Gulf Coast. Am. Assoc. Petr. Geol. Bull. vol. 79 :3 pages 375-393.

Bernard, D., M. Danis and M. Quintard 1989. Effects of permeability anisotropy and throw on the transmissivity in the vicinity of a fault. Hydrological Regimes and Their Subsurface Thermal Effects vol. Geophysical Monograph 47, IUGG Volume 2

Blakey, R., F. Peterson, M. Caputo, R. Gessaneu, and B. Voorhees. 1983. Paleogeography of middle Jurassic continental, shoreline, and shallow marine sedimentation, southern Utah, in Mesozoic Paleogeography of the West-Central United States, M. Reynolds and E. Dolly, eds., published by the Rocky Mountain Section of the SEPM, Denver, CO, pp. 77-100.

Bredehoeft, J.D., K. Belitz and S. Sharp-Hansen 1992. The hydrodynamics of the Big Horn Basin: a study of the role of faults. Am. Assoc. Petr. Geol. Bull. vol. 76 :4 pages 530-546.

Burley, S.D., J. Mullis, and A. Matter, 1989. Timing diagenesis in the Tartan Reservoir (UK North Sea): Constraints from combined cathodoluminescence microscopy and fluid inclusion studies. Marine and Petroleum Geology vol. 6 pages 98-120.

Caine, J.S., J.P. Evans, and C.B. Forster 1996. Fault zone architecture and permeability structure. Geology vol. in press

Carter, K.E. and C.L. Winter 1995. Fractal nature and scaling of normal faults in the Espanola Basin, Rio Grande rift, New Mexico: Implications for fault growth and brittle strain. Jour Struct Geol vol. 17 :6 pages 863-873.

Cather, S.M., R.M. Chamberlin, C.E. Chapin, and W.C. McIntosh 1994. Stratigraphic Consequences of Episodic Uplift in the Lemitar Mountains, Central Rio Grande Rift. Basins of the Rio Grande Rift: Structure, Stratigraphy, and Tectonic Setting vol. Special Paper 291 pages 157-170.

Chandler, M.A., G. Kocurek, D.J. Goggin, and L.W. Lake 1989. Effects of stratigraphic heterogeneity on permeability in eolian sandstone sequence, Page Sandstone, Northern Arizona. Am. Assoc. Petr. Geol. Bull. vol. 73 pages 658-668.

Chapin, C.E. and S. M. Cather 1994. Tectonic Setting of the Axial Basins of the Northern and Central Rio Grande Rift. Basins of the Rio Grande Rift: Structure, Stratigraphy, and Tectonic Setting vol. Special Paper 291 pages 5-26.

Collinson, J.D. 1986. Chapter 5: Deserts. Sedimentary Environments and Facies, second ed. pages 95-122.

Cowie, P., D. Sornette, and C. Vanneste 1995b. Multifractal scaling properties of a growing fault population. Geophys J. Int. vol. 122 pages 457-469.

Cowie, P., C. Vanneste, and D. Sornette 1993. Statistical physics model for the spatio-temporal evolution of faults. J. Geophys. Res. vol. 98 pages 21809-21821.

Cowie, P.A. and C.H. Scholz 1992a. Physical explanation for the displacement-length scaling relationship of faults using a post-yeild fracture mechanics model. Jour Struct Geol vol. 14 :10 pages 1133-1148.

Cowie, P.A. and C.H. Scholz 1992b. Displacement-length scaling relationship for faults: data synthesis and discussion. Jour of Struct Geol vol. 14 :10 pages 1149-1156.

D'Onfro, P., W. Rizer, and L. Cadle 1984. Changes in permeability and porosity during dilatant and compactive failure in Berea sandstone. EOS, Transactions of AGU, Nov. 6, 1984 vol. 65 :45

Davis, J.M. 1994. A Conceptual Sedimentological-Geostatistical Model of Aquifer Heterogeneity Based on Outcrop Studies. Ph.D. Thesis - Jan., 1994

Davis, J.M., J.L. Wilson, F.M. Phillips 1994. A portable air-minipermeameter for rapid in situ field measurements. Ground Water vol. 32 :2 pages 258-266.

Davis, J.M., R.C. Lohman, F.M. Phillips, J.L Wilson, D.W. Love 1993. Architecture of the Sierra Ladrones Formation, central New Mexico: Depositional controls on the permeability correlation structure. Geol. Soc. Amer. Bull. vol. 105 pages 998-1007.

Davis, S.N. and R.J.M. DeWeist 1966. Hydrogeology. John Wiley, New York.

Davison, C.C. and E.T. Kozak 1988. Hydrogeologic characteristics of major fracture zones in a large granite batholith of the Canadian Shield. Proc. 4th Canadian American Conference on Hydrogeology, Banff, Canada, June, 1988

Detmer, D.M., 1995. Permeability, porosity, and grain-size distribution of selected Pliocene and Quaternary sediments in the Albuquerque Basin: New Mexico Geology, v. 17, p. 79-87.

Deutsch, C. 1989. Calculating effective absolute permeability in sandstone/shale sequences. SPE Formation Eval. vol. 4 pages 343-348.

Deutsch, C.V. and A.G. Journel 1992. GSLIB Geostatistical Software Library and User's Guide. Oxford University Press, New York.

Dreyer, T., A. Scheie and O.Walderhaug 1990. Mini-permeameter-based study of permeability trends in channel sand bodies. Am. Assoc. Petr. Geol. Bull. vol. 74 pages 359-374.

Durlofsky, L.J. 1991. Numerical calculation of equivalent grid block permeability tensors for heterogeneous porous media. Water Resour. Res. vol. 27 :5 pages 699-708.

Durlofsky, L.J. 1992. Representation of grid block permeability in coarse scale models of randomly heterogeneous porous media. Water Resour. Res. vol. 28 :7 pages 1791-1800.

Dutcher, L.C. and A.A. Garrett 1963. Geologic and hydrologic features of the San Bernardino area, California; with special reference to underflow across the San . US Geological Survey Water-Supply Paper 114 :W 1419

Dutton, S. and T. Diggs. 1992. Evolution of porosity and permeability in the lower Cretaceous Travis Peak Formation, east, Texas. AAPG Bull. v. 76, no. 2, pages 252-269.

Edwards, H.E., A.D. Becker and J. A Howell 1993. Compartmentalization of an aeolian sandstone by structural heterogeneities: Permo-Triassic Hopeman Sandstone, Moray Firth, Scotland. Characterization of Fluvial and Aeolian Reservoirs pages 339-365.

Elliott, D. 1976. The energy balance and deformation mechanisms of thrust sheets. Phil. Trans. R. Soc. Lond. vol. A283 pages 289-312.

Engelder, J.T. 1974. Cataclasis and the generation of fault gouge. Geol. Soc. Amer. Bull. vol. 85 pages 1515-1522.

Flournoy, L.A., and Ferrell, R.E., 1980. Geopressure and diagenetic modifications of porosity in the Lirette field area, Terrebonne Parish, Louisiana: Gulf Coast Geological Association Transactions, v. 30, p. 341-345.

Forster, C. and L. Smith 1988. Groundwater flow systems in mountainous terrain, 2. Controlling factors. Water Resour. Res. vol. 24 pages 1011-1023.

Forster, Craig B. and James P. Evans 1991. Hydrogeology of Thrust Faults and Crystalline Thrust Sheets: Results of Combined Field and Modeling Studies. Geophysical Research Letters vol. 18 :5 pages 979 - 982.

Fowles, J. and S. Burley 1994. Textural and permeability characteristics of faulted, high porosity sandstones. Marine and Petroleum Geol. vol. 11 :5 pages 608-623.

Ganser, D.R. 1987. Hydrogeologic characteristics of the Ramapo fault, northern New Jersey. Ground Water vol. 25 pages 664-671.

Gauthier, B.D. and S.D. Lake 1993. Probabilistic modeling of faults below the limit of seismic resolution in Pelican Field, North Sea, offshore United Kingdom. Am. Assoc. Petr. Geol. Bull. vol. 77 pages 761-777.

Ge, S. and G. Garven 1994. A theoretical model for thrust-induced deep groundwater expulsion with application to the Canadian Rocky Mountains. J. Geophys. Res. vol. 99 pages 13,851-13,868.

Gibson, R.G. 1994. Fault-zone seals in siliciclastic strata of the Columbus Basin, offshore Trinidad. Am. Assoc. Petr. Geol. Bull. vol. 78 :9 pages 1372-1385.

Gillespie, P., C. Howard, J. Walsh, and J. Watterson 1993. Measurement and characterization of spatial distributions of fractures. Tectonophysics vol. 226 pages 113-141.

Goggin, D.J. M.A. Chandler, G. Kocurek, and L.W. Lake 1988. Patterns of permeability in eolian deposits: Page Sandstone (Jurassic), northeastern Arizona. SPE Formation Eval. vol. 3 pages 297-306.

Goggin, D.J., R. Thrasher and L.W. Lake 1988. A theoretical and experimental analysis of minipermeameter response including gas slippage and high velocity flow effects. In Situ vol. 12 pages 79-116.

Haneberg, W. 1995. Steady state groundwater flow across idealized faults. Water Resour. Res. vol. 31 :7 pages 1815-1820.

Hawley, J. 1978. Guidebook to Rio Grande rift in New Mexico and Colorado. NM Bur. Mines Miner. Resour. Circular 163. Hawley, J., ed.

Harding, T. P., and Tuminas, A. C., 1988. Interpretation of footwall (lowside) fault traps sealed by reverse faults and convergent wrench faults: AAPG Bull., v. 72, p. 738-757.

Hawley, John and C.Stephen Haase, 1992. Hydrogeologic framework of the northern Albuquerque Basin. Open-File Report 387 NMBMMR.

Heynekamp, M.R., Goodwin, L.B., and Mozley, P.S., 1995. Structural and lithologic controls on patterns of cementation along a Cenozoic normal fault [abstract]: GSA Abstracts with Programs, v. 27, no. 6, p. A-218.

Huntoon, P. 1981. Fault controlled ground-water circulation under the Colorado River, Marble Canyon, Arizona. Ground Water vol. 19 :1 pages 20-27.

Huntoon, P. 1985. Fault severed aquifers along the perimeters of Wyoming artesian basins. Ground Water vol. 23 :2 pages 176-181.

Huntoon, P. and D. Lundy 1979. Fracture-controlled ground-water circulation and well siting in the vicinity of Laramie, Wyoming. Ground Water vol. 17 pages 463-469.

Isaaks, E. and R. Srivastava 1988. Spatial continuity measures for probabilistic and deterministic geostatistics. Math. Geol. vol. 20 :4 pages 313-341.

Kelley, Vincent 1977. Geology of Albuquerque Basin, New Mexico. NM Bur. Mines Miner. Resour. Memoir 33, Socorro, NM

Knipe, R.J., 1992. Faulting processes and fault seal. Structural and Tectonic Modeling and its Application to Petroleum Geology. pages 325-342.

Knipe, R.J. 1993. The Influence of Fault Zone Processes and Diagenesis On Fluid Flow. Diagenesis and Basin Development AAPG Studies in Geology #36 :36 pages 135-151.

Kocurek, G. and R. Dott. 1983. Jurassic paleogeography and paleoclimate of the central and southern Rocky Mountain region, in Mesozoic Paleogeography of the West-Central United States, M. Reynolds and E. Dolly, eds., published by the Rocky Mountain Section of the SEPM, Denver, CO, pp. 101-131.

Kolm, K. and J. Downey 1994. Diverse flow patterns in the aquifers of the Amargosa Desert and vicinity, southern Nevada and California. Bull. Assoc. eng. Geol. vol. 31 pages 33-47.

Krantz, R.W. 1988. Multiple fault sets and three-dimensional strain: theory and applicaiton. Jour Struct Geol vol. 10 pages 225-237.

Lewis, C.J. and W.S. Baldridge 1994. Crustal Extension in the Rio Grande Rift, New Mexico: Half-Grabens, Accommodation Zones, and Shoulder Uplifts in the Ladron Peak-Sierra Lucero Area. Basins of the Rio Grande Rift: Structure, Stratigraphy, and Tectonic Setting vol. Special Paper 291 pages 135-156.

Liu, K., P. Boult, S. Painter, and L. Paterson. 1996. Outcrop analog for sandy braided stream reservoirs: permeability patterns in the Triassic Hawkesbury Sandstone, Sydney Basin, Australia. AAPG BUll. v. 80, no. 12, pages 1850-1866.

Lozinsky, R.P. 1994. Cenozoic Stratigraphy, Sandstone Petrology, and Depositional History of the Albuquerque Basin, Central New Mexico. Basins of the Rio Grande Rift: Structure, Stratigraphy, and Tectonic Setting vol. Special Paper 291 pages 73-82.

Machette, M. 1978. Dating Quaternary faults in the southwestern United States by using buried calcic paleosols. Jour. Research U.S. Geol. Survey vol. 6 :3 pages 369-381.

Machette, M. 1986. History of Quaternary offset and paleoseismicity along the La Jencia fault, central Rio Grande rift, New MExico. Bulletin of Seismological Soc of Am vol. 76 :1 pages 259-272.

Machette, M.N., S.F. Personius and A.R. Nelson 1991. Paleoseismology of the Wasatch Fault Zone: A summary of recent investigations, interpretations, and conclusions - Assessment of regional earthquake hazards and risk along the Wasatch Front, Utah. USGS Professsional Paper 1500-A

Machette, M.N., S.F. Personius, A.R. Nelson, D. P. Schwartz, and W. R. Lund 1991. The Wasatch fault zone, Utah - segmentation and history of Holocence earthquakes. J. Structural Geol. vol. 13 :2 pages 137-149.

Machette, M. 1982. Quaternary and Pliocene faults in the La Jencia and southern part of the Albuquerque - Belen Basins, New Mexico: Evidence of fault history from fault-scarp morphology and Quaternary geology. New Mexico Geological Society Guidebook - Albuquerque Country II vol. 33rd field conference pages 161-169.

Maclay, R. and T. Small 1993. Hydrostratigraphic subdivisions and fault barriers of the Edwards aquifer, south-central Texas, USA. J. Hydrol. vol. 61 pages 127-146.

Mandelbrot, B.B. 1983. The Fractal Geometry of Nature. W.H. Freeman and Co., New York.

Marrett, R. and R.W. Allmendinger 1991. Short Note - Estimates of strain due to brittle faulting: sampling of fault populations. Jour Struct Geol vol. 13 :6 pages 735-738.

Matlack, K.S., Houseknecht, D.W., and Applin, K.R., 1989. Emplacement of clay into sand by infiltration: Jour. Sed. Petrology, v. 59, p. 77-87.

Matthai, S.K. and S.G. Roberts. 1996. The influence of fault permeability on single-phase fluid flow near fault-sand intersections: results from steady-state high resolution models of pressure-driven fluid flow. Am. Assoc. Petr. Geol. Bull. v. 80 (11), pages 1763-1779.

May, S.J. and L.R. Russell 1994. Thickness of the Syn-Rift Santa Fe Group in the Albuquerque Basin and its Relation to Structural Style. Basins of the Rio Grande Rift: Structure, Stratigraphy, and Tectonic Setting vol. Special Paper 291 pages 113-124.

Moraes, M., and L. De Ros. 1990. Infiltrated clays in fluvial Jurassic sandstones of Reconcavo Basin, Northeastern Brazil. Jour. Sed. Petrol. v. 60, no. 6, pages 809-819.

Morrow, C., L. Shi, and J. Byerlee. 1981. Permeability and strength of San Andreas fault gouge under high pressure. Geophys. Res. Letters vol. 8, no. 4, pages 325-328.

Morrow, C., L. Shi, and J. Byerlee. 1984. Permeability of fault gouge under confining pressure and shear stress. Jour. Geophys. Res. v. 89, no. B5, pages 3192-3200.

Mozley, P. and L. Goodwin 1994. Patterns of cementation along the Sand Hill Fault, Albuquerque Basin, NM; implications for paleoflow orientations and mechanisms of fault-related cementation. Characterization of Hydrogeologic Units in the Northern Albuquerque Basin, Open-file report

Muraoka, H. and H. Kamata 1983. Displacement distribution along minor fault traces. J. Struct. Geol. vol. 5 pages 483-495.

Nicol, A., J. Walsh, J. Watterson, and P. Gillespie 1996. Fault size distributions - are they really power-law?. J. Struct. Geol. vol. 18 :2/3 pages 191-197.

Pannatier, Y. 1994. MS-WINDOWS Programs for Exploratory Variography and Variogram Modeling in 2D. In Statistics of Spatial Processes: Theory and Applications. Bari, Italy, September 27-30, 1993. V. Capasso, G. Girone, and D. Posa, eds., pages 165-170.

Peacock, D.C. 1991. Displacement and segment linkage in strike-slip fault zones. J. Struct. Geol. vol. 13 pages 1025-1035.

Pittman, E.D. 1981. Effect of fault-related granulation on porosity and permeability of quartz sandstones, Simpson Group (Ordovician), Oklahoma. Am. Assoc. Petr. Geol. Bull. vol. 65 :11 pages 2381-2387.

Rose, W. 1983. A note on the role played by sediment bedding in causing permeability anisotropy. J. Petroleum Tech. vol. Feb., 1983 pages 330-332.

Russell L.R and S. Snelson 1994. Structure and Tectonics of the Albuquerque Basin Segment of the Rio Grande Rift: Insights from Reflection Seismic Data. Basins of the Rio Grande Rift: Structure, Stratigraphy, and Tectonic Setting vol. Special Paper 291 pages 83-112.

Russell, L.R. and S. Snelson 1990. Structural style and tectonic evolution of the Albuquerque Basin segment of the Rio Grande rift. The Potential of Deep Seismic Profiling for Hydrocarbon Exploration: Institut Francais Petrole Research Conference Proceedings pages 175-207.

Schlische, R., S. Young, R. Ackerman, and A. Gupta 1996. Geometry and scaling relations of a population of very small rift-related normal faults. Geology vol. 24 :8 pages 683-686.

Scholz, C.H. and M.H. Anders, 1994. The permeability of faults. The Mechanical Involvement of Fluids in Faulting, USGS Open-file Report 94-228 pages 18-30.

Segall, P. and D. Pollard 1983. Nucleation and growth of strike-slip faults in granite. J. Geophys. Res. vol. 88 pages 555-568.

Shan, C., I. Javandel, and P.A. Witherspoon, 1995. Characterization of leaky faults: Study of water flow in aquifer-fault-aquifer systems. Water Resour. Res. vol. 31, no. 12, pp 2897-2904.

Smith, D.A. 1966. Theoretical considerations of sealing and non-sealing faults. Am. Assoc. Petr. Geol. Bull. vol. 50 pages 363-374.

Smith, D.A. 1980. Sealing and non-sealing faults in Lousiana Gulf Coast salt basin. Am. Assoc. Petr. Geol. Bull. vol. 64 pages 145-172.

Smith, L., C. Forster and J. Evans 1989. Interaction of Fault Zones, Fluid Flow, and Heat Transfer at the Basin Scale. in Hydrogeology of Low Permeability Environments vol. 2 pages 41 - 67.

Thorn, C., D. McAda, and J. Kernodle 1993. Geohydrologic framework and hydrologic conditions in the Albuquerque Basin, central New Mexico. U.S. Geol. Surv. Water Resour. Invest. Rep. 93-4149 pages 106 pp.

Tidwell, V.C. and J.L. Wilson. 1997. Laboratory method for investigating permeability upscaling. Water Resour. Res. v. 33 (7), pages 1607-1616.

Titus, F.B. Jr. 1963. Geology and ground-water conditions in eastern Valencia County, New Mexico. N.M. Bur. Mines MIner. Resour. Ground Water Rep. 7 pages 113 pp.

Tolman, C.F. 1937. Ground Water. McGraw-Hill, New York.

Twiss, R.J. and E.M. Moores 1992. Structural Geology. Freeman, New York.

Walsh, J.J and Watterson, J. 1988. Analysis of the relationship between displacements and dimensions of faults. J. Struct. Geol. vol. 10 pages 239-247.

Walsh, J.J. and J. Watterson 1991. Geometric and kinematic coherence and scale effects in normal faults . Geometry of Normal Faults vol. Spec. Publs geol. Soc. Lond. :56 pages 193-206.

Weber, K., G. Mandl, W. Pilaar, and R. Precious 1978. The role of faults in hydrocarbon migration and trapping in Nigerian growth fault structures. Offshore Technology Conference Proceedings pages 2643-2653.

Whitworth, T.M., Haneberg, W.C., DeRosa, G., Romero, D., Mozley, P.S., and Goodwin, L.B., 1996, Solute sieving by pulverized quartzofeldspathic sands-- experimental results and implications for the membrane behavior of fault gouge [abstract]: GSA 1996 Annual Meeting Abstracts with Programs.

Wingle, W.L., Poeter, E.P., and McKenna, S.A. 1994. UNCERT User s Guide. Colorado School of Mines, Golden, CO 80401.

APPENDICES

Appendix I: Study Site Location Maps

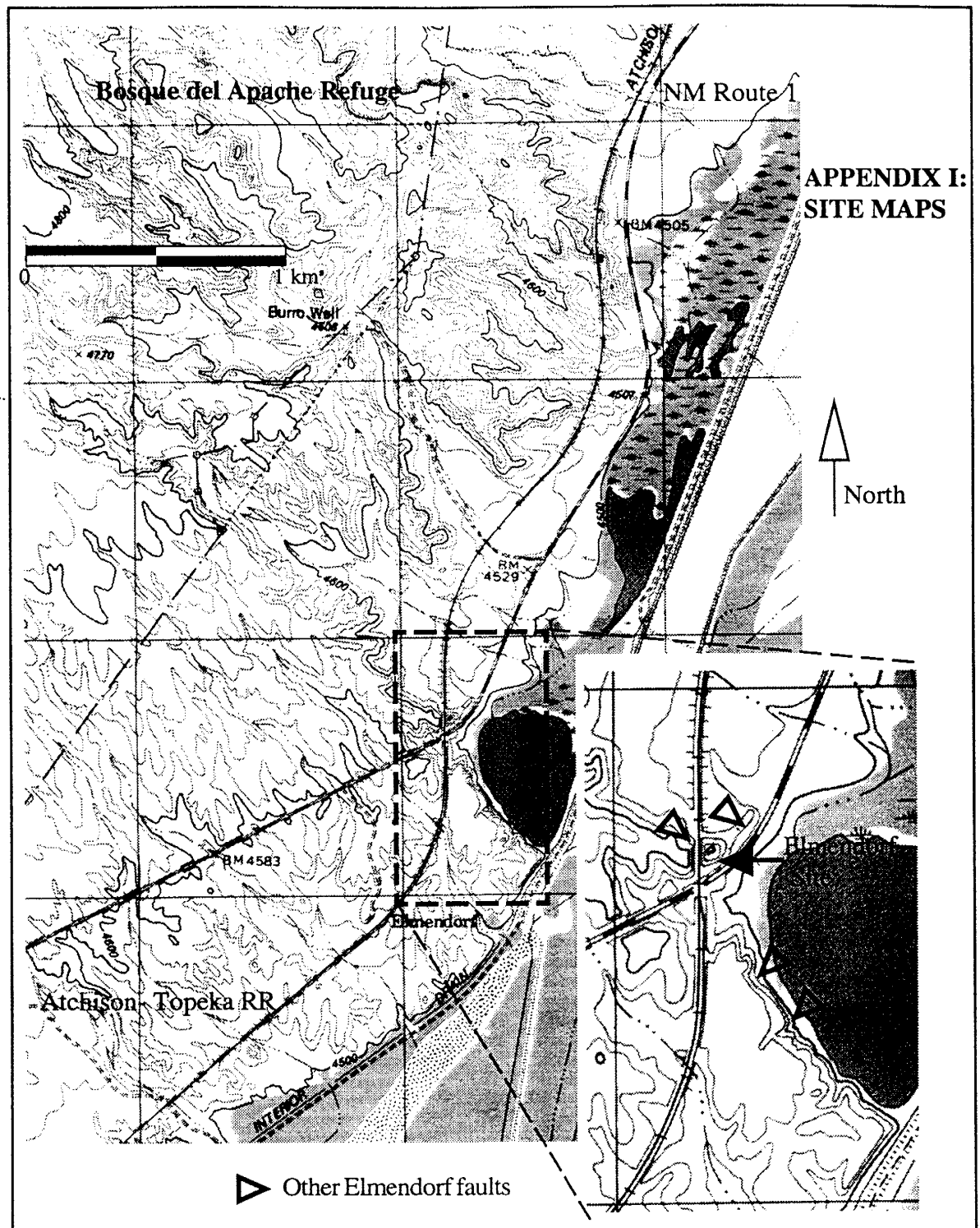

Figure 22: Elmendorf Site Map. Based on USGS (1981) Indian Well Wilderness, New Mexico Topographic Quadrangle (1:24,000). Contour interval is 20 ft. The site is 8 km (5 mi) south of the Bosque del Apache Visitor's Center and approximately 22 km (13 mi) south of the village of San Antonio, NM.

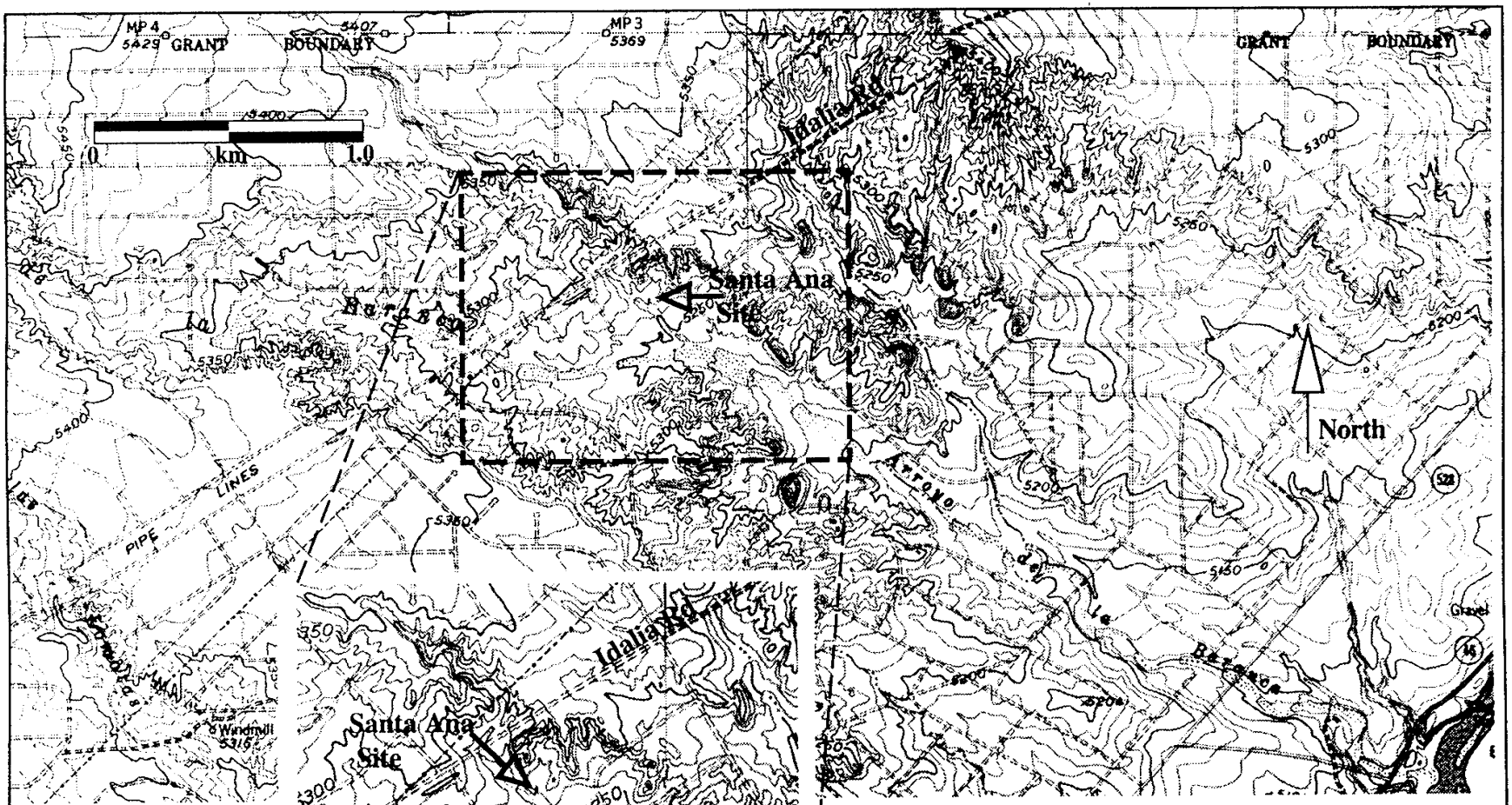

APPENDIX I:
SITE MAPS

Figure 23:
Santa Ana Site Map.

Based on USGS (1981) Loma Machette, New Mexico Topographic Quadrangle (1:24,000). Contour interval is 20 ft. The site is in an arroyo just south of Idalia Road, 5 km (3 mi) from the intersection of Idalia Rd and NM Route 528.

Appendix II: Variography of Permeability in Faulted, Poorly Consolidated Sands

Methods for Determining Spatial Variability of Permeability

Spatial correlation of permeability was quantified through calculation of sample semi-variograms for the mean permeability logarithms (second treatment). Variogram estimates were tested for sensitivity to data clustering and extreme values (outliers) by computing more robust measures such as the semi-rodogram and general relative semi-variogram (Deutsch and Journel, 1992). Where possible, values for the range, sill, and nugget variance were determined by fitting theoretical semi-variogram models to the experimental semi-variograms.

Sample semi-variograms (Equation 3) were calculated separately for undeformed and deformed zones for the isotropic (omni-directional) case and for a range of anisotropic geometric directions between azimuths of 0 and 170 degrees measured clockwise from a 0 degree upwards vertical direction. The azimuthal plane refers to the plane of the outcrop face. All variographic calculations were carried out using the VARIO module of the public domain software package UNCERT (Wingle et al., 1994), available from the Colorado School of Mines in Golden, CO, the GSLIB GAM2V

Equation 3: Definition of Sample Semi-Variogram (Deutsch and Journel, 1992)

$$\lambda(\mathbf{h}) = \frac{1}{2N(\mathbf{h})} \sum_{i=1}^{N(\mathbf{h})} \left(x_i - y_i\right)^2$$

with N(**h**) as the number of pairs for lag class **h** and x and y as the head and tail values for each pair *i*.

subroutine (Deutsch and Journel, 1992), and the VARIOWIN package (Pannatier, 1994).

Lag spacing was initially set to match the minimum spacing between mini-permeameter measurements. The maximum search distance, directional bandwidth, and horizontal half-angle

parameters were set to the maximum values appropriate for each zone at each site for the isotropic sample semi-variogram. These parameters were reduced to values appropriate for anisotropic sample semi-variograms.

Examination of experimental semi-variograms for periodicity, noise, and anisotropy focused on the lag classes with sufficient numbers of pairs. Theoretical semi-variogram model parameters (range, sill, and nugget variance) were estimated for selected sample semi-variograms by eye or, where possible, using UNCERT's VARIOFIT module or VARIOWIN.

Clustering of the data locations as well as outliers can create an apparent correlation structure in sample semi-variograms entirely unrelated to the true spatial correlation (Deutsch and Journel, 1992; Isaaks and Srivastava, 1989, p. 162). Robustness of permeability sample semi-variograms to clustering and outliers was tested using measures of spatial continuity which are less sensitive to data clustering. The semi-rodogram and general and pairwise relative semi-variograms are typically less vulnerable to clustering because they normalize the semi-variogram value for each lag class by the squared mean of the data and the squared average of the paired values (Journel, 1984; Isaaks and Srivastava, 1988). Equation 4 defines the semi-rodogram and Equation 5 defines the general relative semi-variogram. Sample semi-rodograms and general relative semi-variograms were calculated for isotropic and selected directions within each zone at the two sites. Non-ergodic covariances (Equation 6) and correlograms (Equation 7) were used to evaluate whether variations in lag class means and variances unduly influenced correlation structures displayed in the experimental semi-variograms (see Deutsch and Journel, 1992, page 56).

Equation 4: Definition of Semi-Rodogram (Deutsch and Journel, 1992)

$$\lambda_R(\mathbf{h}) = \frac{1}{2N(\mathbf{h})} \sum_{i=1}^{N(\mathbf{h})} \sqrt{|x_i - y_i|}$$

with N(**h**) as the number of pairs for lag class **h** and x and y as the head and tail values for each pair *i*.

Equation 5: Definition of General Relative Semi-Variogram (Deutsch and Journel, 1992)

$$\lambda_{GR}(\mathbf{h}) = \frac{1}{2N(\mathbf{h})} \sum_{i=1}^{N(\mathbf{h})} (x_i - y_i)^2 \left(\frac{m_{-\mathbf{h}} + m_{+\mathbf{h}}}{2} \right)^{-2}$$

where $m_{-\mathbf{h}}$ is the mean of the head (x) values and $m_{+\mathbf{h}}$ is the mean of the tail (y) values for lag class **h**.

Equation 6: Definition of Non-Ergodic Covariance (Deutsch and Journel, 1992)

$$C(\mathbf{h}) = \frac{1}{N(\mathbf{h})} \sum_{i=1}^{N(\mathbf{h})} x_i y_i - m_{-\mathbf{h}} m_{+\mathbf{h}}$$

Equation 7: Definition of Correlogram (Deutsch and Journel, 1992)

$$\rho(\mathbf{h}) = \frac{1}{N(\mathbf{h})} \frac{\sum_{i=1}^{N(\mathbf{h})} x_i y_i - m_{-\mathbf{h}} m_{+\mathbf{h}}}{\sigma_{-\mathbf{h}} \sigma_{+\mathbf{h}}}$$

where $\sigma_{-\mathbf{h}}$ is the standard deviation of the head (x) values and $\sigma_{+\mathbf{h}}$ is the standard deviation of the tail (y) values within each lag group **h**.

Spatial Variability Results

Variographic analysis revealed little spatial correlation structure within undeformed-zone permeability for both undeformed zones. The Elmendorf undeformed-zone log permeability shows evidence of geometric anisotropy and short-scale ranges (correlation lengths) whereas the Santa Ana undeformed-zone permeability does not appear to have any spatial correlation structure at the decimeter to meter scale. Too few measurements were collected within the Elmendorf fault zone to permit geostatistical analysis. Santa Ana fault-zone log permeability displays evidence of non-

stationarity, perhaps caused by local changes in mean permeability with associated with the buff, red, and cataclasite zones.

The relatively sparse sampling grid in the Elmendorf undeformed zone (Figure 24) yielded a sufficient number of measurement locations (47) to provide evidence of anisotropy and short correlation lengths (10 - 20 cm) in experimental semi-variograms for permeability logarithms (Figure 25) (See Appendix III for graphs of all measures of spatial variability).

The isotropic and directional variograms between azimuths 60 and 120 degrees (azimuth 0 points vertically upwards with azimuth angles increasing in a clockwise direction) are the only sample variograms with sufficient numbers of pairs to reliably discern any spatial correlation structure. Perhaps coincidentally, fault dip is perpendicular to an azimuth of 110 to 120 degrees. No bedding dip or strike measurements were made. Even with sufficient numbers of lag class pairs, the isotropic and directional variograms between azimuths 60 and 120 degrees display considerable noise and suggest two possible interpretations (Figure 25). One interpretation is that the sample variograms define a noisy transition model with a short range value of roughly 0.30 m; the second interpretation consists of three nested transition models with ranges (as estimated by eye) of roughly 0.3, 0.6, and 1.0 m. A zero lag sample semivariogram value, calculated by using all 1284 replicate measurements (i.e., combining the three or more replicate measurements per sampling location for all locations) as input to the GSLIB GAM2V semivariogram subroutine (Deutsch and Journel, 1992) with the lag value set to zero, offers an estimate of measurement error because it estimates the nugget variance. The sample zero lag semivariogram value for all replicates accounted for roughly 10% of the log permeability zonal variance (sill) of 0.012.

FIGURE 24: Sampling Locations - Elmendorf Site

Open symbols identify single sampling-incident locations for permeability.
Filled symbols (Repeated) identify locations of multiple permeability sampling-incidents.

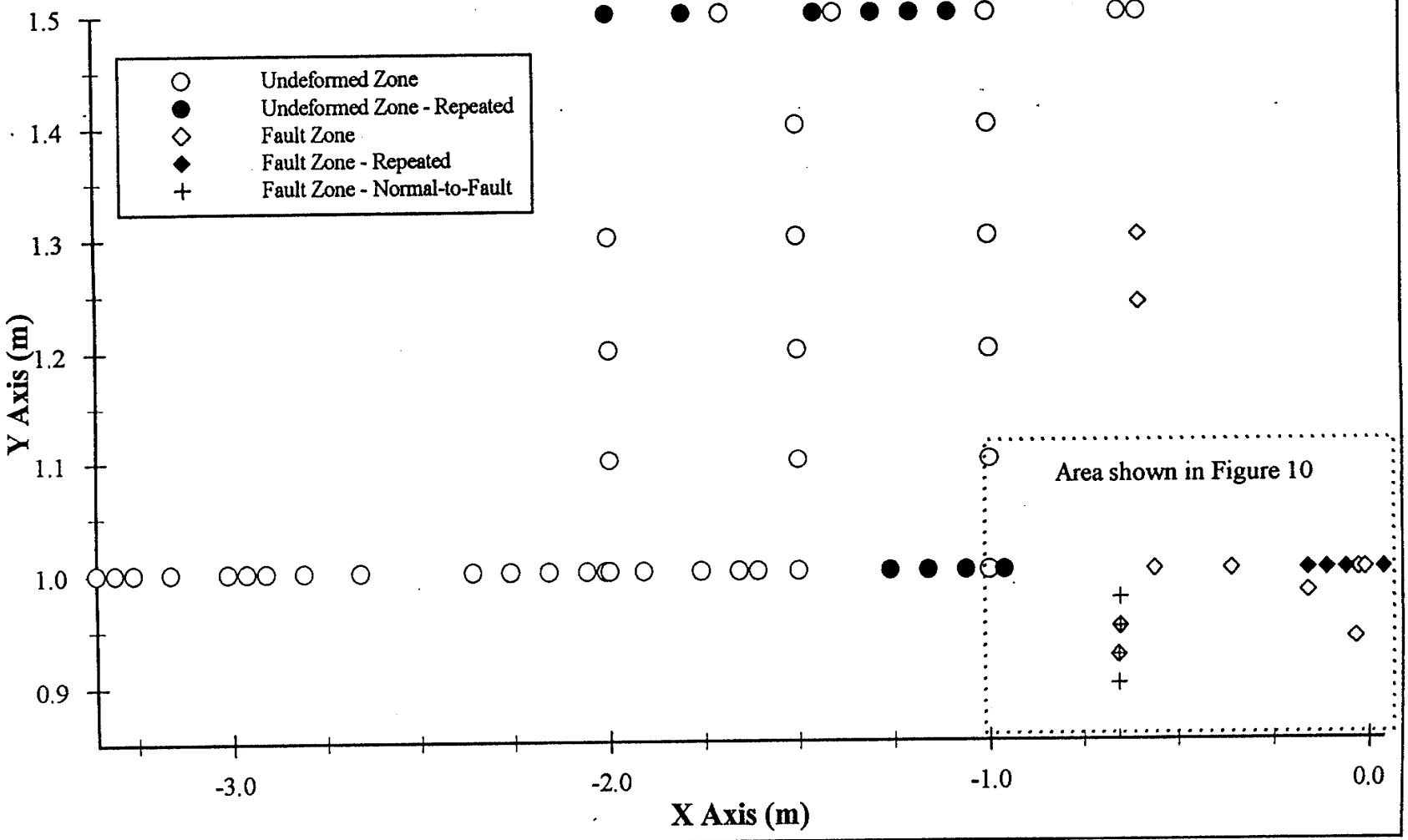

Figure 25: Sample Semi-Variograms of Log Permeability
Elmendorf Undeformed Zone

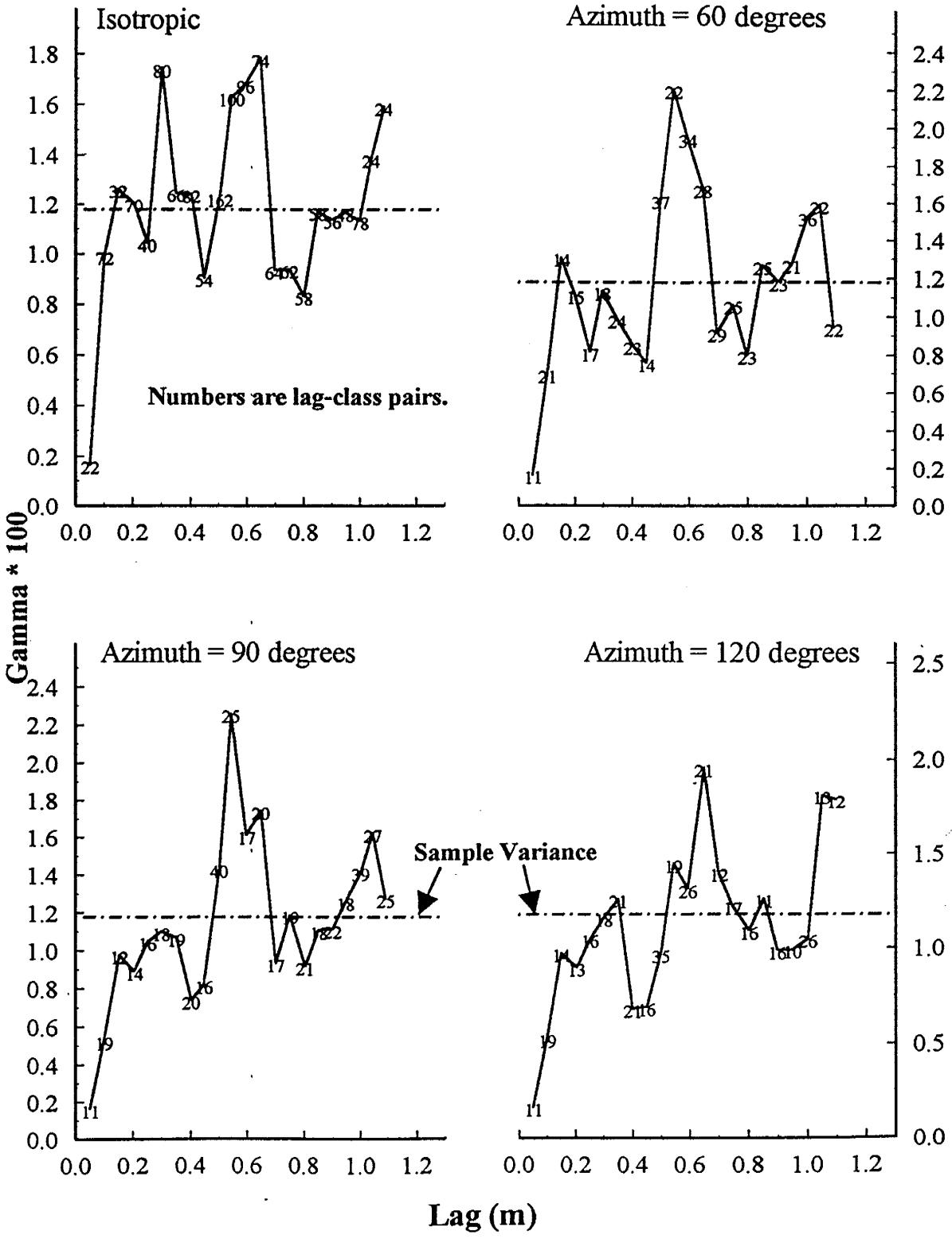

The sharp peaks in the sample variograms may indicate a periodic or nested structure within undeformed sand permeability, possibly an expression of the formation's eolian depositional processes. They may also be artifacts spuriously created by data outliers, clustering of data locations, or by the sampling grid's high aspect ratio. Sample variogram robustness to clustering and outliers was tested by examination of sample semi-rodograms and general relative variograms, which are typically less sensitive to such potentially confounding factors (Isaaks and Srivastava, 1988; Deutsch and Journel, 1992, page 56). The same correlation structures, such as number of peaks and their ranges, are observed to be consistent across all three measures of correlation structure (Figure 26 and Figure 27), making it less likely that the sample variograms are unduly affected by either extreme data values or data clustering.

Containing twice as many measurement locations (96) as its Elmendorf counterpart, the Santa Ana undeformed zone covers nearly four times the area, 4.5 versus 1.3 m^2 (Figure 28). This difference in data density is at least partly responsible for the greater amount of noise and poor evidence of spatial correlation structure displayed in the Santa Ana undeformed zone experimental variograms for mean permeability logarithms (Figure 29). Isotropic variograms computed at lags of 0.08, 0.15, and 0.20 m point to the presence of a large nugget variance, accounting for nearly 80% of total sample variance. The sole directional experimental variograms with discernible correlation structure were calculated at azimuths 130 and 140 degrees, possibly aligned with the tangential cross-beds, and indicate correlation lengths of approximately 0.2, 0.6, and perhaps 1.2 m. This latter scale length, as well as a possible trend observed in the isotropic 0.15 and 0.20 m lag variograms, should probably be discounted according to the geostatistical rule of thumb of confining interpretation to lag classes within the first 25 - 30% of domain length. Alternative measures of spatial correlation also display high noise levels with the nugget variance model giving the best fit: general relative semi-variograms (Figure 30) and semi- rodograms (Figure 31). The zero lag class

Figure 26: Sample Semi-Rodograms
Elmendorf Undeformed Zone

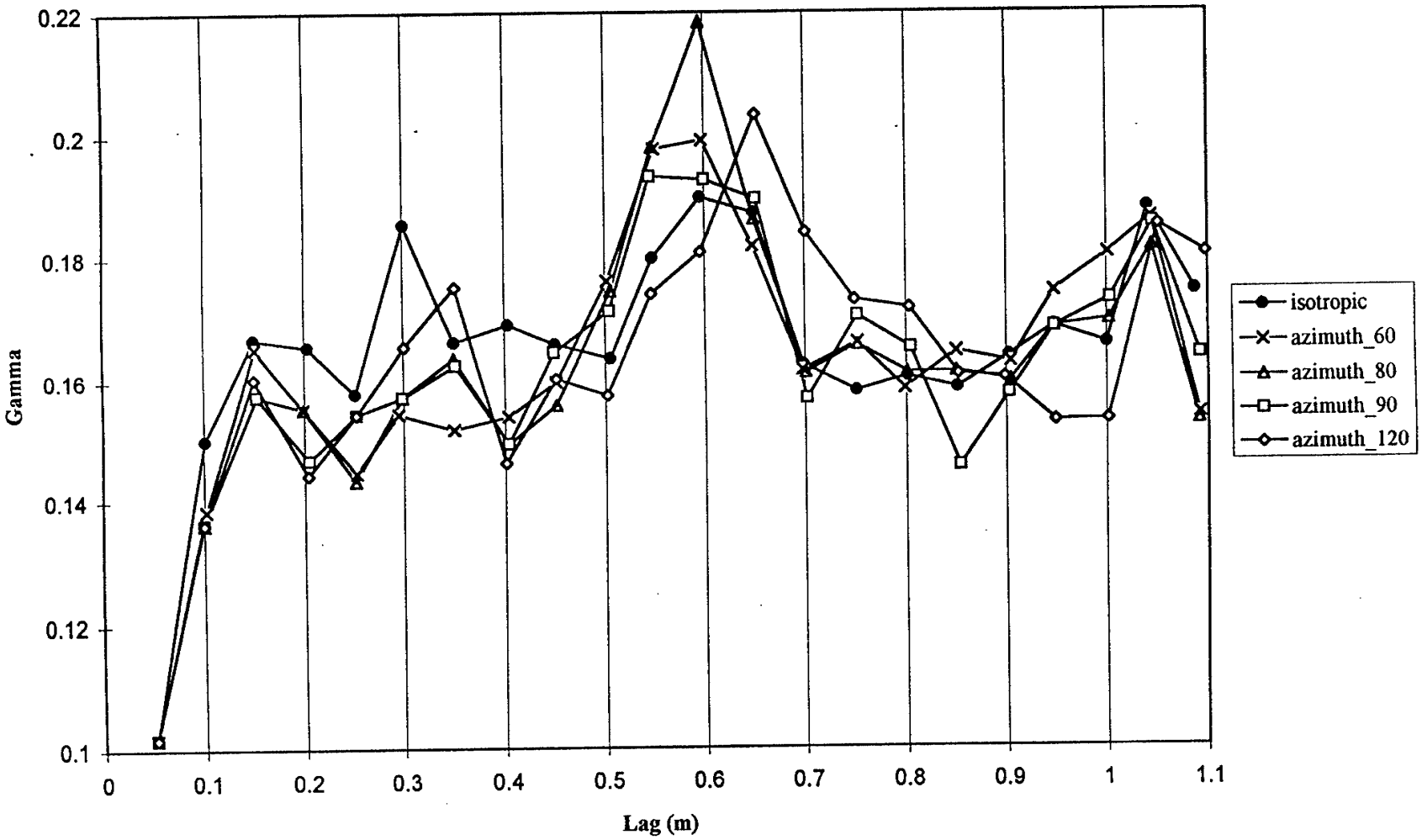

Figure 27: Sample General Relative Semi-Variograms
Elmendorf Undeformed Zone

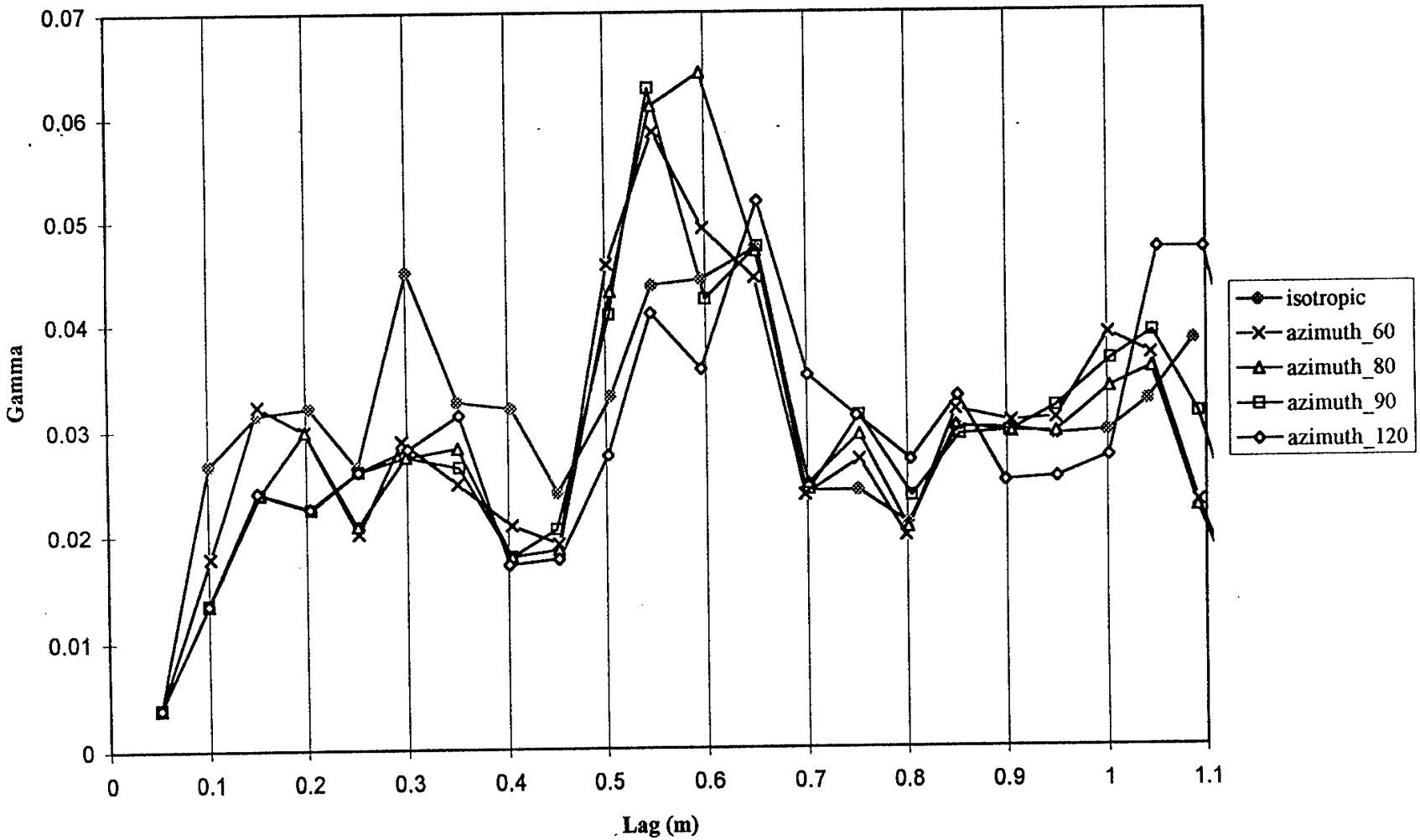

FIGURE 28: Sampling Locations - Santa Ana Site

Open symbols identify single sampling-incident locations for permeability.
Filled symbols (Repeated) identify locations of multiple permeability sampling-incidents.

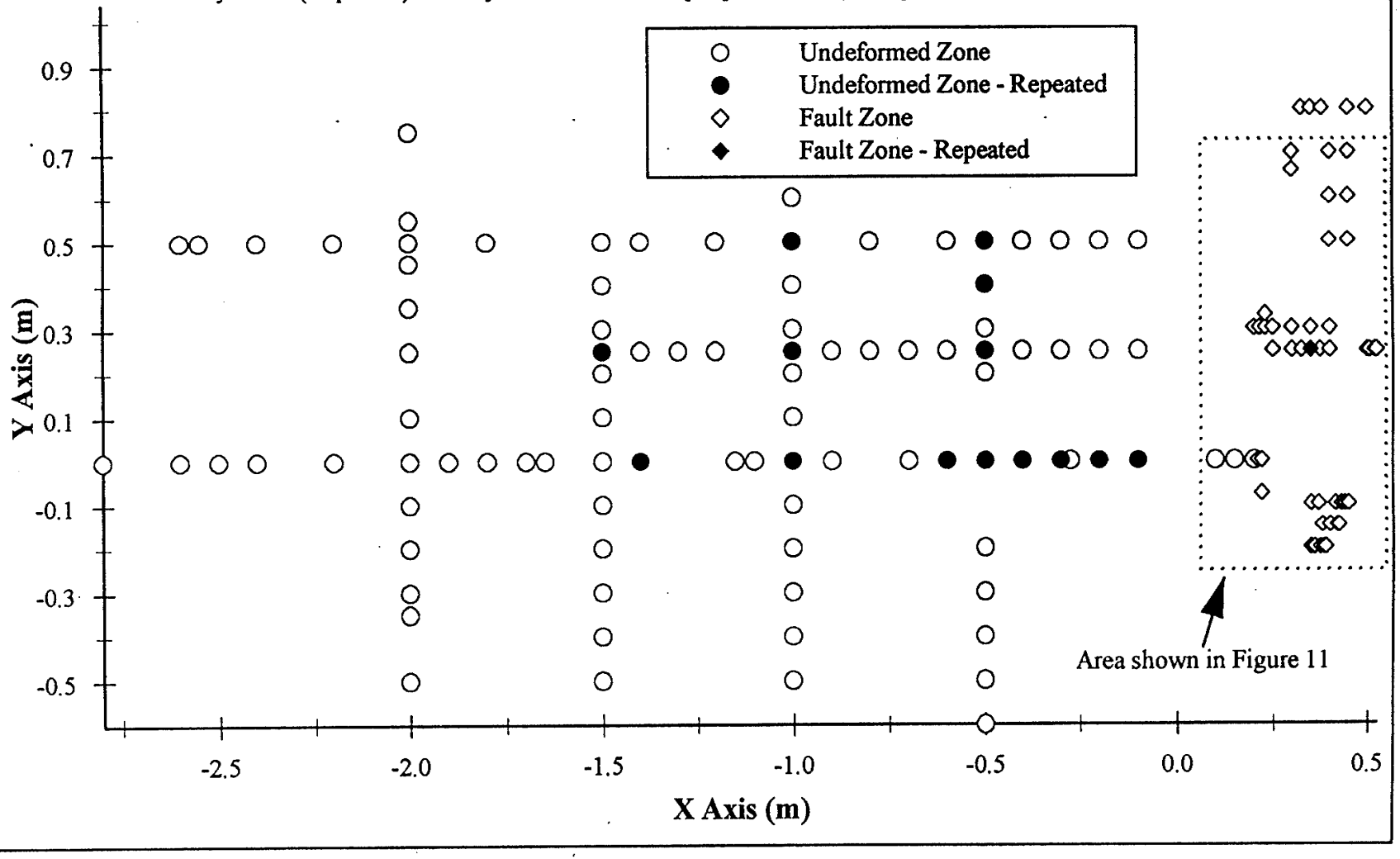

Figure 29: Sample Semi-Variograms of Log Permeability

Santa Ana Undeformed Zone

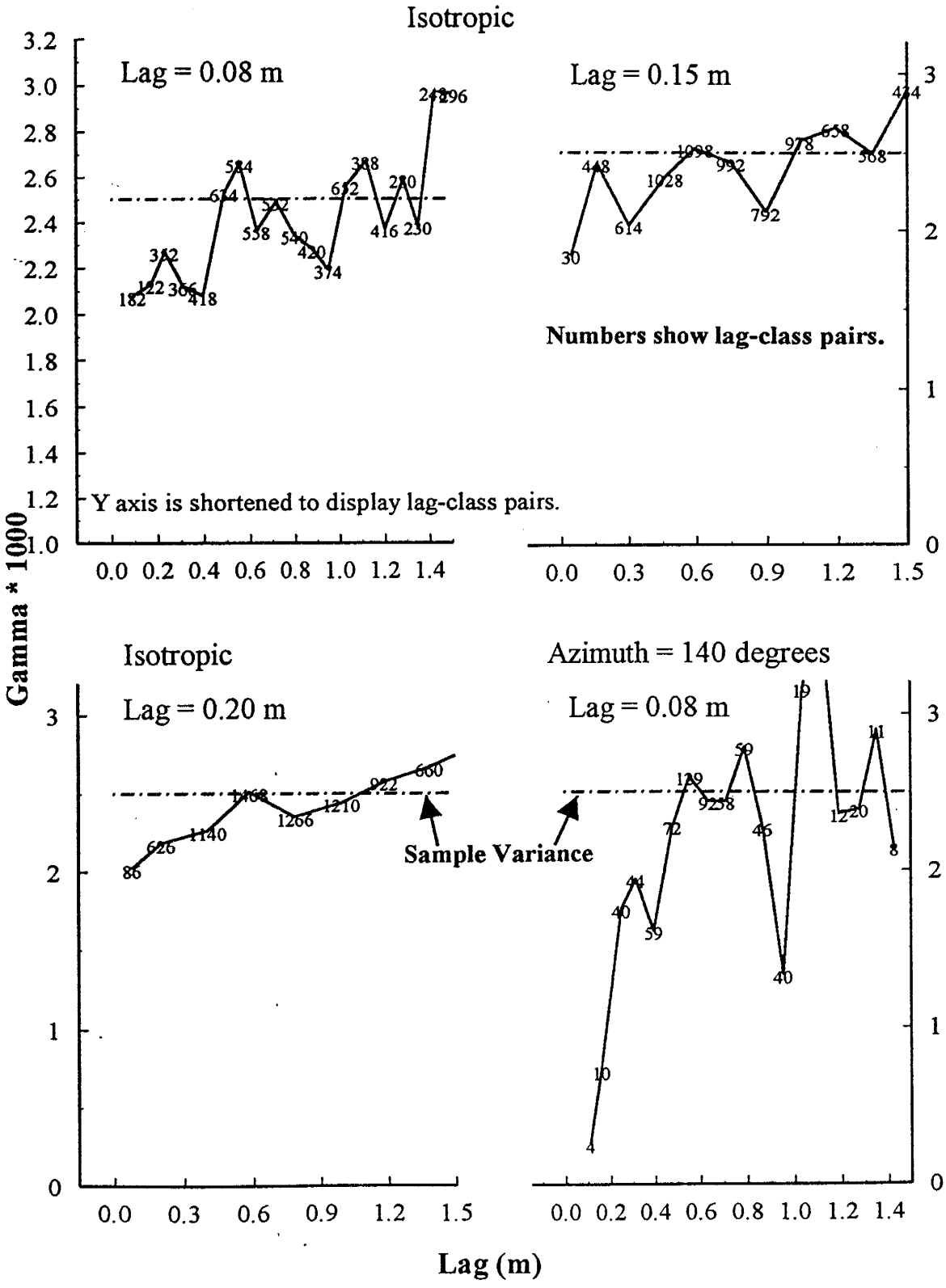

Figure 30: Sample General Relative Semi-Variograms

Santa Ana Undeformed Zone

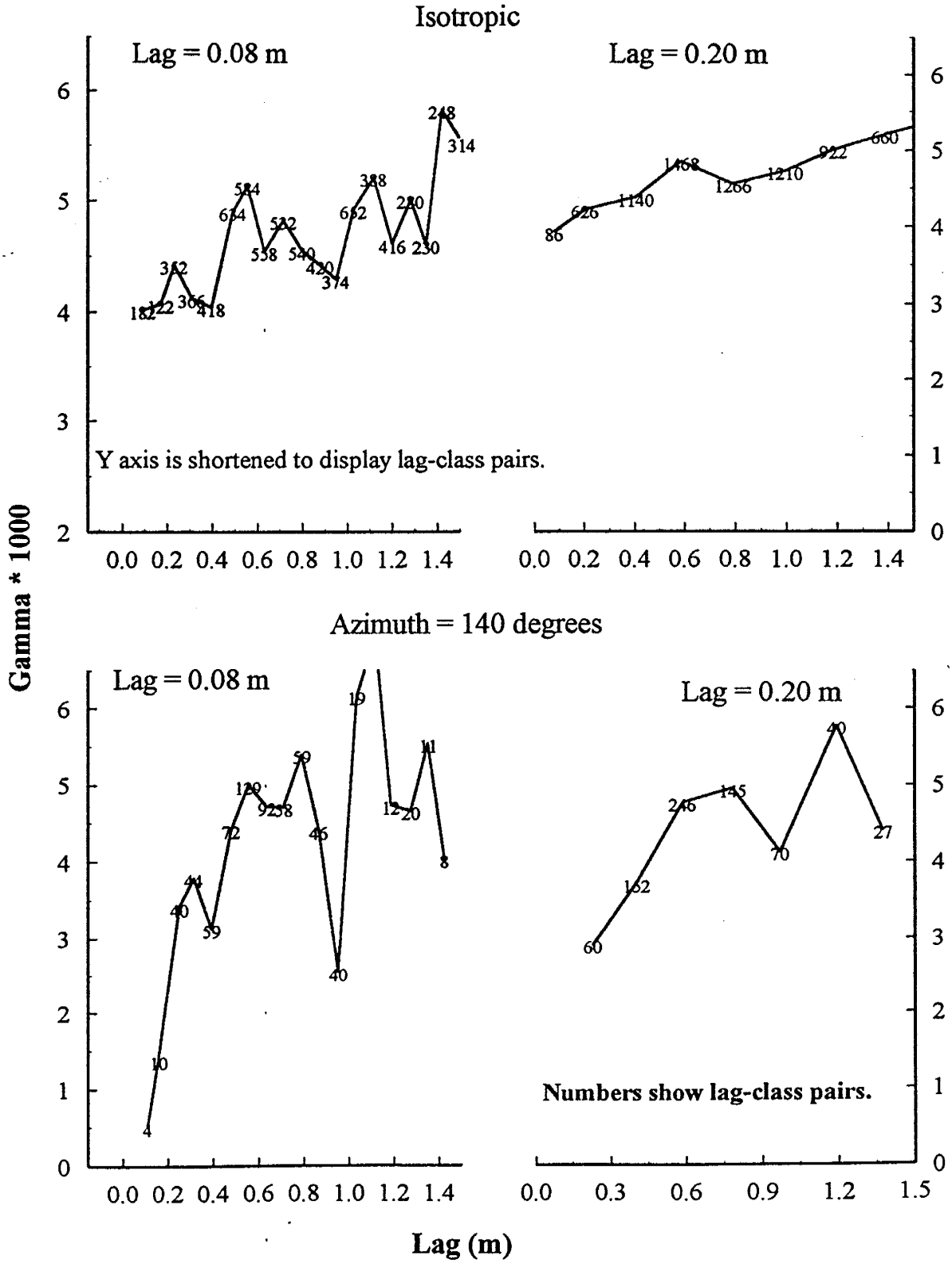

Figure 31: Sample Semi-Rodograms of Log Permeability

Santa Ana Undeformed Zone

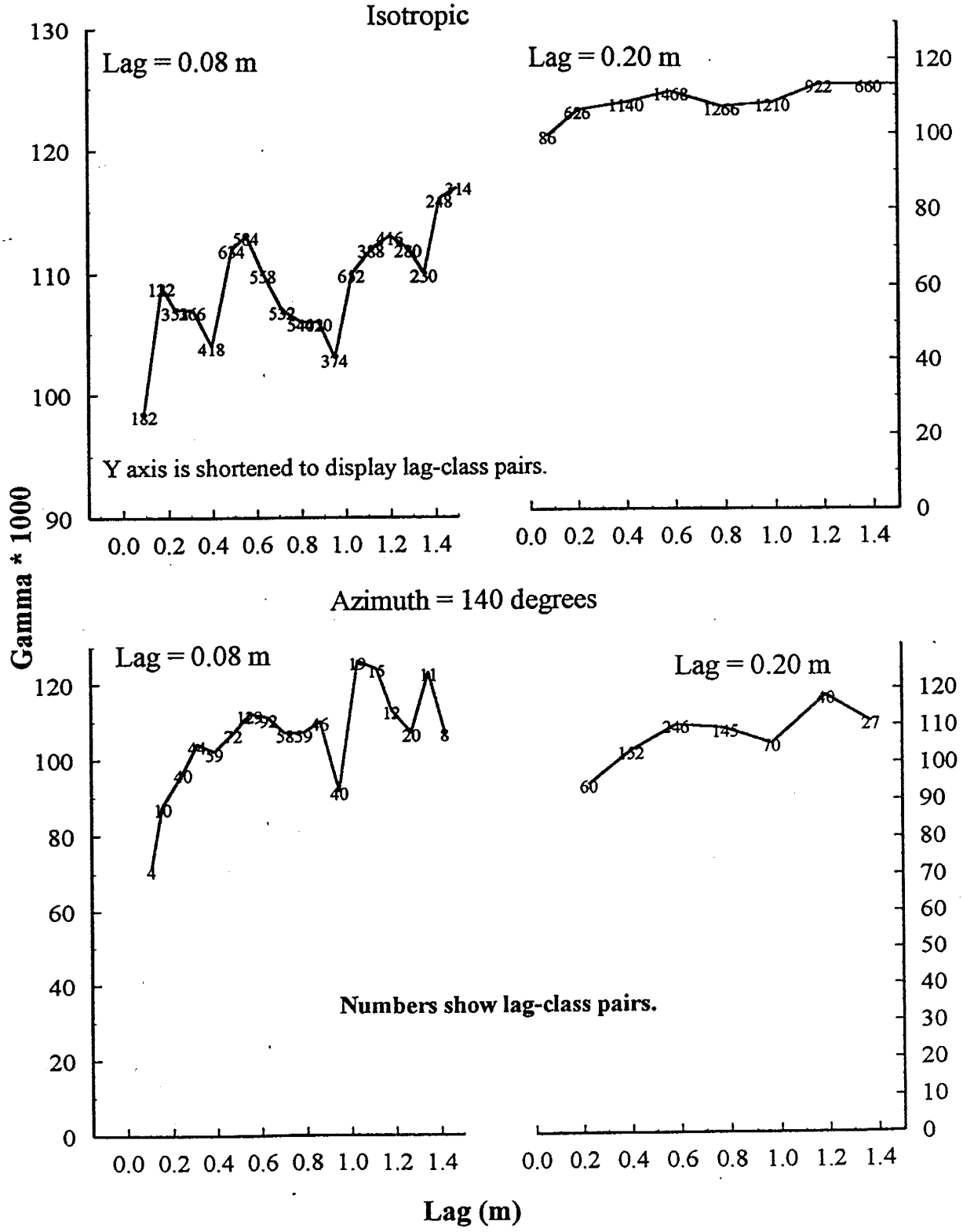

Figure 32: Sample Semi-Variograms of Log Permeability

Santa Ana Fault Zone

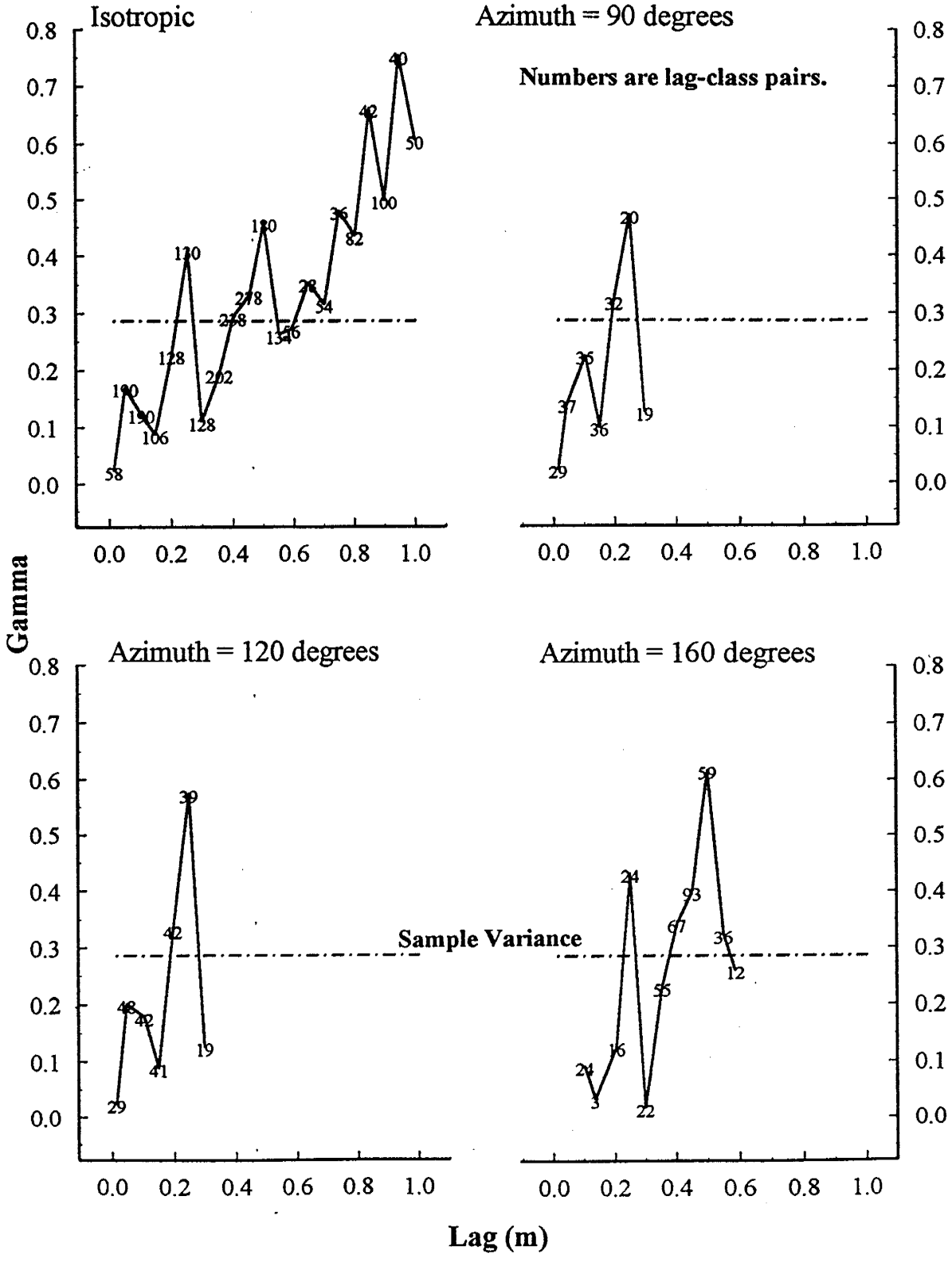

variogram value for all replicate measurements was 0.00036, which represents roughly 10% of the total sample variance (sill) and suggests measurement error is only a small fraction of the total sample variance for the undeformed zone.

Although numbers of measurements within the fault zone (Figure 28) were sufficient to calculate both isotropic and anisotropic experimental semi-variograms at lags of 0.05 m, the results are very noisy and show a quadratic-rate rise characteristic of a trending mean (Figure 32). The experimental directional semi-variograms within 20 degrees of vertical (azimuths 20 and 160 degrees) and the isotropic case give hints of nested correlation structures or periodicity.

The significant dissimilarities in geostatistical analysis results from the two undeformed zones are most likely attributable to differences in depositional environment or diagenesis since the two zones have very similar mineral compositions and grain-size distributions. *A priori*, one would not expect the massive, structureless (in the sedimentological sense) Santa Ana undeformed buff sand to exhibit strong spatial correlation. Noise in the experimental variograms may be the result of an insufficient number of measurement locations or because the plane of the outcrop face is normal to the buff sand's main correlation structure. Given that the mini-permeameter sampling variances are much less than the experimental semi-variogram values for very short lags (~0.0 m), the large observed nugget variance reflects either the true white-noise nature of the Santa Ana undeformed sands or the presence of an unresolved sub-0.05 m correlation structure. In contrast, the short-scale, predominantly anisotropic, potentially cyclic correlation structures estimated for the Elmendorf undeformed zone provide a reasonable match with the observed eolian cross-beds. The inferred correlation lengths of 0.3 to 0.35, 0.4-0.6, and 1.0 m may directly correlate with packages of different grain sizes and lamina orientation or they may correlate with eolian depositional packages such as wind ripple, grain fall, and grain flow laminae or beds, which have centimeter-scale

permeability variations (Chandler et al., 1989; Goggin, et al. 1989; Goggin, et al. 1988). Davis (1994) reported a nested correlation structure with ranges of 0.15 and 5.3 m in the horizontal direction for the northern face of the Elmendorf outcrop (facing into the railroad cut), but the eolian trough cross-beds there extend 5 to 15 m.

Appendix III: Permeametry Measurements

Elmendorf Site

Undeformed Zone

Fault Zone

Santa Ana Site

Undeformed Zone

Fault Zone

KEY to Data Tables

Date	Sample collection date
X	Local x coordinate for sample
Y	Local y coordinate for sample
Time	measured time (seconds) to displace known volume for syringe air mini-permeameter
k	permeability (darcies) computed from time (SAMP)or from flow rate and pressure (CFMP)
Instr	Instrument: C = Continuous flow mini-permeameter; S = Syringe air mini-permeameter

Description abbreviations:

br	brown
B&W	black and white
c	coarse
db	deformation band
DT	downthrown
f	fine
gr	grained
lam	laminae
loc	location
lt	light
m	medium
med	medium
rt	right
SB	slip band
UT	upthrown

CODE (Santa Ana fault zone only)

1	Buff 1 zone
2	Red 1 zone
3	Cataclasite zone
4	Slip band A
5	Buff 2 zone
6	Red 2 zone

Undeformed sand permeability data for Elmendorf site, Bosque del Apache, NM							
Replicate measurements							
DATE	**X**	**Y**	**time [sec]**	**k [darcies]**	**Instr**	**Description**	
3/13/95	-3.360	1.000	9.13	7.4	S		
3/13/95	-3.360	1.000	8.52	8.0	S		
3/13/95	-3.360	1.000	8.94	7.6	S		
3/13/95	-3.310	1.000	9.03	7.5	S		
3/13/95	-3.310	1.000	10.67	6.3	S		
3/13/95	-3.310	1.000	9.01	7.5	S		
3/13/95	-3.310	1.000	9.24	7.3	S		
3/13/95	-3.260	1.000	7.20	9.5	S		
3/13/95	-3.260	1.000	7.32	9.3	S		
3/13/95	-3.260	1.000	6.95	8.0	S		
3/13/95	-3.160	1.000	9.89	6.8	S		
3/13/95	-3.160	1.000	8.92	7.6	S		
3/13/95	-3.160	1.000	10.04	6.7	S		
3/13/95	-3.160	1.000	8.91	7.6	S		
3/13/95	-3.010	1.000	6.01	11.5	S		
3/13/95	-3.010	1.000	5.38	12.9	S		
3/13/95	-3.010	1.000	6.06	11.4	S		
3/13/95	-3.010	1.000	5.88	11.8	S		
3/13/95	-3.010	1.000	5.46	12.7	S		
3/13/95	-3.010	1.000	5.63	12.3	S		
3/13/95	-3.010	1.000	5.24	13.3	S		
3/13/95	-2.960	1.000	6.33	10.9	S		
3/13/95	-2.960	1.000	6.54	10.5	S		
3/13/95	-2.960	1.000	6.57	10.5	S		
3/13/95	-2.910	1.000	6.87	10.0	S		
3/13/95	-2.910	1.000	7.21	9.5	S		
3/13/95	-2.910	1.000	7.80	8.7	S		
3/13/95	-2.910	1.000	7.33	9.3	S		
3/13/95	-2.810	1.000	8.60	7.9	S	Buff f gr w/ coarse below	
3/13/95	-2.810	1.000	8.95	7.6	S	Buff f gr w/ coarse below	
3/13/95	-2.810	1.000	8.77	7.7	S	Buff f gr w/ coarse below	

Undeformed sand permeability data for Elmendorf site, Bosque del Apache, NM							
Replicate measurements							
DATE	**X**	**Y**	**time [sec]**	**k [darcies]**	**Instr**	**Description**	
3/13/95	-2.660	1.000	10.39	6.5	S		
3/13/95	-2.660	1.000	11.16	6.0	S		
3/13/95	-2.660	1.000	11.19	6.0	S		
3/3/95	-2.360	1.000	11.27	6.0	S		
3/3/95	-2.360	1.000	10.81	6.2	S		
3/3/95	-2.360	1.000	10.58	6.4	S		
3/3/95	-2.260	1.000	11.16	6.0	S		
3/3/95	-2.260	1.000	12.34	5.4	S		
3/3/95	-2.260	1.000	13.65	4.9	S		
3/3/95	-2.260	1.000	10.45	6.5	S		
3/3/95	-2.260	1.000	11.47	5.9	S		
3/3/95	-2.160	1.000	10.95	6.2	S	'lots of insect larvae borings	
3/3/95	-2.160	1.000	13.09	5.1	S	'lots of insect larvae borings	
3/3/95	-2.160	1.000	11.12	6.1	S	'lots of insect larvae borings	
3/3/95	-2.160	1.000	10.17	6.6	S	'lots of insect larvae borings	
3/3/95	-2.060	1.000	6.82	10.1	S	lots of insect larvae borings	
3/3/95	-2.060	1.000	5.73	12.1	S	lots of insect larvae borings	
3/3/95	-2.060	1.000	4.88	14.4	S	lots of insect larvae borings	
3/3/95	-2.010	1.000	5.24	13.3	S		
3/3/95	-2.010	1.000	7.74	8.8	S		
3/3/95	-2.010	1.000	5.99	11.5	S		
3/3/95	-2.010	1.000	5.77	12.0	S		
5/19/95	-2.000	1.000	7.19	9.5	S	br/gr	
5/19/95	-2.000	1.000	7.30	9.4	S	br/gr	
5/19/95	-2.000	1.000	7.63	8.9	S	br/gr	
3/3/95	-1.910	1.000	9.15	7.4	S	med-f gr lam	
3/3/95	-1.910	1.000	7.83	8.7	S	med-f gr lam	
3/3/95	-1.910	1.000	7.79	8.8	S	med-f gr lam	
3/3/95	-1.910	1.000	8.38	8.1	S	med-f gr lam	
3/3/95	-1.760	1.000	8.66	7.8	S	mixed med-fine laminae, f sand	
3/3/95	-1.760	1.000	7.13	9.6	S	mixed med-fine laminae, f sand	

Undeformed sand permeability data for Elmendorf site, Bosque del Apache, NM							
Replicate measurements							
DATE	**X**	**Y**	**time [sec]**	**k [darcies]**	**Instr**	**Description**	
3/3/95	-1.760	1.000	7.08	9.7	S	mixed med-fine laminae, f sand	
3/3/95	-1.760	1.000	7.26	9.4	S	mixed med-fine laminae, f sand	
3/3/95	-1.660	1.000	8.04	8.5	S	med., light, gr, w/tiny laminae	
3/3/95	-1.660	1.000	7.24	9.4	S	med., light, gr, w/tiny laminae	
3/3/95	-1.660	1.000	7.75	8.8	S	med., light, gr, w/tiny laminae	
3/3/95	-1.660	1.000	8.34	8.2	S	med., light, gr, w/tiny laminae	
3/3/95	-1.610	1.000	6.38	10.8	S	med., light, gr, w/tiny laminae	
3/3/95	-1.610	1.000	7.02	9.8	S	med., light, gr, w/tiny laminae	
3/3/95	-1.610	1.000	6.90	9.9	S	med., light, gr, w/tiny laminae	
5/19/95	-1.500	1.000	8.56	7.9	S	br f 1 cm below planar,	sub-horiz concretion
5/19/95	-1.500	1.000	9.26	7.3	S	br f 1 cm below planar,	sub-horiz concretion
5/19/95	-1.500	1.000	9.31	7.3	S	br f 1 cm below planar,	sub-horiz concretion
5/19/95	-1.500	1.000	9.10	7.4	S	br f 1 cm below planar,	sub-horiz concretion
3/3/95	-1.260	1.000	8.70	7.8	S	as 1.5 but fine dark on top, lighter below	
3/3/95	-1.260	1.000	8.63	7.9	S	as 1.5 but fine dark on top, lighter below	
3/3/95	-1.260	1.000	8.46	8.0	S	as 1.5 but fine dark on top, lighter below	
3/13/95	-1.260	1.000	9.83	6.9	S		
3/13/95	-1.260	1.000	10.17	6.6	S		
3/13/95	-1.260	1.000	10.45	6.5	S		
3/3/95	-1.160	1.000	11.63	5.8	S	mixed med light-finer dark bands	
3/3/95	-1.160	1.000	10.74	6.3	S	mixed med light-finer dark bands	
3/3/95	-1.160	1.000	10.22	6.6	S	mixed med light-finer dark bands	
3/3/95	-1.160	1.000	11.34	5.9	S	mixed med light-finer dark bands	
3/13/95	-1.160	1.000	10.10	6.7	S		
3/13/95	-1.160	1.000	10.57	6.4	S		
3/13/95	-1.160	1.000	10.81	6.2	S		
3/3/95	-1.060	1.000	12.52	5.4	S	finer gr, darker zone	coarse zone at top
3/3/95	-1.060	1.000	11.25	6.0	S	finer gr, darker zone	coarse zone at top
3/3/95	-1.060	1.000	10.71	6.3	S	finer gr, darker zone	coarse zone at top
3/3/95	-1.060	1.000	10.07	6.7	S	finer gr, darker zone	coarse zone at top
3/13/95	-1.060	1.000	14.22	4.7	S		

Undeformed sand permeability data for Elmendorf site, Bosque del Apache, NM							
Replicate measurements							
DATE	**X**	**Y**	**time [sec]**	**k [darcies]**	**Instr**	**Description**	
3/13/95	-1.060	1.000	12.99	5.2	S		
3/13/95	-1.060	1.000	12.38	5.4	S		
5/19/95	-1.000	1.000	12.19	5.5	S	br f gr zone	
5/19/95	-1.000	1.000	12.57	5.3	S	br f gr zone	
5/19/95	-1.000	1.000	12.37	5.4	S	br f gr zone	
3/3/95	-0.960	1.000	12.28	5.5	S	m-c gr band, light	
3/3/95	-0.960	1.000	11.35	5.9	S	m-c gr band, light	
3/3/95	-0.960	1.000	12.27	5.5	S	m-c gr band, light	
3/3/95	-0.960	1.000	11.86	5.7	S	m-c gr band, light	
3/13/95	-0.960	1.000	11.60	5.8	S		
3/13/95	-0.960	1.000	11.23	6.0	S		
3/13/95	-0.960	1.000	10.95	6.2	S		
5/19/95	-2.000	1.100	10.96	6.1	S	small diff. in vertical loc. changed times	cemented area in center
5/19/95	-2.000	1.100	11.41	5.9	S	small diff. in vertical loc. changed times	cemented area in center
5/19/95	-2.000	1.100	13.01	5.2	S	small diff. in vertical loc. changed times	cemented area in center
5/19/95	-2.000	1.100	13.86	4.8	S	small diff. in vertical loc. changed times	cemented area in center
5/19/95	-1.500	1.100	15.06	4.4	S	tan br finer w/ thin, lighter	
5/19/95	-1.500	1.100	14.69	4.6	S	tan br finer w/ thin, lighter	
5/19/95	-1.500	1.100	15.17	4.4	S	tan br finer w/ thin, lighter	
5/19/95	-1.000	1.100	11.94	5.6	S	br f gr zone	
5/19/95	-1.000	1.100	11.49	5.9	S	br f gr zone	
5/19/95	-1.000	1.100	11.76	5.7	S	br f gr zone	
5/19/95	-2.000	1.200	9.26	7.3	S	br f gr band below lighter	
5/19/95	-2.000	1.200	9.69	7.0	S	br f gr band below lighter	
5/19/95	-2.000	1.200	9.34	7.2	S	br f gr band below lighter	
5/19/95	-1.500	1.200	10.89	6.2	S	lt br f gr	
5/19/95	-1.500	1.200	11.20	6.0	S	lt br f gr	
5/19/95	-1.500	1.200	11.00	6.1	S	lt br f gr	
5/19/95	-1.000	1.200	9.31	7.3	S	light f gr, better indurated	
5/19/95	-1.000	1.200	9.64	7.0	S	light f gr, better indurated	
5/19/95	-1.000	1.200	9.80	6.9	S	light f gr, better indurated	

Undeformed sand permeability data for Elmendorf site, Bosque del Apache, NM							
Replicate measurements							
DATE	**X**	**Y**	**time [sec]**	**k [darcies]**	**Instr**	**Description**	
5/19/95	-2.000	1.300	9.77	6.9	S	better ind., finer grain than	[2.0, 1.5]
5/19/95	-2.000	1.300	10.49	6.4	S	better ind., finer grain than	[2.0, 1.5]
5/19/95	-2.000	1.300	9.84	6.9	S	better ind., finer grain than	[2.0, 1.5]
5/19/95	-2.000	1.300	9.80	6.9	S	better ind., finer grain than	[2.0, 1.5]
5/19/95	-1.500	1.300	15.90	4.2	S	br f ss w/ thin coarser layer	
5/19/95	-1.500	1.300	15.67	4.3	S	br f ss w/ thin coarser layer	
5/19/95	-1.500	1.300	15.77	4.2	S	br f ss w/ thin coarser layer	
5/19/95	-1.000	1.300	6.58	10.4	S	lighter med f	
5/19/95	-1.000	1.300	5.89	11.7	S	lighter med f	
5/19/95	-1.000	1.300	6.36	10.8	S	lighter med f	
5/19/95	-1.000	1.300	5.99	11.5	S	lighter med f	
5/19/95	-1.500	1.400	7.46	9.2	S	lt br/tan f gr	
5/19/95	-1.500	1.400	8.11	8.4	S	lt br/tan f gr	
5/19/95	-1.500	1.400	7.50	9.1	S	lt br/tan f gr	
5/19/95	-1.500	1.400	7.62	9.0	S	lt br/tan f gr	
5/19/95	-1.000	1.400	7.43	9.2	S	med gr ss br & light color	
5/19/95	-1.000	1.400	7.44	9.2	S	med gr ss br & light color	
5/19/95	-1.000	1.400	7.66	8.9	S	med gr ss br & light color	
5/19/95	-2.000	1.500	7.66	8.9	S	med br/grey ss	
5/19/95	-2.000	1.500	7.49	9.1	S	med br/grey ss	
5/19/95	-2.000	1.500	8.19	8.3	S	med br/grey ss	
5/19/95	-2.000	1.500	7.77	8.8	S	med br/grey ss	
3/27/95	-0.600	1.500	7.75	8.8	S	in darker coarse material,	2 cm to left of SB A
3/27/95	-0.650	1.500	7.40	9.2	S	coarse gr ~ 7 cm left of SB A	
3/27/95	-0.650	1.500	7.16	9.6	S	coarse gr ~ 7 cm left of SB A	
3/27/95	-0.650	1.500	8.01	8.5	S	coarse gr ~ 7 cm left of SB A	
3/27/95	-0.650	1.500	7.67	8.9	S	coarse gr ~ 7 cm left of SB A	
3/27/95	-0.650	1.500	9.18	7.4	S	coarse gr ~ 7 cm left of SB A	
3/27/95	-0.650	1.500	8.13	8.4	S	coarse gr ~ 7 cm left of SB A	
3/13/95	-1.000	1.500	6.27	11.0	S	bug hole 1.5 cm to south & right	
3/13/95	-1.000	1.500	6.90	9.9	S	bug hole 1.5 cm to south & right	

Undeformed sand permeability data for Elmendorf site, Bosque del Apache, NM							
Replicate measurements							
DATE	**X**	**Y**	**time [sec]**	**k [darcies]**	**Instr**	**Description**	
3/13/95	-1.000	1.500	6.65	10.3	S	bug hole 1.5 cm to south & right	
3/13/95	-1.100	1.500	6.85	10.0	S	Crack running close to pt	
3/13/95	-1.100	1.500	9.06	7.5	S	Crack running close to pt	
3/13/95	-1.100	1.500	9.95	6.8	S	Crack running close to pt	
3/13/95	-1.100	1.500	6.56	10.5	S	Crack running close to pt	
3/27/95	-1.100	1.500	9.66	7.0	S		
3/27/95	-1.100	1.500	10.52	6.4	S		
3/27/95	-1.100	1.500	10.65	6.3	S		
3/27/95	-1.100	1.500	10.19	6.6	S		
3/13/95	-1.200	1.500	7.10	9.6	S	Piston sticking	thin lt coarse band
3/13/95	-1.200	1.500	8.06	8.4	S	Piston sticking	thin lt coarse band
3/13/95	-1.200	1.500	8.04	8.5	S	Piston sticking	thin lt coarse band
3/27/95	-1.200	1.500	8.95	7.6	S		
3/27/95	-1.200	1.500	10.31	6.5	S		
3/27/95	-1.200	1.500	8.58	7.9	S		
3/27/95	-1.200	1.500	8.81	7.7	S		
3/13/95	-1.300	1.500	9.15	7.4	S	lt coarser band	
3/13/95	-1.300	1.500	10.71	6.3	S	lt coarser band	
3/13/95	-1.300	1.500	9.23	7.3	S	lt coarser band	
3/13/95	-1.300	1.500	10.51	6.4	S	lt coarser band	
3/27/95	-1.300	1.500	10.66	6.3	S		
3/27/95	-1.300	1.500	10.27	6.6	S		
3/27/95	-1.300	1.500	10.88	6.2	S		
3/13/95	-1.400	1.500	9.56	7.1	S	darker finer gr band immed	
3/13/95	-1.400	1.500	8.20	8.3	S	darker finer gr band immed	
3/13/95	-1.400	1.500	8.27	8.2	S	darker finer gr band immed	
3/13/95	-1.400	1.500	9.31	7.3	S	darker finer gr band immed	
3/13/95	-1.450	1.500	8.38	8.1	S	lt med gr band	
3/13/95	-1.450	1.500	9.04	7.5	S	lt med gr band	
3/13/95	-1.450	1.500	8.56	7.9	S	lt med gr band	
3/13/95	-1.450	1.500	8.91	7.6	S	lt med gr band	

Undeformed sand permeability data for Elmendorf site, Bosque del Apache, NM							
Replicate measurements							
DATE	**X**	**Y**	**time [sec]**	**k [darcies]**	**Instr**	**Description**	
3/27/95	-1.450	1.500	7.57	9.0	S		
3/27/95	-1.450	1.500	7.45	9.2	S		
3/27/95	-1.450	1.500	7.32	9.3	S		
3/27/95	-1.450	1.500	7.56	9.0	S		
3/27/95	-1.700	1.500	7.38	9.3	S		
3/27/95	-1.700	1.500	7.42	9.2	S		
3/27/95	-1.700	1.500	9.86	6.9	S		
3/27/95	-1.700	1.500	7.72	8.8	S		
3/27/95	-1.700	1.500	7.81	8.7	S		
3/13/95	-1.800	1.500	10.00	6.8	S	bug holes	
3/13/95	-1.800	1.500	10.36	6.5	S	bug holes	
3/13/95	-1.800	1.500	10.36	6.5	S	bug holes	
3/27/95	-1.800	1.500	9.04	7.5	S		
3/27/95	-1.800	1.500	8.49	8.0	S		
3/27/95	-1.800	1.500	9.90	6.8	S		
3/27/95	-1.800	1.500	8.93	7.6	S		
3/27/95	-1.800	1.500	9.42	7.2	S		
3/27/95	-2.000	1.500	6.54	10.5	S	Very close to bug holes	
3/27/95	-2.000	1.500	5.81	11.9	S	Very close to bug holes	
3/27/95	-2.000	1.500	5.70	12.2	S	Very close to bug holes	
3/27/95	-2.000	1.500	5.49	12.7	S	Very close to bug holes	
3/27/95	-2.000	1.500	5.56	12.5	S	Very close to bug holes	

Fault zone sand permeability data for Elmendorf site, Bosque del Apache, NM							
Replicate measurements							
DATE	**X**	**Y**	**time [sec]**	**k [darcies]**	**Instr**	**Description**	
3/3/95	-0.160	1.000	10.06	6.7	S	B&W band w/ small c gr lamina in center ~3mm	Zone A - B
3/3/95	-0.160	1.000	9.41	7.2	S	B&W band w/ small c gr lamina in center ~3mm	Zone A - B
3/3/95	-0.160	1.000	9.75	6.9	S	B&W band w/ small c gr lamina in center ~3mm	Zone A - B
3/3/95	-0.110	1.000	9.80	6.9	S	~2cm from db to right, finer gr than B&W	Zone A - B
3/3/95	-0.110	1.000	10.93	6.2	S	~2cm from db to right, finer gr than B&W	Zone A - B
3/3/95	-0.110	1.000	10.79	6.2	S	~2cm from db to right, finer gr than B&W	Zone A - B
3/3/95	-0.110	1.000	10.77	6.3	S	~2cm from db to right, finer gr than B&W	Zone A - B
3/3/95	-0.060	1.000	12.12	5.5	S	in dark c gr B&W band, 1-2 cm band	~1.5cm left of db
3/3/95	-0.060	1.000	10.47	6.4	S	in dark c gr B&W band, 1-2 cm band	~1.5cm left of db
3/3/95	-0.060	1.000	10.19	6.6	S	in dark c gr B&W band, 1-2 cm band	~1.5cm left of db
3/3/95	-0.060	1.000	10.41	6.5	S	in dark c gr B&W band, 1-2 cm band	~1.5cm left of db
3/3/95	-0.028	1.000	12.49	5.4	S	Zone of db	
3/3/95	-0.028	1.000	12.45	5.4	S	Zone of db	
3/3/95	-0.028	1.000	12.98	5.2	S	Zone of db	
3/3/95	-0.028	1.000	19.14	3.5	S	Zone of db	
3/3/95	-0.028	1.000	13.98	4.8	S	Zone of db	
3/3/95	0.040	1.000	15.16	4.4	S	Zone of db: lots of db, some bedding preserved	
3/3/95	0.040	1.000	13.49	5.0	S	Zone of db: lots of db, some bedding preserved	
3/3/95	0.040	1.000	15.77	4.2	S	Zone of db: lots of db, some bedding preserved	
3/3/95	0.040	1.000	16.70	4.0	S	Zone of db: lots of db, some bedding preserved	
3/3/95	0.040	1.000	16.81	4.0	S	Zone of db: lots of db, some bedding preserved	
3/3/95	-0.360	1.000	6.94	9.9	S	in topmost B&W c sand, some cracks in vicinity	
3/3/95	-0.360	1.000	7.02	9.8	S	in topmost B&W c sand, some cracks in vicinity	
3/3/95	-0.360	1.000	7.22	9.5	S	in topmost B&W c sand, some cracks in vicinity	
3/3/95	-0.360	1.000	6.74	10.2	S	in topmost B&W c sand, some cracks in vicinity	
3/3/95	-0.010	1.000	7.32	9.3	S	med to c gr sand to right of SB B	between dbs
3/3/95	-0.010	1.000	8.08	8.4	S	med to c gr sand to right of SB B	between dbs
3/3/95	-0.010	1.000	9.13	7.4	S	med to c gr sand to right of SB B	between dbs
5/19/95	-0.160	1.000	9.51	7.1	S	br horiz lam gr above B&W	
5/19/95	-0.160	1.000	9.51	7.1	S	br horiz lam gr above B&W	
5/19/95	-0.160	1.000	9.74	6.9	S	br horiz lam gr above B&W	

Fault zone sand permeability data for Elmendorf site, Bosque del Apache, NM							
Replicate measurements							
DATE	**X**	**Y**	**time [sec]**	**k [darcies]**	**Instr**	**Description**	
5/19/95	-0.160	0.980	8.13	8.4	S	In coarse grain zone	
5/19/95	-0.160	0.980	6.71	10.2	S	In coarse grain zone	
5/19/95	-0.160	0.980	6.19	11.1	S	In coarse grain zone	
5/19/95	-0.160	0.980	7.60	9.0	S	In coarse grain zone	
5/19/95	-0.060	1.000	12.57	5.3	S	in coarse gr br adjacent to db	
5/19/95	-0.060	1.000	14.27	4.7	S	in coarse gr br adjacent to db	
5/19/95	-0.060	1.000	12.60	5.3	S	in coarse gr br adjacent to db	
5/19/95	-0.060	1.000	12.44	5.4	S	in coarse gr br adjacent to db	
5/19/95	-0.011	1.000	7.71	8.8	S	Zone of db: ~ 1.5 cm rt of SB B	
5/19/95	-0.011	1.000	6.99	9.8	S	Zone of db: ~ 1.5 cm rt of SB B	
5/19/95	-0.011	1.000	7.69	8.9	S	Zone of db: ~ 1.5 cm rt of SB B	
5/19/95	-0.011	1.000	7.52	9.1	S	Zone of db: ~ 1.5 cm rt of SB B	
5/19/95	0.040	1.000	14.12	4.7	S	Zone of db	
5/19/95	0.040	1.000	14.02	4.8	S	Zone of db	
5/19/95	0.040	1.000	15.78	4.2	S	Zone of db	
5/19/95	0.040	1.000	15.32	4.4	S	Zone of db	
7/13/95	-0.650	0.950		0.35	C	Into outcrop plane (SB A edge)	
7/13/95	-0.650	0.950		0.38	C	Into outcrop plane (SB A edge)	
7/13/95	-0.650	0.950		0.37	C	Into outcrop plane (SB A edge)	
7/13/95	-0.655	0.925		0.25	C	Into outcrop plane (SB A edge)	
7/13/95	-0.655	0.925		0.29	C	Into outcrop plane (SB A edge)	
7/13/95	-0.655	0.925		0.30	C	Into outcrop plane (SB A edge)	
7/13/95	-0.600	1.240		0.44	C	SB A Mark 1 on edge	~ 7 mm wide
7/13/95	-0.600	1.240		0.48	C	SB A Mark 1 on edge	~ 7 mm wide
7/13/95	-0.600	1.240		0.53	C	SB A Mark 1 on edge	~ 7 mm wide
7/13/95	-0.600	1.240		0.48	C	SB A Mark 1 on edge	~ 7 mm wide
7/13/95	-0.600	1.300		0.25	C	SB A Mark 2 on edge	~ 5-6 mm wide
7/13/95	-0.600	1.300		0.25	C	SB A Mark 2 on edge	~ 5-6 mm wide
7/13/95	-0.600	1.300		0.23	C	SB A Mark 2 on edge	~ 5-6 mm wide
7/13/95	-0.030	1.000		0.17	C	SB B Mark 1 on edge	~ 2.5 mm wide
7/13/95	-0.030	1.000		0.21	C	SB B Mark 1 on edge	~ 2.5 mm wide

Fault zone sand permeability data for Elmendorf site, Bosque del Apache, NM							
Replicate measurements							
DATE	**X**	**Y**	**time [sec]**	**k [darcies]**	**Instr**	**Description**	
7/13/95	-0.030	1.000		0.21	C	SB B Mark 1 on edge	~ 2.5 mm wide
7/13/95	-0.030	1.000		0.19	C	SB B Mark 1 on edge	~ 2.5 mm wide
7/13/95	-0.035	0.940		0.28	C	SB B Mark 2 on edge	~ 2.5 mm wide
7/13/95	-0.035	0.940		0.26	C	SB B Mark 2 on edge	~ 2.5 mm wide
7/13/95	-0.035	0.940		0.28	C	SB B Mark 2 on edge	~ 2.5 mm wide
7/13/95	-0.560	1.000		0.61	C	Zone A-B, well-ind layer	above B&W layers
7/13/95	-0.560	1.000		0.60	C	Zone A-B, well-ind layer	above B&W layers
7/13/95	-0.560	1.000		0.60	C	Zone A-B, well-ind layer	above B&W layers
7/13/95	-0.650	0.975		0.32	C	Normal to SB A	~ 8 mm wide
7/13/95	-0.650	0.975		0.32	C	Normal to SB A	~ 8 mm wide
7/13/95	-0.650	0.975		0.31	C	Normal to SB A	~ 8 mm wide
7/13/95	-0.650	0.950		0.10	C	Normal to SB A	~ 8 mm wide
7/13/95	-0.650	0.950		0.18	C	Normal to SB A	~ 8 mm wide
7/13/95	-0.650	0.950		0.16	C	Normal to SB A	~ 8 mm wide
7/13/95	-0.650	0.950		0.16	C	Normal to SB A	~ 8 mm wide
7/13/95	-0.650	0.950		0.13	C	Normal to SB A	~ 8 mm wide
7/13/95	-0.650	0.950		0.16	C	Normal to SB A	~ 8 mm wide
7/13/95	-0.650	0.950		0.14	C	Normal to SB A	~ 8 mm wide
7/13/95	-0.650	0.950		0.14	C	Normal to SB A	~ 8 mm wide
7/13/95	-0.650	0.950		0.14	C	Normal to SB A	~ 8 mm wide
7/13/95	-0.655	0.925		0.04	C	Normal to SB A	~ 13 mm wide
7/13/95	-0.655	0.925		0.05	C	Normal to SB A	~ 13 mm wide
7/13/95	-0.655	0.925		0.05	C	Normal to SB A	~ 13 mm wide
7/13/95	-0.655	0.925		0.04	C	Normal to SB A	~ 13 mm wide
7/13/95	-0.655	0.900		0.28	C	Normal to SB A	~ 13 mm wide
7/13/95	-0.655	0.900		0.40	C	Normal to SB A	~ 13 mm wide
7/13/95	-0.655	0.900		0.37	C	Normal to SB A	~ 13 mm wide
7/13/95	-0.655	0.900		0.36	C	Normal to SB A	~ 13 mm wide
7/13/95	-0.655	0.850		0.96	C	Normal to SB A	~ 10 mm wide
7/13/95	-0.655	0.850		1.03	C	Normal to SB A	~ 10 mm wide
7/13/95	-0.655	0.850		1.05	C	Normal to SB A	~ 10 mm wide

Undeformed sand permeability data for Santa Ana site, Rio Rancho, NM						
Replicate measurements						
DATE	**X**	**Y**	**time [sec]**	**k [darcies]**	**Instr**	**Description**
3/29/95	0.200	0.000	6.23	11.1	S	To left of fault zone, 1 cm to left of white SB
			6.08	11.4	S	
			6.03	11.5	S	
3/29/95	0.150	0.000	8.34	8.2	S	db
			8.19	8.3	S	
			8.02	8.5	S	
			7.89	8.6	S	
3/29/95	0.100	0.000	7.33	9.3	S	
			7.32	9.3	S	
			7.24	9.5	S	
3/29/95	-0.100	0.000	8.99	7.5	S	
			8.45	8.0	S	
			8.43	8.1	S	
			8.09	8.4	S	
			7.88	8.7	S	
6/27/95	-0.100	0.000	6.37	11.3	S	
			6.24	11.5	S	
			6.2	11.6	S	
7/11/95	-0.100	0.000	6.74	10.6	S	DT block
			6.31	11.4	S	
			5.95	12.1	S	
			5.95	12.1	S	
5/16/95	-0.100	0.250	6.88	10.4	S	
			6.75	10.6	S	
			6.24	11.5	S	
6/12/95	-0.100	0.500	9.32	7.6	S	
			9.12	7.7	S	
			9.08	7.8	S	
3/29/95	-0.200	0.000	7.05	9.7	S	
			6.88	10.0	S	
			6.78	10.1	S	

Undeformed sand permeability data for Santa Ana site, Rio Rancho, NM						
Replicate measurements						
DATE	**X**	**Y**	**time [sec]**	**k [darcies]**	**Instr**	**Description**
			6.56	10.5	S	
7/11/95	-0.200	0.000	7.92	9.0	S	
			7.66	9.3	S	
			7.43	9.6	S	
5/16/95	-0.200	0.250	7.45	9.6	S	
			7.42	9.6	S	
			7.29	9.8	S	
6/12/95	-0.200	0.500	7.33	9.7	S	
			7.2	9.9	S	
			7.15	10.0	S	
3/29/95	-0.275	0.000	6.59	10.4	S	on db
			5.84	11.9	S	
			5.25	13.3	S	
			5.09	13.7	S	
3/29/95	-0.300	0.000	7.89	8.6	S	
			7.18	9.5	S	
			6.88	10.0	S	
			6.59	10.4	S	
7/11/95	-0.300	0.000	7.12	10.0	S	
			6.59	10.9	S	
			6.55	10.9	S	
5/16/95	-0.300	0.250	7.45	9.6	S	
			7.31	9.8	S	
			6.95	10.3	S	
6/12/95	-0.300	0.500	7.81	9.1	S	
			7.73	9.2	S	
			7.3	9.8	S	
3/29/95	-0.400	0.000	7.45	9.2	S	
			7.25	9.4	S	
			7.16	9.6	S	
6/27/95	-0.400	0.000	6.66	10.8	S	

Undeformed sand permeability data for Santa Ana site, Rio Rancho, NM						
Replicate measurements						
DATE	**X**	**Y**	**time [sec]**	**k [darcies]**	**Instr**	**Description**
			6.27	11.5	S	
			6.13	11.7	S	
7/11/95	-0.400	0.000	6.46	11.1	S	
			6.26	11.5	S	
			6.18	11.6	S	
5/16/95	-0.400	0.250	7.45	9.6	S	alongside sub-v db
			7.15	10.0	S	
			7.03	10.2	S	
			6.56	10.9	S	
6/12/95	-0.400	0.500	8.2	8.6	S	
			8.2	8.6	S	
			7.95	8.9	S	
6/7/95	-0.500	-0.600	7.27	9.8	S	
			6.81	10.5	S	
			6.59	10.9	S	
6/7/95	-0.500	-0.500	8.41	8.4	S	
			8.37	8.5	S	
			8.32	8.5	S	
6/4/95	-0.500	-0.400	7.47	9.5	S	
			7.37	9.7	S	
			7.3	9.8	S	
6/4/95	-0.500	-0.300	8.69	8.1	S	
			8.32	8.5	S	
			7.85	9.1	S	
			7.63	9.3	S	
6/4/95	-0.500	-0.200	5.94	12.1	S	
			5.63	12.8	S	
			5.14	14.2	S	
			5.07	14.4	S	
			4.93	14.8	S	
3/29/95	-0.500	0.000	8.31	8.2	S	

Undeformed sand permeability data for Santa Ana site, Rio Rancho, NM						
Replicate measurements						
DATE	**X**	**Y**	**time [sec]**	**k [darcies]**	**Instr**	**Description**
			7.86	8.7	S	
			7.74	8.8	S	
			7.6	9.0	S	
			7.38	9.3	S	
6/27/95	-0.500	0.000	7.16	10.0	S	
			6.54	11.0	S	
			6.45	11.1	S	
			6.33	11.3	S	
7/11/95	-0.500	0.000	6.66	10.8	S	
			6.32	11.4	S	
			6.2	11.6	S	
6/4/95	-0.500	0.200	7.53	9.5	S	
			7.45	9.6	S	
			7.16	10.0	S	
			6.56	10.9	S	
			6.47	11.1	S	
5/16/95	-0.500	0.250	7.89	9.0	S	
			7.2	9.9	S	
			7.08	10.1	S	
6/4/95	-0.500	0.250	7.38	9.7	S	
			6.84	10.5	S	
			6.79	10.5	S	
			6.55	10.9	S	
			6.39	11.2	S	
6/7/95	-0.500	0.250	7.36	9.7	S	
			6.96	10.3	S	
			6.89	10.4	S	
			6.48	11.1	S	
6/4/95	-0.500	0.300	6.94	10.3	S	
			6.77	10.6	S	
			6.56	10.9	S	

Undeformed sand permeability data for Santa Ana site, Rio Rancho, NM						
Replicate measurements						
DATE	**X**	**Y**	**time [sec]**	**k [darcies]**	**Instr**	**Description**
			6.31	11.4	S	
			6.26	11.5	S	
6/4/95	-0.500	0.400	6.07	11.9	S	
			5.98	12.1	S	
			5.87	12.3	S	
			5.61	12.9	S	
6/7/95	-0.500	0.400	6.96	10.3	S	
			6.49	11.1	S	
			6.32	11.4	S	
			6.16	11.7	S	
			6.04	11.9	S	
6/4/95	-0.500	0.500	6.63	10.8	S	
			6.34	11.3	S	
			6.19	11.6	S	
			6.16	11.7	S	
			6.09	11.8	S	
6/7/95	-0.500	0.500	6.59	10.9	S	
			6.42	11.2	S	
			6.34	11.3	S	
			6.31	11.4	S	
3/29/95	-0.600	0.000	7.94	8.6	S	
			7.64	8.9	S	
			7.4	9.2	S	
7/11/95	-0.600	0.000	7.84	9.1	S	Between 2 dbs, 1 cuts thru sample vol
			7.24	9.8	S	
			7.17	9.9	S	
5/16/95	-0.600	0.250	7.03	10.2	S	
			6.86	10.4	S	
			6.75	10.6	S	
6/12/95	-0.600	0.500	6.84	10.5	S	
			6.77	10.6	S	

Undeformed sand permeability data for Santa Ana site, Rio Rancho, NM						
Replicate measurements						
DATE	**X**	**Y**	**time [sec]**	**k [darcies]**	**Instr**	**Description**
			6.28	11.4	S	
			6.2	11.6	S	
			5.95	12.1	S	
7/11/95	-0.700	0.000	6.63	10.8	S	
			6.47	11.1	S	
			6.44	11.1	S	
5/16/95	-0.700	0.250	6.98	10.2	S	
			6.97	10.3	S	
			6.77	10.6	S	
			6.7	10.7	S	
			6.44	11.1	S	
5/16/95	-0.800	0.250	6.98	10.2	S	
			6.97	10.3	S	
			6.77	10.6	S	
			6.7	10.7	S	
			6.44	11.1	S	
6/12/95	-0.800	0.500	9	7.8	S	
			8.47	8.4	S	
			8.45	8.4	S	
			8.07	8.8	S	
			7.95	8.9	S	
7/11/95	-0.900	0.000	6.61	10.8	S	
			6.42	11.2	S	
			6.34	11.3	S	
5/16/95	-0.900	0.250	7.77	9.1	S	
			7.46	9.5	S	
			7.33	9.7	S	
6/7/95	-1.000	-0.500	7.49	9.5	S	
			7.49	9.5	S	
			7.3	9.8	S	
6/7/95	-1.000	-0.400	7.06	10.1	S	

Undeformed sand permeability data for Santa Ana site, Rio Rancho, NM						
Replicate measurements						
DATE	**X**	**Y**	**time [sec]**	**k [darcies]**	**Instr**	**Description**
			7.05	10.1	S	
			6.46	11.1	S	
6/7/95	-1.000	-0.300	6.52	11.0	S	
			6.2	11.6	S	
			6.04	11.9	S	
			6.03	11.9	S	
6/7/95	-1.000	-0.200	6.91	10.3	S	
			6.79	10.5	S	
			6.55	10.9	S	
6/7/95	-1.000	-0.100	7.69	9.2	S	
			7.45	9.6	S	
			6.57	10.9	S	
			6.27	11.5	S	
6/7/95	-1.000	0.000	6.16	11.7	S	
			6.06	11.9	S	
			5.74	12.6	S	
			5.65	12.8	S	
6/27/95	-1.000	0.000	7.4	9.6	S	
			7.22	9.9	S	
			7.22	9.9	S	
6/7/95	-1.000	0.100	6.19	11.6	S	
			6.06	11.9	S	
			5.71	12.7	S	
			5.66	12.8	S	
6/7/95	-1.000	0.200	7.59	9.4	S	
			7.59	9.4	S	
			7.27	9.8	S	
5/16/95	-1.000	0.250	7.77	9.1	S	
			7.59	9.4	S	
			7.59	9.4	S	
6/7/95	-1.000	0.250	7.85	9.1	S	

Undeformed sand permeability data for Santa Ana site, Rio Rancho, NM						
Replicate measurements						
DATE	**X**	**Y**	**time [sec]**	**k [darcies]**	**Instr**	**Description**
			7.51	9.5	S	
			7.47	9.5	S	
			6.92	10.3	S	
6/7/95	-1.000	0.300	7.57	9.4	S	
			7.27	9.8	S	
			7.06	10.1	S	
			7.03	10.2	S	
6/7/95	-1.000	0.400	6.76	10.6	S	
			6.73	10.6	S	
			6.62	10.8	S	
6/7/95	-1.000	0.500	6.98	10.2	S	
			6.73	10.6	S	
			6.65	10.8	S	
			6.56	10.9	S	
6/12/95	-1.000	0.500	7.2	9.9	S	close to vertical transect location
			6.84	10.5	S	
			6.74	10.6	S	
			6.01	12.0	S	
			5.95	12.1	S	
6/7/95	-1.000	0.600	6.56	10.9	S	
			6.39	11.2	S	
			6.19	11.6	S	
			5.8	12.4	S	
			5.8	12.4	S	
			5.77	12.5	S	
			5.71	12.7	S	
			5.54	13.1	S	
7/11/95	-1.100	0.000	6.9	10.4	S	
			6.52	11.0	S	
			6.24	11.5	S	
7/11/95	-1.150	0.000	7.24	9.8	S	

Undeformed sand permeability data for Santa Ana site, Rio Rancho, NM						
Replicate measurements						
DATE	**X**	**Y**	**time [sec]**	**k [darcies]**	**Instr**	**Description**
			7.24	9.8	S	
			7.13	10.0	S	
5/16/95	-1.200	0.250	6.89	10.4	S	
			6.73	10.6	S	
			6.57	10.9	S	
			6.55	10.9	S	
			6.53	11.0	S	
6/12/95	-1.200	0.500	8.38	8.5	S	
			7.59	9.4	S	
			6.91	10.3	S	
5/16/95	-1.300	0.250	8.42	8.4	S	
			8.35	8.5	S	
			8.23	8.6	S	
			8.18	8.7	S	
			7.86	9.0	S	
6/27/95	-1.400	0.000	7.84	9.1	S	
			7.58	9.4	S	
			7.26	9.8	S	
7/11/95	-1.400	0.000	6.91	10.3	S	
			6.84	10.5	S	
			6.61	10.8	S	
5/16/95	-1.400	0.250	6.63	10.8	S	
			6.55	10.9	S	
			6.08	11.8	S	
			6.01	12.0	S	
6/12/95	-1.400	0.500	7.52	9.5	S	
			7.42	9.6	S	
			7.26	9.8	S	
			6.73	10.6	S	
6/7/95	-1.500	-0.500	6.91	10.3	S	
			6.66	10.8	S	

Undeformed sand permeability data for Santa Ana site, Rio Rancho, NM						
Replicate measurements						
DATE	**X**	**Y**	**time [sec]**	**k [darcies]**	**Instr**	**Description**
			6.34	11.3	S	
6/7/95	-1.500	-0.400	5.66	12.8	S	
			5.45	13.3	S	
			5.24	13.9	S	
6/7/95	-1.500	-0.300	7.65	9.3	S	
			7.54	9.4	S	
			7.52	9.5	S	
			7.09	10.1	S	
6/7/95	-1.500	-0.200	8.6	8.2	S	
			8.39	8.4	S	
			8.38	8.5	S	
6/7/95	-1.500	-0.100	7.35	9.7	S	
			6.84	10.5	S	
			6.74	10.6	S	
			6.58	10.9	S	
6/7/95	-1.500	0.000	6.16	11.7	S	
			6.06	11.9	S	
			5.74	12.6	S	
			5.65	12.8	S	
6/7/95	-1.500	0.100	7.96	8.9	S	
			7.88	9.0	S	
			7.66	9.3	S	
			7.34	9.7	S	
			6.98	10.2	S	
6/7/95	-1.500	0.200	8.2	8.6	S	
			8.18	8.7	S	
			8.01	8.9	S	
5/16/95	-1.500	0.250	7.66	9.3	S	
			7.51	9.5	S	
			7.5	9.5	S	
6/7/95	-1.500	0.250	6.45	11.1	S	

Undeformed sand permeability data for Santa Ana site, Rio Rancho, NM						
Replicate measurements						
DATE	**X**	**Y**	**time [sec]**	**k [darcies]**	**Instr**	**Description**
			6.05	11.9	S	
			5.95	12.1	S	
			5.58	13.0	S	
6/7/95	-1.500	0.300	6.85	10.4	S	
			6.74	10.6	S	
			6.46	11.1	S	
6/7/95	-1.500	0.400	6.53	11.0	S	
			6.41	11.2	S	
			6.38	11.3	S	
6/7/95	-1.500	0.500	6.32	11.4	S	
			6.24	11.5	S	
			6.2	11.6	S	
7/11/95	-1.650	0.000	6.77	10.6	S	
			6.59	10.9	S	
			6.57	10.9	S	
			6.36	11.3	S	
7/11/95	-1.700	0.000	6.94	10.3	S	
			6.81	10.5	S	
			6.52	11.0	S	
7/11/95	-1.800	0.000	6.22	11.6	S	
			6.13	11.7	S	
			5.98	12.0	S	
6/12/95	-1.800	0.500	8.49	8.3	S	
			7.78	9.1	S	
			6.93	10.3	S	
			6.75	10.6	S	
			6.57	10.9	S	
7/11/95	-1.900	0.000	6.95	10.3	S	
			6.83	10.5	S	
			6.75	10.6	S	
6/12/95	-2.000	-0.550	18.38	3.8	S	

Undeformed sand permeability data for Santa Ana site, Rio Rancho, NM						
Replicate measurements						
DATE	**X**	**Y**	**time [sec]**	**k [darcies]**	**Instr**	**Description**
			18.31	3.8	S	
			16.99	4.1	S	
			16.49	4.2	S	
6/12/95	-2.000	-0.500	9.56	7.4	S	
			7.13	10.0	S	
			7.05	10.1	S	
6/12/95	-2.000	-0.350	7.42	9.6	S	
			6.9	10.4	S	
			6.81	10.5	S	
			6.8	10.5	S	
6/12/95	-2.000	-0.300	6.53	11.0	S	
			6.52	11.0	S	
			6.27	11.5	S	
6/12/95	-2.000	-0.200	6.25	11.5	S	
			6.21	11.6	S	
			5.95	12.1	S	
			5.66	12.8	S	
6/12/95	-2.000	-0.100	5.95	12.1	S	
			5.79	12.5	S	
			5.7	12.7	S	
6/12/95	-2.000	0.000	5.8	12.4	S	
			5.41	13.4	S	
			5.2	14.0	S	
6/12/95	-2.000	0.100	6.42	11.2	S	
			5.82	12.4	S	
			5.68	12.7	S	
6/12/95	-2.000	0.250	8.24	8.6	S	
			7.51	9.5	S	
			7.5	9.5	S	
			7.46	9.5	S	
6/12/95	-2.000	0.350	7.5	9.5	S	

Undeformed sand permeability data for Santa Ana site, Rio Rancho, NM						
Replicate measurements						
DATE	**X**	**Y**	**time [sec]**	**k [darcies]**	**Instr**	**Description**
			7.45	9.6	S	
			7.39	9.6	S	
6/12/95	-2.000	0.450	6.48	11.1	S	
			6.22	11.6	S	
			5.03	14.5	S	
			4.97	14.7	S	
			4.94	14.8	S	
6/12/95	-2.000	0.500	6.6	10.9	S	
			6.13	11.7	S	
			5.59	12.9	S	
			5.53	13.1	S	
6/12/95	-2.000	0.550	8.31	8.5	S	
			8.16	8.7	S	
			7.59	9.4	S	
			7.52	9.5	S	
			7.46	9.5	S	
6/12/95	-2.000	0.750	6.58	10.9	S	
			6.56	10.9	S	
			6.45	11.1	S	
7/11/95	-2.200	0.000	6.49	11.0	S	
			6.28	11.4	S	
			6.2	11.6	S	
6/12/95	-2.200	0.500	7.99	8.9	S	Near concretion
			7.81	9.1	S	
			7.67	9.3	S	
7/11/95	-2.400	0.000	8.81	8.0	S	White calcite cement
			8.76	8.1	S	
			8.38	8.5	S	
6/12/95	-2.400	0.500	8.01	8.9	S	
			7.74	9.2	S	
			7.61	9.3	S	

Undeformed sand permeability data for Santa Ana site, Rio Rancho, NM						
Replicate measurements						
DATE	**X**	**Y**	**time [sec]**	**k [darcies]**	**Instr**	**Description**
			6.96	10.3	S	
			6.57	10.9	S	
7/11/95	-2.500	0.000	6.81	10.5	S	
			6.74	10.6	S	
			6.54	11.0	S	
6/12/95	-2.550	0.500	6.61	10.8	S	
			6.26	11.5	S	
			5.64	12.8	S	
6/12/95	-2.590	0.500	17.95	3.9	S	On db
			17.21	4.0	S	
			16.37	4.2	S	
7/11/95	-2.600	0.000	7.21	9.9	S	Some white calcite cement
			6.96	10.3	S	
			6.8	10.5	S	
6/12/95	-2.600	0.500	6.77	10.6	S	On easternmost edge of db zone
			5.52	13.1	S	
7/11/95	-2.800	0.000	6.97	10.2	S	
			6.95	10.3	S	
			6.89	10.4	S	

Fault zone sand permeability data for Santa Ana site, Rio Rancho, NM							
Replicate measurements							
DATE	**X**	**Y**	**time [sec]**	**k [darcies]**	**Instr**	**Description**	**CODE**
3/29/95	0.220	-0.075	15.58	4.3	S	In DT red zone	2
3/29/95	0.220	-0.075	15.48	4.3	S	In DT red zone	2
3/29/95	0.220	-0.075	17.49	3.8	S	In DT red zone	2
3/29/95	0.220	-0.075	15.35	4.4	S	In DT red zone	2
3/29/95	0.210	0.000	14.34	4.7	S	Start FZ On SB - white band 7-10mm wide	4
3/29/95	0.210	0.000	15.70	4.3	S	Start FZ On SB - white band 7-10mm wide	4
3/29/95	0.210	0.000	15.70	4.3	S	Start FZ On SB - white band 7-10mm wide	4
3/29/95	0.220	0.000	10.20	6.6	S	Just inside FZ buff	1
3/29/95	0.220	0.000	10.84	6.2	S	Just inside FZ buff	1
3/29/95	0.220	0.000	11.81	5.7	S	Just inside FZ buff	1
3/29/95	0.220	0.000	9.71	7.0	S	Just inside FZ buff	1
6/7/95	0.300	0.250	16.38	4.2	S	DT red zone	2
6/7/95	0.300	0.250	14.46	4.8	S	DT red zone	2
6/7/95	0.300	0.250	15.55	4.5	S	DT red zone	2
6/7/95	0.300	0.250	14.11	4.9	S	DT red zone	2
6/7/95	0.300	0.250	14.76	4.7	S	DT red zone	2
6/7/95	0.325	0.250	15.48	4.5	S	DT red zone	2
6/7/95	0.325	0.250	15.29	4.6	S	DT red zone	2
6/7/95	0.325	0.250	13.67	5.1	S	DT red zone	2
6/7/95	0.325	0.250	14.32	4.9	S	DT red zone	2
6/7/95	0.350	0.250	32.59	2.1	S	DT red zone On wh Calcareous	2
6/7/95	0.350	0.250	38.52	1.8	S	DT red zone On wh Calcareous	2
6/7/95	0.350	0.250	35.47	1.9	S	DT red zone On wh Calcareous	2
6/7/95	0.375	0.250	19.23	3.6	S	DT red zone	2
6/7/95	0.375	0.250	20.59	3.4	S	DT red zone	2
6/7/95	0.375	0.250	19.84	3.5	S	DT red zone	2
6/7/95	0.500	0.250	39.27	1.8	S	UT buff zone better ind., red cat to rt	5
6/7/95	0.500	0.250	33.54	2.1	S	UT buff zone better ind., red cat to rt	5
6/7/95	0.500	0.250	39.88	1.7	S	UT buff zone better ind., red cat to rt	5
6/7/95	0.500	0.250	36.16	1.9	S	UT buff zone better ind., red cat to rt	5
6/7/95	0.505	0.250	29.41	2.3	S	UT buff zone near db	5

Fault zone sand permeability data for Santa Ana site, Rio Rancho, NM							
Replicate measurements							
DATE	X	Y	time [sec]	k [darcies]	Instr	Description	CODE
6/7/95	0.505	0.250	35.10	2.0	S	UT buff zone near db	5
6/7/95	0.505	0.250	31.24	2.2	S	UT buff zone near db	5
6/7/95	0.525	0.250	18.75	3.7	S	UT buff/red zone, same as DT red	6
6/7/95	0.525	0.250	17.65	3.9	S	UT buff/red zone, same as DT red	6
6/7/95	0.525	0.250	17.46	4.0	S	UT buff/red zone, same as DT red	6
6/20/95	0.350	-0.200		0.28	C	Red cataclasite	3
6/20/95	0.350	-0.200		0.27	C	Red cataclasite	3
6/20/95	0.350	-0.200		0.29	C	Red cataclasite	3
6/20/95	0.360	-0.200		0.37	C	Red cataclasite	3
6/20/95	0.360	-0.200		0.39	C	Red cataclasite	3
6/20/95	0.360	-0.200		0.36	C	Red cataclasite	3
6/20/95	0.375	-0.200		0.36	C	Red cataclasite	3
6/20/95	0.375	-0.200		0.33	C	Red cataclasite	3
6/20/95	0.375	-0.200		0.36	C	Red cataclasite	3
6/20/95	0.385	-0.200		0.28	C	Red cat, In a whiteish band (calcite)	3
6/20/95	0.385	-0.200		0.32	C	Red cat, In a whiteish band (calcite)	3
6/20/95	0.385	-0.200		0.39	C	Red cat, In a whiteish band (calcite)	3
6/20/95	0.390	-0.200		0.71	C	Red cataclasite	3
6/20/95	0.390	-0.200		0.80	C	Red cataclasite	3
6/20/95	0.390	-0.200		0.64	C	Red cataclasite	3
6/20/95	0.390	-0.200		0.71	C	Red cataclasite	3
6/20/95	0.380	-0.150		1.04	C	Red cataclasite	3
6/20/95	0.380	-0.150		0.89	C	Red cataclasite	3
6/20/95	0.380	-0.150		0.93	C	Red cataclasite	3
6/20/95	0.400	-0.150		0.58	C	Red cat In slightly coarser gr band	3
6/20/95	0.400	-0.150		0.59	C	Red cat In slightly coarser gr band	3
6/20/95	0.400	-0.150		0.57	C	Red cat In slightly coarser gr band	3
6/20/95	0.420	-0.150		0.16	C	Red cataclasite	3
6/20/95	0.420	-0.150		0.17	C	Red cataclasite	3
6/20/95	0.420	-0.150		0.12	C	Red cataclasite	3
6/20/95	0.420	-0.150		0.12	C	Red cataclasite	3

Fault zone sand permeability data for Santa Ana site, Rio Rancho, NM							
Replicate measurements							
DATE	**X**	**Y**	**time [sec]**	**k [darcies]**	**Instr**	**Description**	**CODE**
6/20/95	0.425	-0.150		0.13	C	Red cataclasite	3
6/20/95	0.425	-0.150		0.15	C	Red cataclasite	3
6/20/95	0.425	-0.150		0.14	C	Red cataclasite	3
6/20/95	0.350	-0.100		0.77	C	Outside cat, in red zone, rt of clay core	6
6/20/95	0.350	-0.100		0.77	C	Outside cat, in red zone, rt of clay core	6
6/20/95	0.350	-0.100		0.77	C	Outside cat, in red zone, rt of clay core	6
6/20/95	0.370	-0.100		1.12	C	Outside cat, in red zone, rt of clay core	6
6/20/95	0.370	-0.100		1.13	C	Outside cat, in red zone, rt of clay core	6
6/20/95	0.370	-0.100		1.10	C	Outside cat, in red zone, rt of clay core	6
6/20/95	0.415	-0.100		0.40	C	Outside cat, in red zone, rt of clay core	6
6/20/95	0.415	-0.100		0.44	C	Outside cat, in red zone, rt of clay core	6
6/20/95	0.415	-0.100		0.47	C	Outside cat, in red zone, rt of clay core	6
6/20/95	0.430	-0.100		0.46	C	Outside cat, in red zone, rt of clay core Cracks near sample ar	6
6/20/95	0.430	-0.100		0.47	C	Outside cat, in red zone, rt of clay core Cracks near sample ar	6
6/20/95	0.430	-0.100		0.54	C	Outside cat, in red zone, rt of clay core Cracks near sample ar	6
6/20/95	0.440	-0.100		0.30	C	Outside cat, in red zone, rt of clay core	6
6/20/95	0.440	-0.100		0.34	C	Outside cat, in red zone, rt of clay core	6
6/20/95	0.440	-0.100		0.27	C	Outside cat, in red zone, rt of clay core	6
6/20/95	0.440	-0.100		0.22	C	Outside cat, in red zone, rt of clay core	6
6/20/95	0.440	-0.100		0.30	C	Outside cat, in red zone, rt of clay core	6
6/20/95	0.450	-0.100		0.30	C	Outside cat, in red zone, rt of clay core	6
6/20/95	0.450	-0.100		0.30	C	Outside cat, in red zone, rt of clay core	6
6/20/95	0.450	-0.100		0.30	C	Outside cat, in red zone, rt of clay core	6
6/20/95	0.250	0.250		0.13	C	In red zone of DT block within concretion	2
6/20/95	0.250	0.250		0.15	C	In red zone of DT block within concretion	2
6/20/95	0.250	0.250		0.13	C	In red zone of DT block within concretion	2
6/20/95	0.300	0.250		1.30	C	Red zone, DT block	2
6/20/95	0.300	0.250		1.64	C	Red zone, DT block	2
6/20/95	0.300	0.250		1.93	C	Red zone, DT block	2
6/20/95	0.325	0.250		2.04	C	Red zone, DT block	2
6/20/95	0.325	0.250		2.01	C	Red zone, DT block	2

Fault zone sand permeability data for Santa Ana site, Rio Rancho, NM							
Replicate measurements							
DATE	**X**	**Y**	**time [sec]**	**k [darcies]**	**Instr**	**Description**	**CODE**
6/20/95	0.325	0.250		2.23	C	Red zone, DT block	2
6/20/95	0.350	0.250		1.26	C	Red zone, DT block	2
6/20/95	0.350	0.250		1.43	C	Red zone, DT block	2
6/20/95	0.350	0.250		1.72	C	Red zone, DT block	2
6/20/95	0.400	0.250		0.28	C	Red zone, DT block	2
6/20/95	0.400	0.250		0.31	C	Red zone, DT block	2
6/20/95	0.400	0.250		0.19	C	Red zone, DT block	2
6/20/95	0.400	0.250		0.30	C	Red zone, DT block	2
6/20/95	0.505	0.250		1.00	C		5
6/20/95	0.505	0.250		1.01	C		5
6/20/95	0.505	0.250		0.97	C		5
6/20/95	0.520	0.250		1.77	C		
6/20/95	0.520	0.250		1.98	C		
6/20/95	0.520	0.250		2.37	C		
6/20/95	0.524	0.250		1.36	C		2
6/20/95	0.524	0.250		1.41	C		2
6/20/95	0.524	0.250		1.49	C		2
6/20/95	0.250	1.800		0.07	C	On SB A concretion, near rt angle bend	0
6/20/95	0.250	1.800		0.03	C	On SB A concretion, near rt angle bend	0
6/20/95	0.250	1.800		0.03	C	On SB A concretion, near rt angle bend	0
6/20/95	0.250	1.800		0.04	C	On SB A concretion, near rt angle bend	0
6/27/95	0.400	0.500	19.63	3.5	S	Red zone, DT Block	2
6/27/95	0.400	0.500	19.24	3.6	S	Red zone, DT Block	2
6/27/95	0.400	0.500	20.01	3.5	S	Red zone, DT Block	2
6/27/95	0.450	0.500	21.17	3.3	S	Red zone, DT Block	2
6/27/95	0.450	0.500	21.47	3.2	S	Red zone, DT Block	2
6/27/95	0.450	0.500	20.76	3.3	S	Red zone, DT Block	2
6/27/95	0.400	0.600	18.88	3.7	S	Red zone, DT Block	2
6/27/95	0.400	0.600	18.83	3.7	S	Red zone, DT Block	2
6/27/95	0.400	0.600	18.99	3.7	S	Red zone, DT Block	2
6/27/95	0.450	0.600	25.57	2.7	S	Red zone, DT Block	2

Fault zone sand permeability data for Santa Ana site, Rio Rancho, NM							
Replicate measurements							
DATE	**X**	**Y**	**time [sec]**	**k [darcies]**	**instr**	**Description**	**CODE**
6/27/95	0.450	0.600	31.82	2.2	S	Red zone, DT Block	2
6/27/95	0.450	0.600	31.31	2.2	S	Red zone, DT Block	2
6/27/95	0.300	0.700	9.66	7.3	S	Buff zone, DT Block 1.5 cm to rt of thick db	1
6/27/95	0.300	0.700	9.06	7.8	S	Buff zone, DT Block 1.5 cm to rt of thick db	1
6/27/95	0.300	0.700	9.27	7.6	S	Buff zone, DT Block 1.5 cm to rt of thick db	1
6/27/95	0.400	0.700	19.77	3.5	S	Red zone, DT Block, crack runs across zone	2
6/27/95	0.400	0.700	15.85	4.4	S	Red zone, DT Block, crack runs across zone	2
6/27/95	0.400	0.700	15.16	4.6	S	Red zone, DT Block, crack runs across zone	2
6/27/95	0.400	0.700	17.99	3.9	S	Red zone, DT Block, crack runs across zone	2
6/27/95	0.450	0.700	19.31	3.6	S	Red zone, DT Block	2
6/27/95	0.450	0.700	16.16	4.3	S	Red zone, DT Block	2
6/27/95	0.450	0.700	14.57	4.8	S	Red zone, DT Block	2
6/27/95	0.450	0.700	13.99	5.0	S	Red zone, DT Block	2
6/27/95	0.450	0.700	19.92	3.5	S	Red zone, DT Block	2
6/27/95	0.450	0.700	14.27	4.9	S	Red zone, DT Block	2
6/27/95	0.450	0.700	16.13	4.3	S	Red zone, DT Block	2
6/27/95	0.450	0.700	18.87	3.7	S	Red zone, DT Block	2
6/27/95	0.450	0.700	15.52	4.5	S	Red zone, DT Block	2
7/11/95	0.200	0.300	10.85	6.5	S	Slip band separating FZ buff zone from DT undef. block	4
7/11/95	0.200	0.300	10.66	6.6	S	Slip band separating FZ buff zone from DT undef. block	4
7/11/95	0.200	0.300	10.42	6.7	S	Slip band separating FZ buff zone from DT undef. block	4
7/11/95	0.215	0.300	9.34	7.6	S	Buff zone (total width = 4 cm)	1
7/11/95	0.215	0.300	9.54	7.4	S	Buff zone (total width = 4 cm)	1
7/11/95	0.215	0.300	9.56	7.4	S	Buff zone (total width = 4 cm)	1
7/11/95	0.230	0.300	10.50	6.7	S	Buff zone (total width = 4 cm)	1
7/11/95	0.230	0.300	10.65	6.6	S	Buff zone (total width = 4 cm)	1
7/11/95	0.230	0.300	10.99	6.4	S	Buff zone (total width = 4 cm)	1
7/11/95	0.250	0.300	17.63	3.9	S	Just inside red zone, near db	2
7/11/95	0.250	0.300	19.16	3.6	S	Just inside red zone, near db	2
7/11/95	0.250	0.300	18.53	3.7	S	Just inside red zone, near db	2
7/11/95	0.300	0.300	17.43	4.0	S	Red zone	2

Fault zone sand permeability data for Santa Ana site, Rio Rancho, NM							
Replicate measurements							
DATE	**X**	**Y**	**time [sec]**	**k [darcies]**	**Instr**	**Description**	**CODE**
7/11/95	0.300	0.300	16.94	4.1	S	Red zone	2
7/11/95	0.300	0.300	18.41	3.8	S	Red zone	2
7/11/95	0.300	0.300	18.69	3.7	S	Red zone	2
7/11/95	0.350	0.300	20.77	3.3	S	Red zone	2
7/11/95	0.350	0.300	21.77	3.2	S	Red zone	2
7/11/95	0.350	0.300	21.30	3.3	S	Red zone	2
7/11/95	0.400	0.300	25.45	2.7	S	Red zone	2
7/11/95	0.400	0.300	21.85	3.2	S	Red zone	2
7/11/95	0.400	0.300	23.16	3.0	S	Red zone	2
7/11/95	0.230	0.330	10.12	7.0	S	Buff zone (total width = 4 cm)	1
7/11/95	0.230	0.330	10.96	6.4	S	Buff zone (total width = 4 cm)	1
7/11/95	0.230	0.330	11.15	6.3	S	Buff zone (total width = 4 cm)	1
7/11/95	0.230	0.330	11.12	6.3	S	Buff zone (total width = 4 cm)	1
7/11/95	0.300	0.660	9.16	7.7	S	Buff zone	1
7/11/95	0.300	0.660	9.64	7.3	S	Buff zone	1
7/11/95	0.325	0.800	10.17	6.9	S	Buff zone	1
7/11/95	0.325	0.800	8.93	7.9	S	Buff zone	1
7/11/95	0.325	0.800	9.04	7.8	S	Buff zone	1
7/11/95	0.350	0.800	11.02	6.4	S	Buff zone	1
7/11/95	0.350	0.800	11.16	6.3	S	Buff zone	1
7/11/95	0.350	0.800	11.27	6.2	S	Buff zone	1
7/11/95	0.380	0.800	11.97	5.8	S	Buff zone, near red zone boundary	1
7/11/95	0.380	0.800	13.66	5.1	S	Buff zone, near red zone boundary	1
7/11/95	0.380	0.800	13.99	5.0	S	Buff zone, near red zone boundary	1
7/11/95	0.450	0.800	22.59	3.1	S	Red zone	2
7/11/95	0.450	0.800	22.63	3.1	S	Red zone	2
7/11/95	0.450	0.800	21.03	3.3	S	Red zone	2
7/11/95	0.500	0.800	24.71	2.8	S	Red zone	2
7/11/95	0.500	0.800	22.88	3.0	S	Red zone	2
7/11/95	0.500	0.800	30.56	2.3	S	Red zone	2